National Library of Canada

Acquisitions and Bibliographic Services Branch

395 Wellington Street
Ottawa, Ontario
K1A 0N4

Bibliothèque nationale du Canada

Direction des acquisitions et des services bibliographiques

395, rue Wellington
Ottawa (Ontario)
K1A 0N4

Your file Votre référence

Our file Notre référence

NOTICE

The quality of this microform is heavily dependent upon the quality of the original thesis submitted for microfilming. Every effort has been made to ensure the highest quality of reproduction possible.

If pages are missing, contact the university which granted the degree.

Some pages may have indistinct print especially if the original pages were typed with a poor typewriter ribbon or if the university sent us an inferior photocopy.

Reproduction in full or in part of this microform is governed by the Canadian Copyright Act, R.S.C. 1970, c. C-30, and subsequent amendments.

AVIS

La qualité de cette microforme dépend grandement de la qualité de la thèse soumise au microfilmage. Nous avons tout fait pour assurer une qualité supérieure de reproduction.

S'il manque des pages, veuillez communiquer avec l'université qui a conféré le grade.

La qualité d'impression de certaines pages peut laisser à désirer, surtout si les pages originales ont été dactylographiées à l'aide d'un ruban usé ou si l'université nous a fait parvenir une photocopie de qualité inférieure.

La reproduction, même partielle, de cette microforme est soumise à la Loi canadienne sur le droit d'auteur, SRC 1970, c. C-30, et ses amendements subséquents.

Canada

UNIVERSITY OF ALBERTA

POLYCHLORINATED BIPHENYL COMBUSTION IN A MONOLITH REACTOR

BY

ADAM JOHN RANKIN ©

A thesis submitted to the Faculty of Graduate Studies and Research in partial fulfilment of the requirements for the degree of

MASTER OF SCIENCE

DEPARTMENT OF CHEMICAL ENGINEERING

Edmonton, Alberta, CANADA

Fall, 1993

National Library
of Canada

Acquisitions and
Bibliographic Services Branch

395 Wellington Street
Ottawa, Ontario
K1A 0N4

Bibliothèque nationale
du Canada

Direction des acquisitions et
des services bibliographiques

395, rue Wellington
Ottawa (Ontario)
K1A 0N4

Your file Votre référence

Our file Notre référence

The author has granted an irrevocable non-exclusive licence allowing the National Library of Canada to reproduce, loan, distribute or sell copies of his/her thesis by any means and in any form or format, making this thesis available to interested persons.

L'auteur a accordé une licence irrévocable et non exclusive permettant à la Bibliothèque nationale du Canada de reproduire, prêter, distribuer ou vendre des copies de sa thèse de quelque manière et sous quelque forme que ce soit pour mettre des exemplaires de cette thèse à la disposition des personnes intéressées.

The author retains ownership of the copyright in his/her thesis. Neither the thesis nor substantial extracts from it may be printed or otherwise reproduced without his/her permission.

L'auteur conserve la propriété du droit d'auteur qui protège sa thèse. Ni la thèse ni des extraits substantiels de celle-ci ne doivent être imprimés ou autrement reproduits sans son autorisation.

ISBN 0-315-88099-6

Canada

UNIVERSITY OF ALBERTA

RELEASE FORM

NAME OF AUTHOR : Adam John Rankin

TITLE OF THESIS : Polychlorinated Biphenyl Combustion in a Monolith Reactor

DEGREE : Master of Science

YEAR THIS DEGREE GRANTED : 1993

Permission is hereby granted to the University of Alberta Library to reproduce single copies of this thesis and to lend or sell such copies for private, scholarly or scientific research purposes only.

The author reserves all other publication and other rights in association with the copyright in the thesis, and except as hereinbefore provided neither the thesis nor any substantial portion thereof may be printed or otherwise reproduced in any material form whatever without the author's prior written permission.

A. Rankin

Adam J. Rankin
165 Balcombe Road
Horley
Surrey, RH6 9DR
United Kingdom

Dated April 30th 1993.

The crisp, still, morning twilight, emblazoned
in a starry canopy of dark velvet sky,
is at once sanctified by the soulful
entreaties of coyotes in chorus and
mellowed by the delicate lowing
of a great horned owl calling from a
nearby juniper grove. In my morning
prayers for guidance, I envisioned my
ancestors' experience many generations ago;
as the night sentry peered carefully
into the predawn stillness from under the
warming enclosure of his buffalo robe,
once again acknowledging another late
summer day in this sacred place.

Overhead, the great thunderbird races
along on a flashing path leaving behind
a vaporous trail marking its passing.
The Sun is coming!

(Desert Dance)

UNIVERSITY OF ALBERTA
FACULTY OF GRADUATE STUDIES AND RESEARCH

The undersigned certify that they have read, and recommended to the Faculty of Graduate Studies and Research, a thesis entitled **Polychlorinated Biphenyl Combustion in a Monolith Reactor** submitted by **Adam John Rankin** in partial fulfilment of the requirements for the degree of **Master of Science**.

Rob Hayes
Dr. R.E. Hayes (Supervisor)

S.E. Wanke
Dr. S.E. Wanke

J.D. Dale
Dr. J.D. Dale

Dr. S.T. Kolaczkowski

Dated April 30th 1993.

to my Parents and Grandparents

ABSTRACT

This research concerns the catalytic combustion of polychlorinated biphenyls (PCB) in a monolith reactor, as an alternative technique to destroy hazardous waste safely and at relatively low operating temperatures. The objective of this study was to develop a mathematical model of a single channel monolith reactor used for the catalytic combustion of a commercially used mixture of PCB, known as Aroclor 1242 (42% chlorine by weight).

Data were previously obtained using a reactor of 15 mm inside diameter and lengths varying from 15 to 31 cm which was installed in a high temperature furnace. A feed of vaporised PCB, air and nitrogen was fed into the reactor, at inlet temperatures ranging from 740 - 1060 K and inlet PCB concentrations of 3700 - 7200 ppm. Outlet PCB concentrations were measured using high performance liquid chromatography (HPLC). The axial centre-line temperature profiles were also recorded by means of a thermocouple that could be traversed inside a thin sleeve. Homogeneous combustion was studied by carrying out experiments in an uncoated tubular reactor. Simultaneous homogeneous and catalytic combustion was then investigated using a channel coated with a chromia catalyst.

A two-dimensional mathematical model was developed to simulate the reactor system. It can incorporate the effects of internal and external radiation, axial wall conduction, fully developed or developing gas flow as well as homogeneous and catalytic wall reaction. The model consists of a series of non-linear partial differential equations which were solved using the Galerkin finite element method. Optimum model convergence was obtained using a transient algorithm which involves solving the wall temperature profile as a separate one-dimensional problem.

Analysis of the experimental data with the reactor model, gave an insight into the homogeneous and catalytic combustion kinetics of PCB and the mass and heat transfer phenomena that exist in a monolith channel. The catalytic reaction was found to be limited by the rate of diffusion to the wall. Radial temperature profiles indicated that the flow was thermally non-developed which was also apparent in the values of Nusselt number. In addition, the axial temperature profile measured with a thermocouple probe was shown to be significantly affected by internal radiation and axial wall conduction, the average inlet gas temperature being 20 - 150 K lower than the inlet probe wall temperature.

ACKNOWLEDGEMENTS

In completing this research study I gratefully acknowledge:

Financial support from the Natural Science and Engineering Research Council (Canada), Science and Engineering Research Council (U.K.), External Affairs and International Trade Canada, University of Alberta Central Research Fund, and the Mary Louise Imrie Graduate Award.

The experimental work completed by Dr. S.P. Perera in conjunction with the Reaction Engineering research group of the School of Chemical Engineering at the University of Bath, United Kingdom.

The love and support of Claudia and my family.

I offer my sincere thanks to Dr. R.E. Hayes for his great support and guidance during this project as my research supervisor and for providing me with the invaluable opportinity to study in Canada. I am grateful to Bob Barton in the DACS centre and Walter Boddez in the instrument shop for being always helpful. Special thanks also to the ever cheerful Cindy Heisler and Bev Walker in the deparment office, the Faculty of the Department of Chemical Engineering and the staff of the International Centre for their help and enlightenment.

The friends and *compañeros* I made during my time at this University remain special to me and include to mention a couple:

Wellington Kwok, Harald Huebscher, Philip Mees, Mike Macharia, Sam Dhaliwal, Cleve Graham, Paul Nawrocki, Munawar Saudagar, Amr Henni, Kevin Dorma, Andy Jenkins, S. Lakshminarayanan, Ramesh Sadhankar, Maggie Bowers, Leigh Wardhaugh, Jayant Chakravarty, Don Ryland, Christine Ho, Sergio Ghosh, Angela Canavo, Mary Sewell, Shelita, Albert, Pablo, Thor, Jessica, Mark, Andy, Liz, Balbi, Doug, Jochen, Super Green Mario, Paul Bélanger, Randy Lawrence, David Johnson, Maria Torres and CENSAT.

TABLE OF CONTENTS

List of tables
List of figures
Nomenclature

1 **Introduction** 1

1.1 Polychlorinated biphenyls - what are they and why should we destroy them 1

1.2 Current PCB disposal methods 4

1.3 Catalytic combustion and monolith reactors 6

1.4 Combustion of chlorinated wastes - a literature survey 10

1.5 Project outline and objectives 12

1.6 Layout of the thesis 12

2 **Experimental Work** 14

2.1 Experimental apparatus 14

2.2 Homogeneous combustion experiments 18

2.3 Catalytic combustion experiments 23

3 **Development of the Mathematical Model** 29

3.1 The governing equations 29

3.2 Physical properties 34

3.3 PCB combustion kinetics 37

3.4 Solution methodology 38

3.5 Model development due to the thermocouple probe 46

3.6 Developing velocity profile in an annulus 50

3.7 Convergence behaviour and the transient algorithm 55

3.8 Validation of the model 62

4 Numerical Results and Discussion 64

4A : Uncoated Channel Experiments 65

- 4A.1 Preliminary homogenous kinetics 65
- 4A.2 Temperature and concentration profiles 67
- 4A.3 Optimisation of the homogeneous kinetics 73
- 4A.4 Incorporation of the thermocouple probe in the model 76
- 4A.5 Heat and mass transfer coefficients 86
- 4A.6 Sensitivity analysis 89
- 4A.7 Verification of the homogeneous kinetics 98

4B : Catalyst Coated Channel Experiments 103

- 4B.1 Preliminary observations on catalytic reaction 103
- 4B.2 Model analysis 106
- 4B.3 Diffusion limited catalytic reaction 119
- 4B.4 Homogeneous kinetics reviewed 128

5 Conclusions and Recommendations 139

- 5.1 Conclusions 139
- 5.2 Recommendations for future work 141

References 144

A Appendix 149

- A.1 Physical properties of the composite channel wall 149
- A.2 Heat of combustion for PCB 152
- A.3 Molecular diffusion coefficient for PCB 154
- A.4 View factors for an empty tube 155
- A.5 View factors for an annular geometry 159

B Appendix 171

- B.1 Example parameter file for the mathematical model of the single channel monolith reactor 171

LIST OF TABLES

2-1	Properties of Aroclor 1242 PCB	15
2-2	Details of the reactor assembly	20
2-3	Homogeneous combustion results at varying inlet PCB concentrations	21
2-4	Homogeneous combustion results at varying inlet temperatures	24
2-5(a)	Catalytic combustion results at varying reactor lengths	25
2-5(b)	Axial temperature profiles for catalytic combustion experiments	27
3-1	Physical properties of the reactor system	35
3-2	Molecular diffusion coefficient for PCB	36
3-3	Developing flow lengths at different Reynolds numbers	55
3-4	Options available in the reactor model	63
4-1	Results for temperature independent kinetics	66
4-2	Evaluation of the homogeneous kinetics	77
4-3	Effect of the thermocouple probe on the simulation	80
4-4	Accuracy of the parameters in the model	90
4-5	Sensitivity analysis on the model parameters	91
4-6	Verification of the homogeneous kinetics	99
4-7	Simulated conversions with different catalytic rate expressions	108
4-8	The effect of developing flow on the catalytic reaction	120
4-9	Results using an increased D_k value	121
4-10	Effect of molecular diffusion on homogeneous combustion	122
4-11	Results using a variable D_k value	127
4-12	Further results using a variable D_k value	128
4-13	Global homogeneous combustion kinetics for aromatics	130
4-14	Results for temperature independent kinetics	131
A-1	Cross-sectional areas of the components in the channel wall	151
A-2	Heat capacity constants for the components of the gas phase	153

LIST OF FIGURES

1-1 Chemical structure of an example PCB, PCDD and PCDF 3
1-2 Schematic of a typical rotary kiln hazardous waste incinerator 7
1-3 Catalytic combustion regimes 9

2-1(a) Flow diagram of experimental apparatus 16
2-1(b) Photograph of experimental apparatus 17
2-1(c) Photograph of the single channel monolith reactor 17
2-2 Schematic of the single channel monolith reactor 19
2-3 Measured axial centre-line temperature for a homogeneous combustion run 22
2-4 Measured axial temperature profiles for catalytic combustion at different reactor lengths 28

3-1 External radiation exchange with the furnace 32
3-2(a) P2 triangular finite element and reference triangle 40
3-2(b) Examples of the finite element mesh 47
3-3 Model development due to internal radiation to the probe 49
3-4(a) Developing laminar flow in the reactor annulus 51
3-4(b) Finite element mesh for the Navier-Stokes solution 51
3-5 Developing velocity profile in the reactor annulus 54
3-6 The reactor model and the transient algorithm 59
3-7 Non-insulated boundary condition for the probe 61

4-1 Preliminary homogeneous kinetics 68
4-2 Simulated axial temperature profile 69
4-3 Simulated radial temperature profile 70
4-4 Simulated radial concentration profile 71
4-5 Plot showing the minimisation of the residual square error 74
4-6 Residual square error contour plot 75
4-7 Evaluation of the homogeneous kinetics : Outlet mole fraction of PCB 78

4-8 Axial temperature profiles with an annular geometry and at different T_{LR} values 79
4-9 Radial temperature profiles with an annular geometry : effect of internal radiation 81
4-10 Internal radiation flux plot 82
4-11 Axial temperature profiles with and without axial wall conduction 84
4-12 Axial temperature profiles with different probe boundary conditions 85
4-13(a) *Sh* and *Nu* number plot for the inside channel wall 87
4-13(b) *Sh* and *Nu* number plot for the outside probe wall 88
4-14 Sensitivity analysis : variation in furnace temperature 92
4-15 Sensitivity analysis : variation in average inlet velocity 93
4-16(a) Sensitivity analysis : variation in internal wall emissivity value 94
4-16(b) Sensitivity analysis : variation in wall conduction resistance 95
4-17 Sensitivity analysis : variation in average inlet gas temperature 96
4-18 Sensitivity analysis : variation in the heat of reaction for PCB 97
4-19(a-c) Axial temperature profile with complete model 100-102
4-20 Temperature comparison profiles 104
4-21 Concentration comparison profiles 105
4-22 Radial concentration profile for catalytic reaction 107
4-23(a-f) Temperature profiles : consequence of model type 109-114
4-24(a) Radial temperature profile with catalytic reaction 115
4-24(b) Internal radiation flux plot with catalytic reaction 116
4-24(c) *Sh* and *Nu* number plot with catalytic reaction : Channel wall. 117
4-24(d) *Sh* and *Nu* number plot with catalytic reaction : Probe wall. 118
4-25(a-d) Axial temperature profiles at an increased diffusion coefficient 123-126
4-26 Homogeneous kinetics reviewed 133
4-27(a-d) Axial temperature profiles : Homogeneous kinetics reviewed 135-138

A-1 Diagram of an empty tube : view factors between surface elements 156
A-2 Diagram of an empty tube : view factors to the channel ends 156
A-3 Diagram of an annulus : view factors between surface elements and to the channel ends 160

NOMENCLATURE

A = Surface area of an element exchanging radiant energy, m^2
A_e = External surface area of the channel wall, m^2
A_H = Pre-exponential factor, homogeneous reaction, s^{-1}
A_W = Pre-exponential factor, catalytic reaction, m s^{-1}
C_{pcb} = Concentration of PCB, mol m^{-3}
Cp = Heat capacity of the gas, J mol^{-1} K^{-1}
Cp_w = Heat capacity of the channel wall, J kg^{-1} K^{-1}
Cp_p = Heat capacity of the thermocouple probe wall, J kg-1 K^{-1}
D = Molecular diffusion coefficient, m^2 s^{-1}
D_k = Constant in diffusion equation, (2.5322 x 10^{-5} Pa m^2 $K^{-1.75}$ s^{-1})
d_e = Equivalent inside diameter, m
E_H = Activation energy for homogeneous reaction, J mol^{-1}
E_W = Activation energy for catalytic reaction, J mol^{-1}
E_b = Black body radiation, W m^{-2}
F_{jk} = View factor between two surface elements *j* and *k*
$[F]$ = Global vector for the temperature or concentration problem
ΔH_R = Heat of reaction, J (mol PCB)$^{-1}$
h_{eff} = Effective heat transfer coefficient for the probe, W m^{-2}
J_j = Radiosity of surface element *j*, W m^{-2}
$[\![J]\!]$ = Global Jacobian matrix for the temperature or concentration problem
K = View factor between an end surface and an interior surface element
k_f = Thermal conductivity of the gas, W m^{-1} K^{-1}
k_x = Thermal conductivity of component x in the channel wall W m^{-1} K^{-1}
k_w = Combined axial thermal conductivity of the channel wall W m^{-1} K^{-1}
k_p = Axial thermal conductivity of the thermocouple probe wall W m^{-1} K^{-1}
k_H = First order rate constant for the homogeneous reaction, s^{-1}
k_W = First order rate constant for the catalytic reaction, m s^{-1}
L = Length of the monolith channel, m
L_D = Entrance length for developing flow, m
L^* = Exterior distance used for probe boundary condition, m
$[\![M]\!]$ = Global matrix for the temperature or concentration problem
m = Number of nodes associated with a finite element
N_i = Number of surface elements comprising the interior surface of the channel
Nu = Nusselt number
n = Coupling iteration number for the temperature-concentration problem
n_g = Number of Gaussian integration points
$[n]$ = Normal vector
P = Pressure, Pa
Q_{gen} = Heat generated by catalytic reaction at the wall, W m^{-2}
Q_{axC} = Heat flux due to axial conduction in the wall, W m^{-2}
Q_{iR} = Heat flux due to internal radiation in the channel, W m^{-2}
Q_{eR} = Heat flux due to external radiation from the furnace (based on R), W m^{-2}
$\hat{Q}_{eR}$ = Heat transfer due to external radiation from the furnace, W

$\hat{Q}_{rC}$ = Heat transfer due to radial conduction across the wall, W
R = Inside radius of the ceramic channel, m
R_2 = Outside radius of the ceramic channel, m
R_3 = Inside radius of the stainless steel tube, m
R_4 = Outside radius of the stainless steel tube, m
R_p = Outside radius of the thermocouple probe, m
r = Radial coordinate, m
r_m = Radial position of maximum velocity (zero shear), m
Re = Reynolds number, based on equivalent diameter
R_g = Gas constant, (8.314 J mol^{-1} K^{-1})
R_H = Rate of the homogeneous reaction, mol m^{-3} s^{-1}
R_W = Rate of the catalytic reaction, mol m^{-2} s^{-1}
ΣR^2 = Sum of the residual square errors
Sh = Sherwood number
s = Distance between two interior surface elements, m
T = Temperature of the gas, K
T_O = Average inlet gas temperature, K
T_L = Average outlet gas temperature, K
$T_{L/2}$ = Average midpoint gas temperature (at $z = 0.5\ L$), K
T_F = Furnace temperature, K
T_{We} = Temperature of the external channel wall surface, K
T_{Wi} = Temperature of the internal channel wall surface, K
T_P = Temperature of the probe wall, K
T_{ref} = Reference temperature used for probe boundary condition, K
T_{OR} = Entrance temperature for internal radiation, K
T_{LR} = Exit temperature for internal radiation, K
t = time, s
V = Velocity vector, m s^{-1}
$\langle V_{Zo} \rangle$ = Average inlet velocity, m s^{-1}
w = Length of a finite element on the wall in the discretized domain, m
w_k = Gaussian weight coefficient for integration point k
wt = Weight factor used to improve model convergence
X_{pcb} = Outlet fractional conversion of PCB
Y_{pcb} = Mole fraction of PCB
Y_{pcbo} = Average inlet mole fraction of PCB
Y_{pcbL} = Average outlet mole fraction of PCB
z = Axial distance, m

Greek Symbols

α = Coefficient of thermal expansion for ceramic (*c*) or stainless steel (*ss*), K^{-1}
β = w_k/w_j
Γ = Boundary of a domain
γ_1 = z/w
γ_2 = $(L-z)/w$
$[\Delta T]$ = Correction vector for temperature calculated using Newton method, K
$[\Delta Y]$ = Correction vector for mole fraction calculated using Newton method
Δt = Time step for transient solution, s
δ_w = Total channel wall thickness, m
δ_p = Thermocouple probe wall thickness, m
ϵ_{wi} = Emissivity value of the inside channel wall
ϵ_{we} = Emissivity value of the external channel wall
ϵ_p = Emissivity value of the thermocouple probe wall
ρ = Density of the gas, mol m^{-3}
ρ_w = Density of the channel wall, kg m^{-3}
ρ_p = Density of the thermocouple probe wall, kg m^{-3}
σ = Stefan-Boltzmann constant, (5.67×10^{-8} W m^{-2} K^{-4})
η = $s/(2w)$
Θ_1 = z/R
Θ_2 = $(L-z)/R$
λ_w = Radial channel wall conduction resistance, K m^2 W^{-1}
ξ = s/R
(ξ,η) = Coordinates for finite element reference domain
μ = Viscosity of the gas, kg m^{-1} s^{-1}
ϕ = w/R
ψ = Galerkin weight function, equal to the interpolation function
Ω = Solution domain

Abbreviations

B.C. = Boundary condition
Exp. = Experimental
HPLC = High performance liquid chromatography
Model = Mathematical model of the single channel monolith reactor
PCB = Polychlorinated biphenyls / Aroclor 1242 commercial mixture
PCDD = Polychlorinated dibenzodioxins
PCDF = Polychlorinated dibenzofurans
PDE = Partial differential equation
RK4 = Runga-Kutta method
1-D = One dimensional
2-D = Two dimensional

1

INTRODUCTION

This research concerns the mathematical modelling of a catalytic reactor used for the combustion of polychlorinated biphenyls. In this chapter the objectives of this study are described and a brief introduction is given on topics relevant to the work, thus providing the reader with some background information. In particular, the areas of polychlorinated biphenyls, hazardous waste destruction techniques and a review of recent work that has been published in the literature concerning combustion of chlorinated wastes is presented.

1.1 Polychlorinated Biphenyls - What are They and Why Should We Destroy Them ?

Polychlorinated biphenyls (PCB) are mono- or polychlorinated derivatives of biphenyl. There are 209 different forms of PCB that theoretically exist [1], one experimental study has identified 69 isomers in a particular sample of Aroclor 1254 [2]. A comprehensive review on the properties, health risks, legislation and destruction technology pertaining to PCB has been completed by Crittenden *et al.* [3,4].

As a result of their excellent dielectric and fire resistant properties, PCB have been widely used in electrical equipment such as transformers and capacitors since the 1930's. They have also been used extensively as heat exchange and hydraulic fluids. Commercial PCB products contain a mixture of isomers and were manufactured under trade-names such as Monsanto's Aroclor, Askarel and Pyroclor. Products were classified by their chlorine content *eg* Aroclor 1242 (the mixture of PCB used in this study), the last two digits signify that it contains an average 42 weight % chlorine. Depending on their chlorine content they are either mobile oils, viscous liquids or sticky resins. The marketed product usually contained trace amounts of other chemicals such as trichlorobenzene, polychlorinated napthalenes and dibenzofurans. Figure 1-1 shows the chemical structure of an example PCB.

Concern over the toxic effects of PCB led to an end in production during the 1970's, by which time over one million tons had been produced [5]. A significant fraction of this still exists today, either in storage, transformer service, or as a contaminant in the environment. The long-term risks from exposure to PCB, as with many other chemicals classified as toxic, are largely unknown. Public concern about the toxic nature of PCB was very much influenced by a rice poisoning incident known as *Yusho* in Japan. Rice oil, contaminated with 1000 ppm PCB, was ingested by about 1200 people. Patients were mainly treated for skin and liver complaints and after subsequent years there was some evidence suggesting excessive patient death from cancer [6]. However, investigations that followed the incident proposed that the illness was actually caused by dibenzofurans present in the oil [7].

PCB have a low volatility so industrial exposure by absorption through the skin is of more concern than absorption through inhalation. They have also been associated with liver disease and chloracne, a reversible skin condition. The International Agency on Cancer also describes PCB as suspected human carcinogens [8]. The American Conference of Governmental Industrial Hygienists (ACGIH) gives the following occupational threshold limit values (TLV), for two of the most common PCB [9]:

	42% Chlorine	**54% Chlorine**
Time-weighted average (TLV-TWA)*	1 mg m^{-3}	0.5 mg m^{-3}
Short-term exposure limit (TLV-STEL)†	2 mg m^{-3}	1 mg m^{-3}

* Defined as the time-weighted average concentration in workplace air over an eight hour work-day.

† Defined as a 15 minute time-weighted average concentration in workplace air which should not be exceeded.

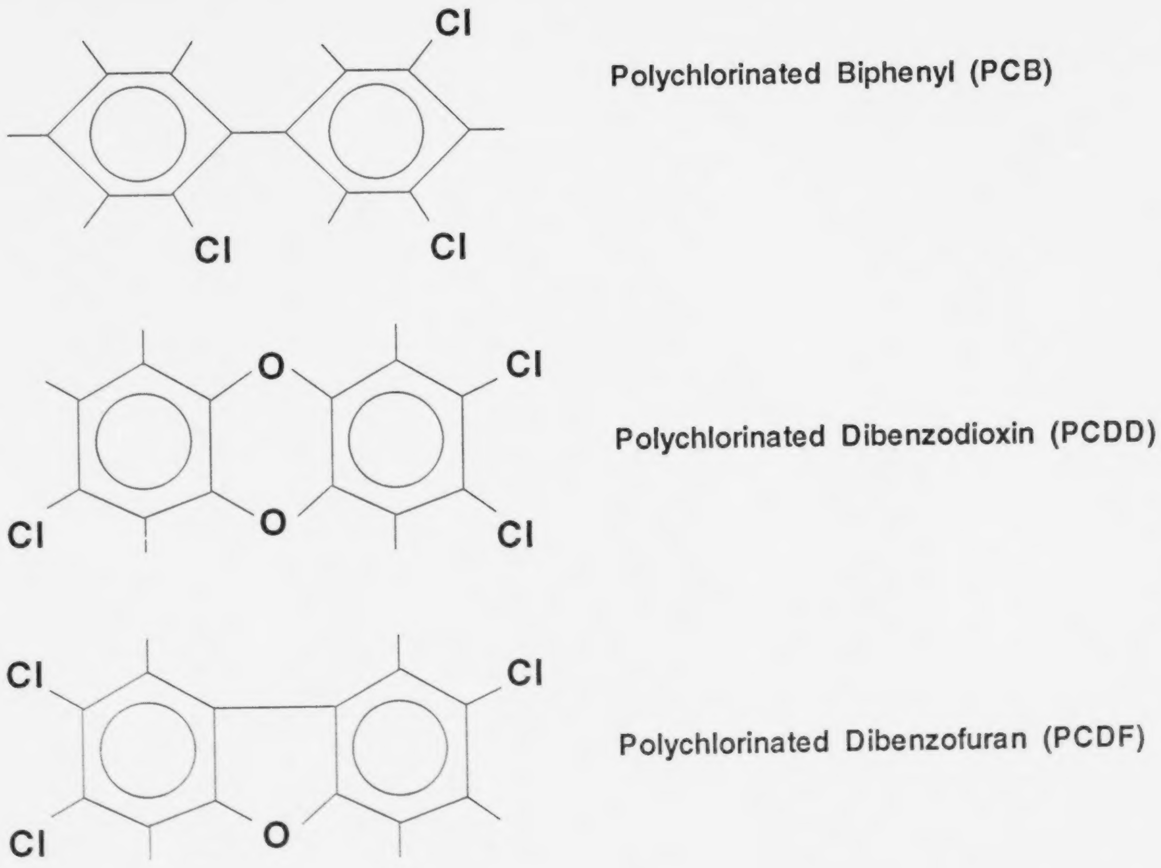
Cl
Cl
Cl
Polychlorinated Biphenyl (PCB)
O
O
Cl
Cl
Cl
Polychlorinated Dibenzodioxin (PCDD)
Cl
Cl
Cl
Cl
O
Polychlorinated Dibenzofuran (PCDF)

Figure 1-1. Chemical Structure of an example PCB, PCDD and PCDF.

The characteristic inertness of PCB renders them resistant to environmental degradation and, as they are soluble in fat tissue, bio-accumulative in the food chain. Fifty years of their uncontrolled use has caused widespread contamination of the environment, via either runoff from roads on which a PCB containing oil was used as a dust-suppressant, leaks of PCB from installed equipment, spills during transport, landfill disposal or incomplete destruction [10]. Pollution of water systems is particularly hazardous, studies have shown low and high forms of aquatic life to show serious toxic responses [11,12,13]. Most PCB released in the hydrosphere are expected to end up either absorbed onto sediment or resting as sludge at the bottom of rivers, lakes and oceans. Atmospheric transport also plays a major role in the worldwide dissemination of PCB [14].

Legislation on PCB has been effected as much by public opinion as the magnitude of the risk that PCB present. They were among the earliest class of chemicals to be identified as hazardous and to be restricted by law. As such, they have become in many people's mind the epitome of hazardous waste. In Europe a number of EEC directives restrict the use and control disposal of PCB. A North Sea Conference Declaration requires all Member States "to phase out the use and to destroy in an environmentally safe manner all identifiable PCB, with the aim of complete destruction by 1995, and by the end of 1999 at the latest" [15]. In Canada the *Environmental Contaminants Act* (1976) and its recent amendments, restrict the use of PCB and controls their phase-out throughout the country. It restricts the use of PCB to existing electrical equipment and sets a maximum of 50 wt. ppm of PCB that may be contained in specified electrical equipment at the time of import, manufacture or sale [16].

1.2 Current PCB Disposal Methods

With the phasing out of the use of PCB completely and the option of long-term storage or deep well disposal generally being considered as unsatisfactory, there is a need for environmentally safe destruction methods. Although there are many references in the literature to new techniques for the destruction of PCB wastes, not many of them have been adopted. Environment Canada has currently recommended chemical treatment and high temperature incineration as destruction methods that are satisfactory [17].

Chemical treatment is mainly applied to the treatment of low concentration PCB (less than 5000 ppm) contaminated mineral oil. The process is usually based on the use of sodium, which reacts selectively with the chlorine of the PCB molecule to form sodium chloride and a non-halogenated biphenyl. An alternative method using PEG/KOH (polyethylene glycol/potassium hydroxide) as the reagent is also becoming widely used. The resulting mineral oil (less than 50 ppm PCB) can either be reused in electrical equipment or disposed of by conventional means.

For high concentration PCB waste, high temperature incineration is the only approved technology [17]. Some of the established processes are liquid injection, rotary kiln and high efficiency boiler incineration. Rotary kiln incineration is one of the most versatile technologies and can handle both liquid and solid waste materials. As PCB possess a high thermal stability, severe operating conditions have to be employed to ensure complete destruction. The following operating standards for incinerators are reported [4,16]:

i) A PCB destruction efficiency of not less than 99.9999% to be achieved.
ii) A mean residence time of at least 2 seconds with 3% minimum excess oxygen content.
iii) Operation at sustained temperatures greater than 1200°C.

Generally, air or oxygen is used for the oxidation and auxiliary hydrocarbon fuel is used to maintain the high temperatures required for complete combustion. Hydrogen chloride, one of the combustion by-products, must be removed from the effluent gases by scrubbing devices before being discharged to the environment. It is important to limit the amount of free chlorine produced in the process as this is not only more corrosive than

HCl, but is also less easy to remove by scrubbing. The amount of excess oxygen influences the formation of Cl_2, as can be from the Deacon reaction [18]:

$$2\ H_2O\ +\ Cl_2 \Leftrightarrow 2\ HCl\ +\ 0.5\ O_2$$

There are also strict regulations on the particulate, NO_x, dioxin and furan content of the effluent gases. Figure 1-2 shows a schematic of a typical rotary kiln hazardous waste incinerator. In the future there may be a greater trend to use mobile incineration facilities as the approval for stationary incineration plants is slow. These mobile systems have been used extensively in the U.S. and require only 2-6 weeks to set up on site [19].

There are a number of industrial processes which have demonstrated the necessary temperature, residence time and other conditions required to completely destroy PCB. In particular cement kilns are advantageous since the crushed limestone used in the process also neutralizes the HCl generated by the thermal destruction of PCB, this alleviates the need for further addition of a neutralizing agent; the waste ash and particulates are combined into the finished cement product. These processes also have large throughputs in which the PCB waste can be fed at only a small fraction of the overall feed rate [20]. St. Lawerence Cement claimed that they could destroy PCB and shredded scrap tires in their kiln and still maintain emissions below standards [21]. The disadvantages of using cement kilns include the need to add proper waste handling and containment facilities to the existing plant; the need for training of staff in procedures for waste handling; and the likely public opposition to the use of the facility for a purpose not originally intended.

1.3 Catalytic Combustion and Monolith Reactors

Prasad *et al.* [22] have given an excellent review on the principles of catalytic combustion, modelling aspects and guidelines for the selection of catalyst and support. The objective of introducing a catalyst in the combustor is to carry out heterogeneous oxidation on the catalyst surface. By proper selection of a catalyst, the activation energy for the heterogeneous reaction is much lower than that for the purely homogeneous case.

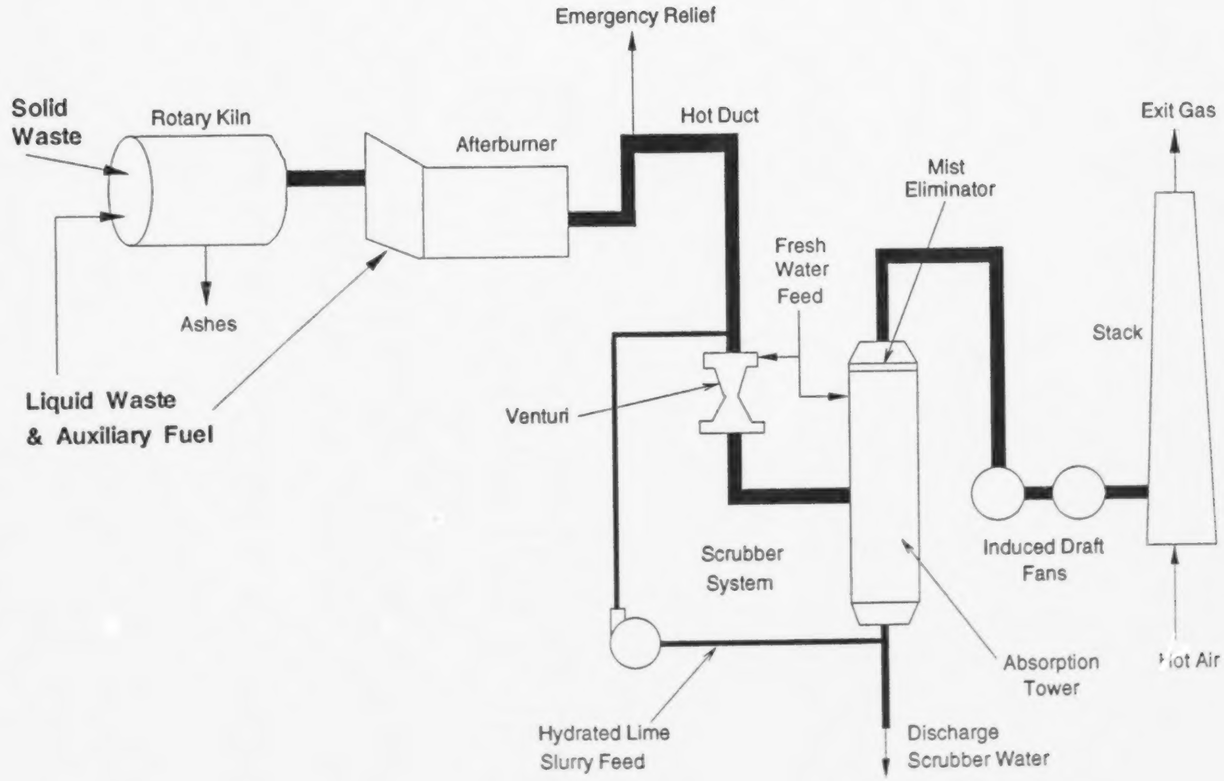
Emergency Relief
Solid Waste
Rotary Kiln
Afterburner
Hot Duct
Exit Gas
Mist Eliminator
Fresh Water Feed
Ashes
Stack
Liquid Waste & Auxiliary Fuel
Venturi
Scrubber System
Induced Draft Fans
Absorption Tower
Hot Air
Hydrated Lime Slurry Feed
Discharge Scrubber Water

Figure 1-2. Schematic of a typical rotary kiln hazardous waste incinerator [11].

As the surface temperature of the catalyst increases along the reactor bed, a reactor will typically exhibit the regimes illustrated in Figure 1-3. Near the reactor entrance, where the catalyst temperature is low, the reaction rate is controlled by the surface kinetics which increase exponentially with temperature. At elevated temperatures, the surface reaction rate can be so high that the overall process is limited by the rate of species transport to the surface. In this region the reaction rate is a weak function of temperature since the mass transfer coefficient is fairly insensitive to temperature. As the surface reaction proceeds further, the bulk gas temperature increases to a value where the homogeneous gas phase reactions occur simultaneously with the catalytic reaction [22].

Catalytic combustion has seen many industrial applications in the fields of pollution control and also heat and power generation. Due to considerably lower operating temperatures, catalytic combustion offers the following strong advantages as an alternative or complimentary PCB destruction method to incineration:

i) Reduction in the support fuel required to sustain the combustion process.
ii) A design that uses less expensive and easily obtainable materials of construction.
iii) A reduction in the amount of NO_x formation.
iv) The thermal inertia of the catalyst support means that improved temperature control can be achieved.
v) Safer operation of the process.

However, at this time there is little published information on industrial catalytic combustors used for the destruction of hazardous wastes. Benson [23] describes a *Catoxid* process for the large scale destruction of chlorinated wastes. Chlorinated byproduct from the manufacture of vinyl chloride monomer is fed into the catalytic fluid bed reactor that operates at temperatures below 540°C. Rockwell International describes a fluid bed combustor followed by a catalytic afterburner used for PCB combustion [24]. They claim that the process can achieve a destruction efficiency of more than 99.9999% and operates at half the temperature required by other

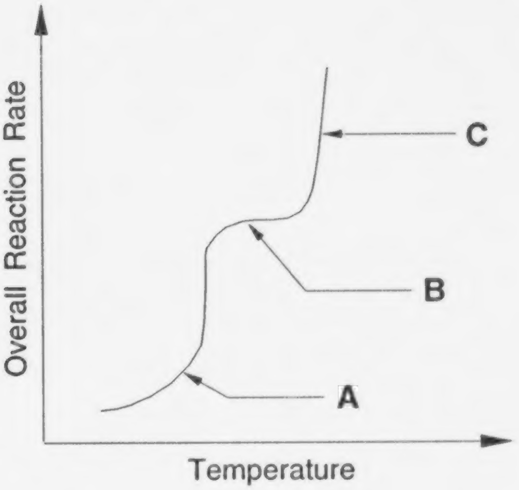

Region A : Kinetic Controlled Catalytic Reaction

Region B : Mass Diffusion Controlled Catalytic Reaction

Region C : Catalytically Supported Homogeneous Reaction

Figure 1-3. Catalytic combustion regimes [22].

incineration processes. The Rockwell system uses chromic oxide catalyst, deposited on alumina, and granular sodium carbonate to neutralise the acid in situ in the dry state.

There has been increasing interest in the use of catalytic monolith reactors [25] and there has been numerous applications in the field of pollution control, most notably the automobile catalytic converter [26,27]. There is also interest in using catalytic monolith reactors as the combustion chambers for gas turbines, since the lower combustion temperatures would mean a reduction in NO_x formation.

Monolith reactors consist of a honeycomb structure of metal or ceramic that contains hundreds of parallel channels of the order of 1 mm in diameter. These channels can be square, triangular or circular in cross-sectional shape. Studies have shown that the chosen channel geometry can effect the pressure drop, mechanical strength and the thermal shock resistance of the monolith [25]. The catalyst is usually coated onto the walls of the channels by passing a washcoat of alumina, Al_2O_3, previously impregnated with the catalyst, through the structure. The Al_2O_3 washcoat strongly adheres to the channel wall and serves to increase the effective surface area for heterogeneous reaction. The washcoat also enables the deposition of a uniform and stable catalyst coat.

For hazardous waste combustion the catalytic monolith reactor offers several advantages over more traditional reactor configurations:

i) Low reactor pressure drop.
ii) High structural integrity.
iii) Relatively high surface-to-volume ratio.
iv) Minimal resistance to particulates present in a waste stream.
v) Low axial dispersion and radial heat flow.

1.4 Combustion of Chlorinated Wastes - A Literature Survey

The combustion of chlorinated wastes has been the subject of many recent research programs. Most of these studies have concentrated on achieving a better understanding of the reaction steps involved in the thermal destruction of chlorinated wastes and the formation of hazardous organic compounds, in particular polychlorinated dibenzofurans (PCDF) and polychlorinated dibenzodioxins (PCDD) [18]. Sethuraman *et al.* [28] and Graham *et al.* [29], both completed separate experimental studies on the gas phase oxidation of chlorobenzene in a flow reactor and identified the combustion by-products and proposed plausible reaction sequences. Others have studied mechanistic reaction models based on thermal-chemical principles to gain an understanding of the pathways to dioxin formation [30,31]. Such processes are known to proceed subsequent to the combustion period and at relatively low temperatures with fly ash being the important mediator. Ruby *et al.* [32] studied the oxidation of a mixture of PCB over a temperature range 500 - 1000°C using a 1 mm diameter flow reactor. They found an increase in the oxygen available for combustion resulted in an increase in PCDF formation.

Thermal stability and kinetic data for the homogeneous combustion of selected chlorinated wastes in tubular reactors has been reported in the literature [33,47,48] some of the data were used in this research for comparison purposes. However, previous research on the catalytic combustion of chlorinated hydrocarbons is scarce, particularly for the oxidation of PCB. Manning [49] studied the oxidation of chloroethylenes in a fluid bed reactor bed reactor with a commercially available chromia on alumina catalyst. The experimental data yielded a rate expression, first order in the chlorocarbon species and between zero and first order in oxygen, over the temperature range 350 - 550°C. Senkan [34] obtained analogous results using a similar catalytic reactor system but for the oxidation of CH_3Cl. Greene and Subbanna [35,50] investigated various catalysts for the oxidation of Aroclor 1254 (a commercial grade of PCB) in a monolithic reactor. Results from these research programs were taken into account in this study, during the modelling of the combustion kinetics of Aroclor 1242 (the PCB feed mixture).

1.5 Project Outline and Objectives

The objective of this study was to develop a mathematical model of the single channel monolith reactor used for the catalytic combustion of Aroclor 1242 (a PCB mixture) at the School of Chemical Engineering at the University of Bath. In this way it was hoped to gain some insight in the following areas:

i) The important effects that need to be included in a mathematical model, to describe accurately the reactor system.
ii) The homogeneous and catalytic oxidation kinetics of PCB.
iii) The heat and mass transfer phenomena that exist in the channel of a monolith reactor.

The catalytic combustion of a commercial mixture of PCB, known as Aroclor 1242 (42% chlorine by weight), was investigated using a single channel monolith reactor. Combustion experiments were previously carried out by Dr. S.P. Perara at the University of Bath. Since homogeneous combustion is always present, the first stage of the work was to determine the homogeneous kinetics. This was achieved by carrying out experiments in an uncoated tubular reactor. Homogeneous and catalytic combustion was then studied using a channel coated with a chromia catalyst. In developing a model for the reactor system the phenomena of both homogeneous and catalytic combustion were addressed.

1.6 Layout of the Thesis

This thesis is structured so that the reader can first obtain a brief background in the area of this research and the previously completed experimental work. This is followed by a description of how the modelling work progressed and the conclusions drawn at particular stages during this study. In this way the importance of including different effects in the mathematical model can be comprehensively shown.

An overview of the homogeneous and catalytic combustion experiments and the experimental apparatus is given in Chapter 2. This is important as it explains why certain effects were incorporated in the model of the reactor. In Chapter 3 the mathematical model is discussed in detail, including the formulation of the equations, the solution algorithm employed and the development of a comprehensive model. The major portion of this work is given in Chapter 4, where the results obtained are presented and discussed. This Chapter is divided into two sections; the modelling of the uncoated channel experiments (homogeneous combustion); the modelling of the catalyst coated channel (homogeneous and catalytic combustion). Finally, Chapter 5 draws conclusions from previous chapters and recommends possibilities for future work.

2

EXPERIMENTAL WORK

The experimental work in this study was completed by Dr. S.P. Perera in conjunction with the Reaction Engineering research group of the School of Chemical Engineering at the University of Bath, United Kingdom. It is presented and summarised in this chapter to provide clarity in explaining this study.

The combustion of Aroclor 1242 PCB was carried out experimentally in a single channel monolith reactor. Data were obtained in a reactor of 15 mm inside diameter and lengths varying from 15 to 31 cm which was installed in a high temperature furnace. Homogeneous combustion experiments were first carried out in an uncoated tubular reactor. Homogeneous and catalytic combustion was then studied using a channel coated with a chromia catalyst. The properties of Aroclor 1242 the PCB mixture used as the feedstock for these experiments is given in Table 2-1.

2.1 Experimental Apparatus

The experimental apparatus used in this study is shown in Figures 2-1(a) and 2-1(b), complete experimental details can be found in earlier work [36,37]. The PCB fluid was stored in a 25 ml reservoir maintained at 20°C, whence it was pumped through a vaporiser, where a small purge of nitrogen was added to stabilise any fluctuations. This mixture was passed to a preheater before being mixed with a hot air stream. The PCB/air/N_2 mixture was then fed into the reactor which was housed in an electrically heated furnace.

Table 2-1. Properties of Aroclor 1242 PCB.

commercial trade-name	Aroclor 1242
chlorine by weight	42 %
supplied by	Rechem International Ltd, U.K.
PHYSICAL PROPERTIES :	
appearance	clear, mobile oil
average molecular weight	261
liquid density (@ 25 °C)	1380 kg m^{-3}
distillation range	325 - 366°C
flash point (open cup)	176 - 180°C
fire point (open cup)	none to boiling point
CHEMICAL PROPERTIES :	
representative chemical formula	$C_{12}H_{6.9}Cl_{3.1}$
ΔH_R heat of reaction @298 K †	- 5,558 kJ (mole of PCB)$^{-1}$
gas heat capacity constants *	A - 33.26
	B 9.052 x 10^{-1}
	C - 6.012 x 10^{-4}
	D 1.466 x 10^{-7}

† Calculated from an estimated value of the heat of formation for Aroclor 1242 based on the group contribution method [37,38]

* Cp of PCB (J mol^{-1} K^{-1}) = A + BT + CT^2 + DT^3, constants calculated using group contribution method [39]

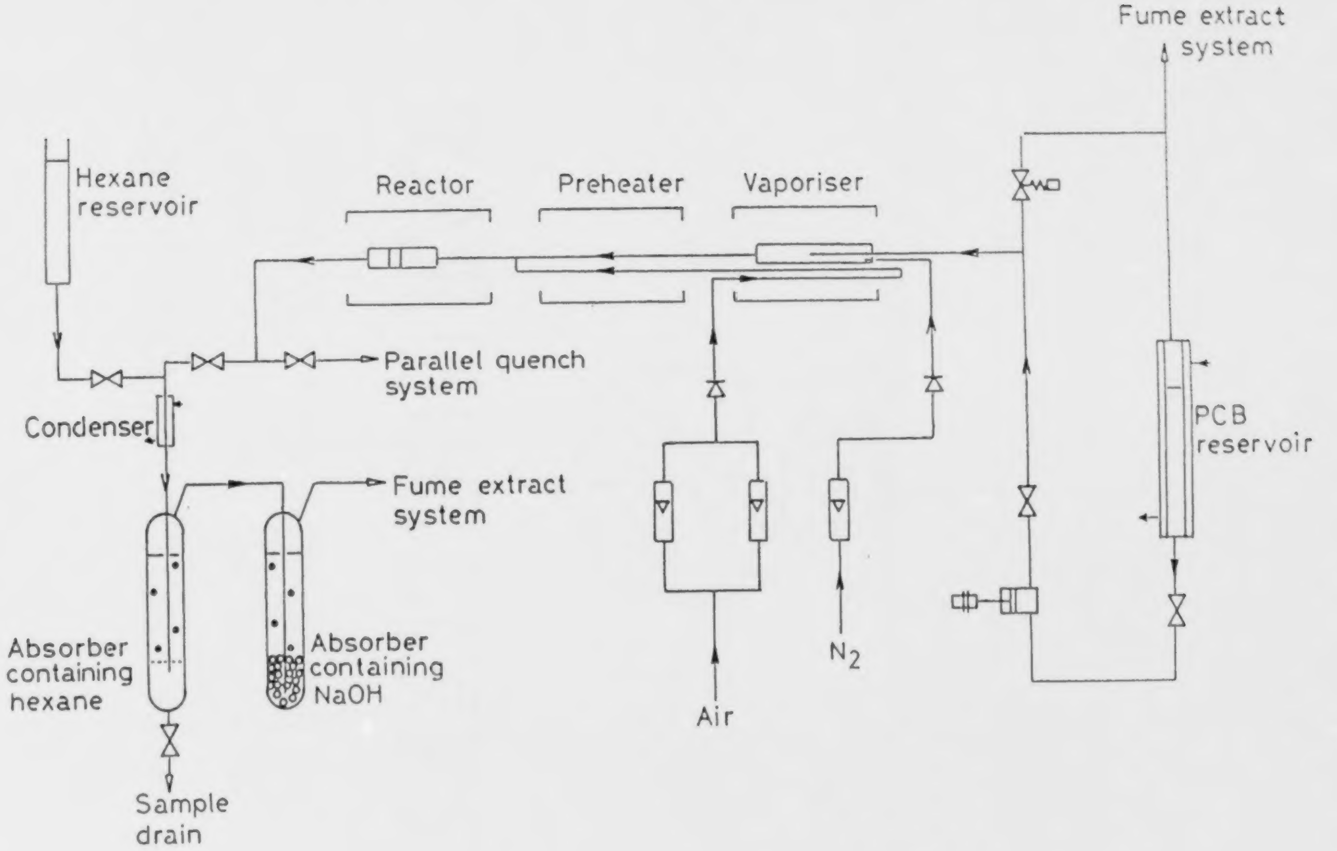
Fume extract system
Hexane reservoir
Reactor
Preheater
Vaporiser
Parallel quench system
Condenser
Fume extract system
PCB reservoir
Absorber containing hexane
Absorber containing NaOH
Sample drain
Air
N_2

Figure 2-1(a). Flow diagram of experimental apparatus.

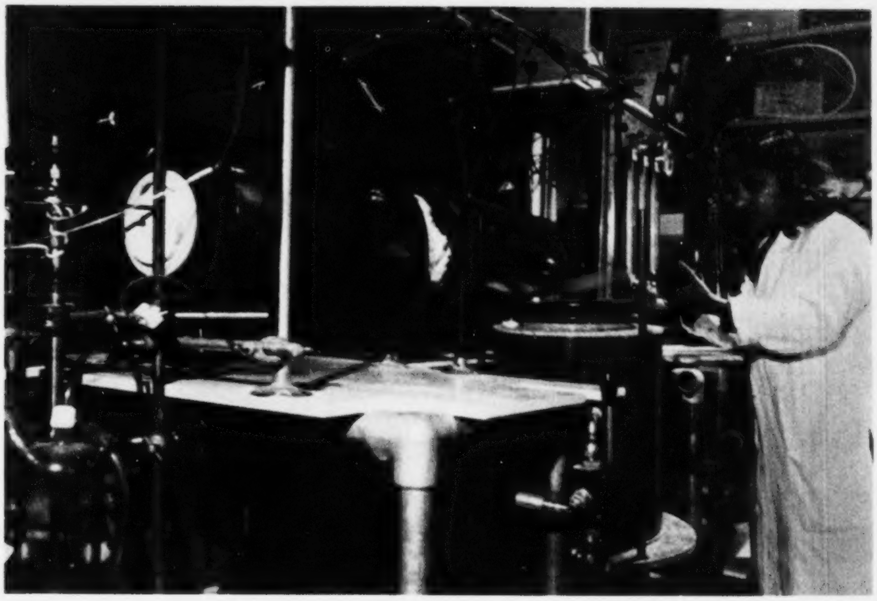

Figure 2-1(b). Photograph of experimental apparatus.

From right to left: rotameter panel; preheater; reactor furnace; quench system.

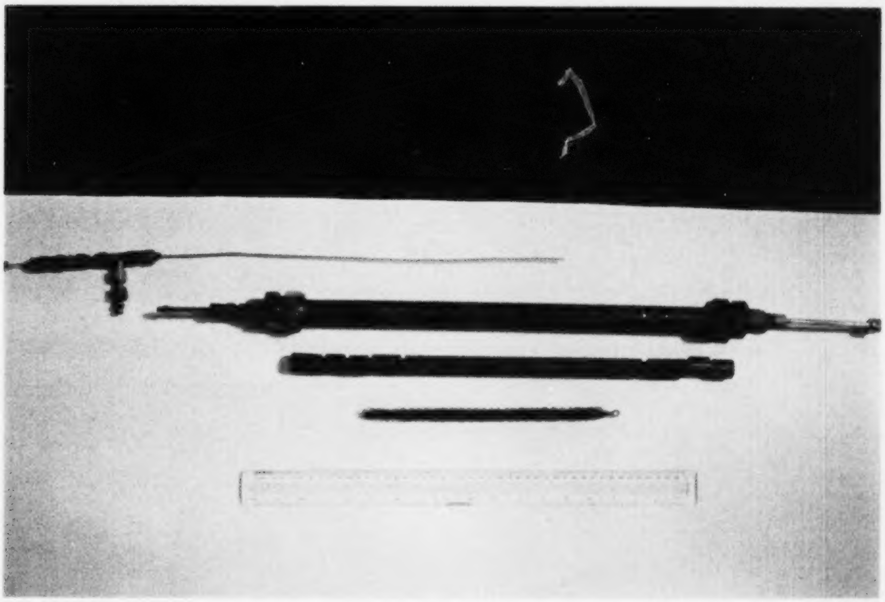

Figure 2-1(c). Photograph of the single channel monolith reactor.

From top to bottom: thermocouple and sleeve; stainless steel tube housing; ceramic channel, manifold and spacers; insert (not used in this study); 30 cm ruler.

Finally the combustion products from the reactor were directed into one of two quench systems, where the unreacted PCB and other liquid products were collected for analysis. The gaseous stream was passed through three absorbers, two of which contained hexane and one which contained sodium hydroxide. An experimental run involved first letting the reactor obtain steady-state conditions and then the combustion products from the reactor would be directed to the second quench system to be collected for about 30 minutes. Analysis of the total concentration of PCB remaining in the collected liquids was subsequently determined by high performance liquid chromatography (HPLC).

Details of the single channel monolith reactor used for the combustion experiments are shown in Figures 2-1(c) and 2-2 and also in Table 2-2. The reactor consisted of a ceramic channel supported externally by a stainless steel tube. Between the stainless steel and ceramic wall there was a uniform air gap of about 0.6 mm. Axial centre-line temperature profiles were measured by means of a chromel-alumel thermocouple that could be traversed along the length of the reactor channel inside a stainless steel sleeve, see Figure 2-1(c). The sleeve served to isolate the thermocouple from the combustion reactions proceeding in the channel. Stainless steel manifolds at the reactor entrance and exit provided good flow distribution across the entrance and held the thermocouple sleeve in position. The manifolds consisted of a plate perforated with holes of less than 1 mm diameter. The reactor was operated at inlet temperatures > 450°C (723 K) and at atmospheric pressure.

2.2 Homogeneous Combustion Experiments

A series of experiments was performed in a 25 cm length ceramic channel to assess the extent of homogeneous reaction at the temperatures to be studied. In one set of experiments, the inlet gas temperature was maintained at approximately 753 K, whilst the inlet PCB concentration was varied from 3700 - 6600 ppm. The outlet conversion of PCB and the axial gas temperature profile were recorded for each run, the results are summarised in Table 2-3. Figure 2-3 illustrates typical axial temperatures obtained from a steady-state run; these profiles exhibit a maximum near the midpoint of the reactor.

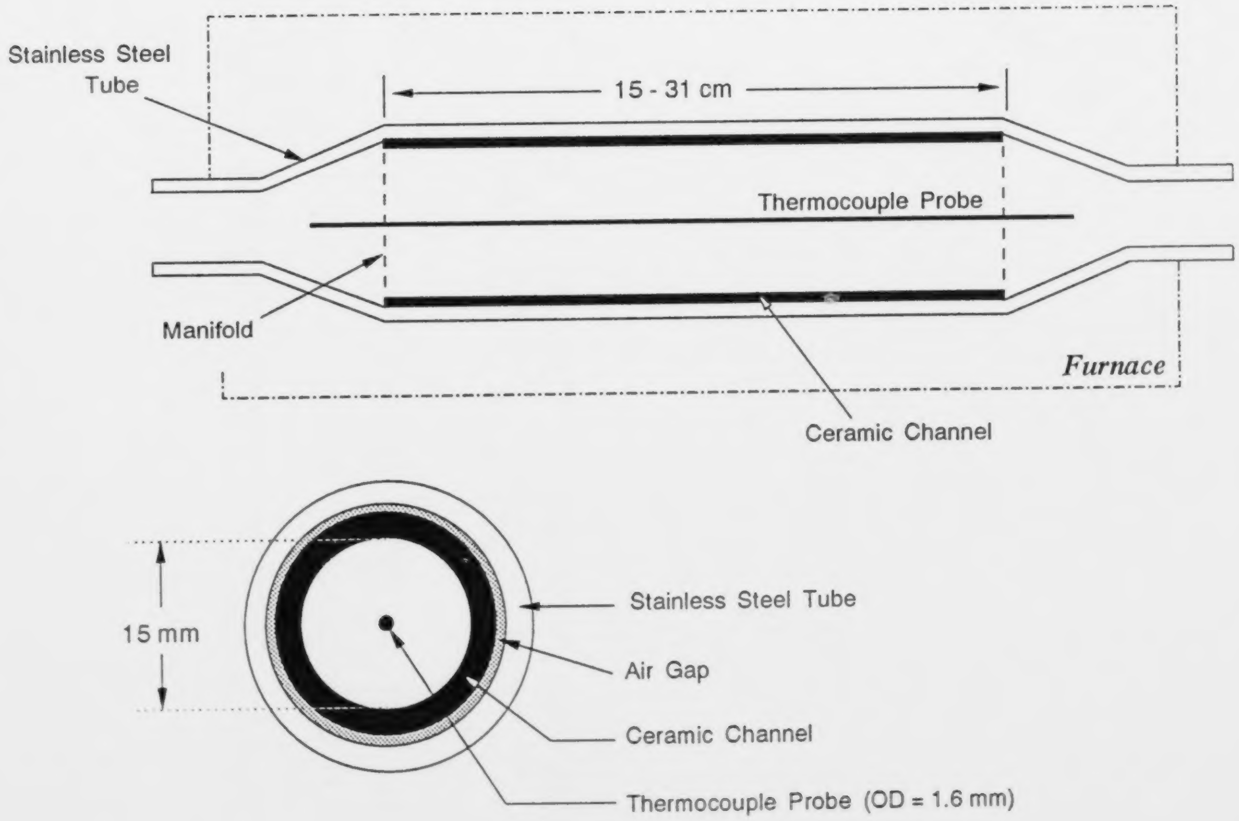
Stainless Steel Tube
15 - 31 cm
Thermocouple Probe
Manifold
Furnace
Ceramic Channel
15 mm
Stainless Steel Tube
Air Gap
Ceramic Channel
Thermocouple Probe (OD = 1.6 mm)

Figure 2-2. Schematic of the single channel monolith reactor.

Table 2-2. Details of the reactor assembly.

CERAMIC CHANNEL :	
commercial trade-name	pormulit
material	alumina silicate (porous)
inside diameter	15 mm
outside diameter	20 mm
TUBE HOUSING :	
material	stainless steel
inside diameter	21.1 mm
outside diameter	25.5 mm
THERMOCOUPLE SLEEVE :	
material	stainless steel
inside diameter	0.79 mm
outside diameter	1.59 mm
FURNACE :	
inside diameter	115 mm
outside diameter	300 mm
length	460 mm

Table 2-3. Homogeneous combustion results at varying inlet PCB concentrations.

Experiment number	pcb1 (5, 1a)	pcb2 (5, 1b)	pcb3 (5, 1e)	pcb4 (5, 1c)	pcb5 (5, 1d)
PCB flowrate (cc min^{-1} @ 20°C)	0.18	0.21	0.32	0.28	0.30
T_O Inlet temperature (K) †	746	755	749	753	753
T_F Furnace temperature (K)	843	843	843	838	838
$\langle V_{ZO} \rangle$ Average inlet velocity (m s^{-1} @ T_O) *	1.493	1.511	1.506	1.510	1.511
Y_{pcbo} Inlet PCB mole fraction (x 10^6)	3727	4345	6606	5785	6196
Y_{pcbL} Outlet PCB mole fraction (x 10^6)	2926	3289	4294	3830	4678
X_{pcb} Outlet conversion of PCB	0.215	0.243	0.350	0.338	0.245

z, Axial distance (cm)	Measured axial centre-line temperature (K)				
0	773	788	775	782	781
2	788	805	792	796	795
4	796	813	799	802	802
6	801	817	805	806	806
8	804	820	809	809	809
10	807	821	813	811	811
12	808	820	814	812	812
14	809	818	814	812	811
16	808	814	811	809	809
18	805	808	807	804	805
20	799	800	800	800	800
22	787	788	790	791	791
24	768	770	776	777	777
26	737	734	743	746	747

† Temperature measured upstream of reactor entrance using thermocouple probe.

* Average inlet velocity based on the cross-sectional area of the annulus and the inlet gas temperature.

Experimental details: air flow = 5.5 l min^{-1} @ 15°C; N_2 flow = 0.5 l min^{-1} @ 15°C;
L = 25 cm; uncoated channel; series #5 experiments.

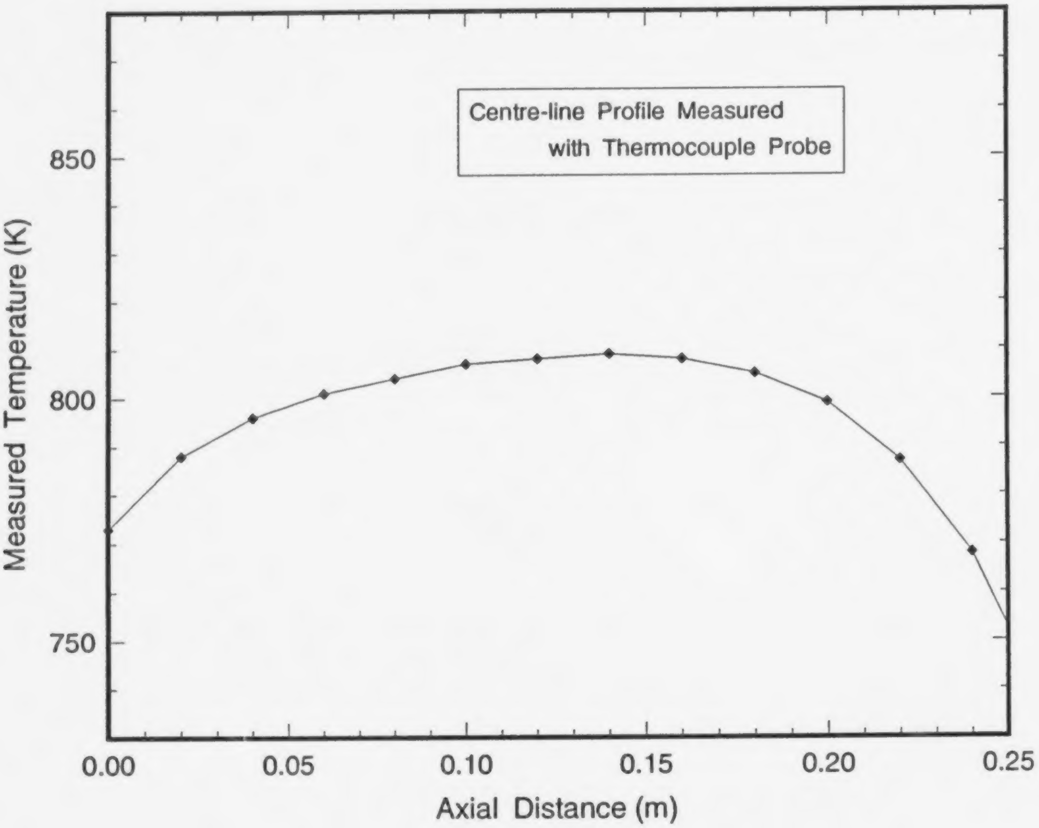

Experiment number: pcb1 (5, 1a)

Figure 2-3. Measured axial centre-line temperature for a homogeneous combustion run.

In the second set of experiments the inlet concentration of PCB was maintained at approximately 5500 ppm, whilst the inlet temperature was varied from 800 - 1060 K. These results are summarised in Table 2-4.

2.3 Catalytic Combustion Experiments

Catalytic combustion experiments were performed with a ceramic channel coated with a chromia catalyst at tube lengths of 15 cm, 20 cm, 24 cm and 31 cm. For each length the inlet temperature was maintained constant and a series of runs were completed over a range of inlet PCB concentrations. As before, the outlet conversion of PCB and the axial temperature profile were recorded at steady-state conditions. A summary of the results of these experiments are presented in Table 2-5(a) and 2-5(b). When compared with the homogeneous experiments, it is evident that catalytic combustion achieves a substantially higher conversion of PCB. Figure 2-4 shows experimentally measured temperature profiles at the different reactor lengths, these runs all had the same inlet PCB mole fraction and inlet gas velocity.

Table 2-4. Homogeneous combustion results at varying inlet temperatures.

Experiment number	pcb6 (10, 2b)	pcb7 (10, 2c)	pcb8 (10, 2d)	pcb9 (10, 2e)
PCB flowrate (cc min^{-1} @ 20°C)	0.26	0.28	0.26	0.265
T_O Inlet temperature (K) †	798	902	903	1031
T_F Furnace temperature (K)	873	973	973	1073
$\langle V_{Zo} \rangle$ Average inlet velocity (m s^{-1} @ T_O) *	1.600	1.809	1.809	2.114
Y_{pcbo} Inlet PCB mole fraction (x 10^6)	5374	5785	5374	5477
Y_{pcbL} Outlet PCB mole fraction (x 10^6)	3977	2761	2547	2246
X_{pcb} Outlet conversion of PCB	0.26	0.523	0.526	0.59

z, Axial distance (cm)	Measured axial centre-line temperature (K)			
0	812	915	917	1045
2	828	928	930	1055
4	841	939	940	1069
6	850	947	947	1079
8	854	953	953	1092
10	858	959	958	1096
12	861	960	959	1094
14	860	959	958	1092
16	858	956	954	1089
18	853	952	947	1082
20	845	944	939	1075
22	833	929	926	1059
24	818	911	901	1032
26	802	893	888	1012

† Temperature measured upstream of reactor entrance using thermocouple probe.

* Average inlet velocity based on the cross-sectional area of the annulus and the inlet gas temperature.

Experimental details: air flow = 5.5 l min^{-1} @ 15°C; N_2 flow = 0.5 l min^{-1} @ 15°C;
L = 25 cm; uncoated channel; series #10 experiments.

Table 2-5(a). Catalytic combustion results at varying reactor lengths.

Channel Length = 31 cm (2.84 wt % Cr_2O_3 coated tube)

Experiment number	cat3 (3a)	cat3 (3b)	cat3 (3c)	cat3 (3d)	cat3 (3e)	cat3 (3f)	cat3 (3g)
PCB flowrate (cc min^{-1} @ 20°C)	0.30	0.10	0.33	0.26	0.25	0.27	0.28
T_o Inlet temperature (K) †	743	743	743	743	743	743	743
$\langle V_{zo} \rangle$ Inlet velocity (m s^{-1}) *	1.548	1.548	1.548	1.548	1.548	1.548	1.548
Y_{pcbo} Inlet PCB mole fraction x 10^6	6196	2074	6811	5374	5168	5580	5785
Y_{pcbL} Outlet PCB mole fraction x 10^6	1456	819	1117	1220	1509	1060	1018
X_{pcb} Outlet conversion of PCB	0.765	0.605	0.836	0.773	0.708	0.810	0.824

Channel Length = 24 cm (2.41 wt % Cr_2O_3 coated tube)

Experiment number	cat4 (4a)	cat4 (4b)	cat4 (4c)	cat4 (4d)	cat4 (4e)	cat4 (4f)
PCB flowrate (cc min-1 @20°C)	0.260	0.285	0.305	0.290	0.245	0.226
T_o Inlet temperature (K) †	773	773	773	773	773	773
$\langle V_{zo} \rangle$ Inlet velocity (m s^{-1}) *	1.548	1.548	1.548	1.548	1.548	1.548
Y_{pcbo} Inlet PCB mole fraction x 10^6	5374	5888	6298	5990	5066	4675
Y_{pcbL} Outlet PCB mole fraction x 10^6	1381	1425	982	1438	1353	1440
X_{pcb} Outlet conversion of PCB	0.743	0.758	0.844	0.760	0.733	0.692

Channel Length = 20 cm (2.59 wt % Cr_2O_3 coated tube)

Experiment number	cat5 (5a)	cat5 (5b)	cat5 (5c)	cat5 (5d)	cat5 (5e)	cat5 (5f)	cat5 (5g)
PCB flowrate (cc min^{-1} @ 20°C)	0.245	0.280	0.325	0.310	0.210	0.260	0.220
T_o Inlet temperature (K) †	773	773	773	773	773	773	773
$\langle V_{Zo} \rangle$ Inlet velocity (m s^{-1}) *	1.548	1.548	1.548	1.548	1.548	1.548	1.548
Y_{pcbo} Inlet PCB mole fraction x 10^6	5066	5785	6709	6401	4345	5374	4551
Y_{pcbL} Outlet PCB mole fraction x 10^6	1788	1649	959	1504	1582	1650	1698
X_{pcb} Outlet conversion of PCB	0.647	0.715	0.857	0.765	0.636	0.693	0.627

Channel Length = 15 cm (3.28 wt % Cr_2O_3 coated tube)

Experiment number	cat6 (6a)	cat6 (6b)	cat6 (6c)	cat6 (6d)	cat6 (6e)	cat6 (6f)	cat6 (6g)
PCB flowrate (cc min-1 @20°C)	0.260	0.25	0.35	0.24	0.23	0.19	0.12
T_o Inlet temperature (K) †	773	773	773	773	773	773	773
$\langle V_{Zo} \rangle$ Inlet velocity (m s^{-1}) *	1.548	1.548	1.548	1.548	1.548	1.548	1.548
Y_{pcbo} Inlet PCB mole fraction x 10^6	5374	5168	7221	4963	4757	3933	2488
Y_{pcbL} Outlet PCB mole fraction x 10^6	1709	1922	2181	2263	2202	1915	1311
X_{pcb} Outlet conversion of PCB	0.682	0.628	0.698	0.544	0.537	0.513	0.473

† Temperature measured upstream of reactor entrance using thermocouple probe.

* Average inlet velocity based on the cross-sectional area of the annulus and the inlet gas temperature.

Experimental details: Furnace temperature T_F = 838 K; air flow = 5.5 l min^{-1} @ 15°C; N_2 flow = 0.5 l min^{-1} @ 15°C; catalyst coated channel.

Table 2-5(b). Axial temperature profiles for catalytic combustion experiments

z, Axial distance (cm)	Measured axial centre-line temperature (K)			
Experiment number Channel Length (cm)	(3d) 31	(4a) 24	(5f) 20	(6a) 15
0	739	785	820	841
2	815	846	847	871
4	855	851	861	880
6	870	868	868	884
8	879	883	873	887
10	886	887	876	888
12	891	889	879	885
14	894	884	876	876
16	895	883	872	854
18	893	871	860	
20	886	872	828	
22	872	859		
24	854	838		
26	835	794		
28	817			
30	796			
32	751			

Experimental details: Furnace temperature T_F = 838 K; air flow = 5.5 l min^{-1} @ 15°C; N_2 flow = 0.5 l min^{-1} @ 15°C; catalyst coated channel; $Y_{pcbo} = 5.374 \times 10^{-3}$; $\langle V_{Zo} \rangle = 1.548$ m s^{-1}; T_O = 743 K for (3d) and 773 k for (4a), (5f), (6a).

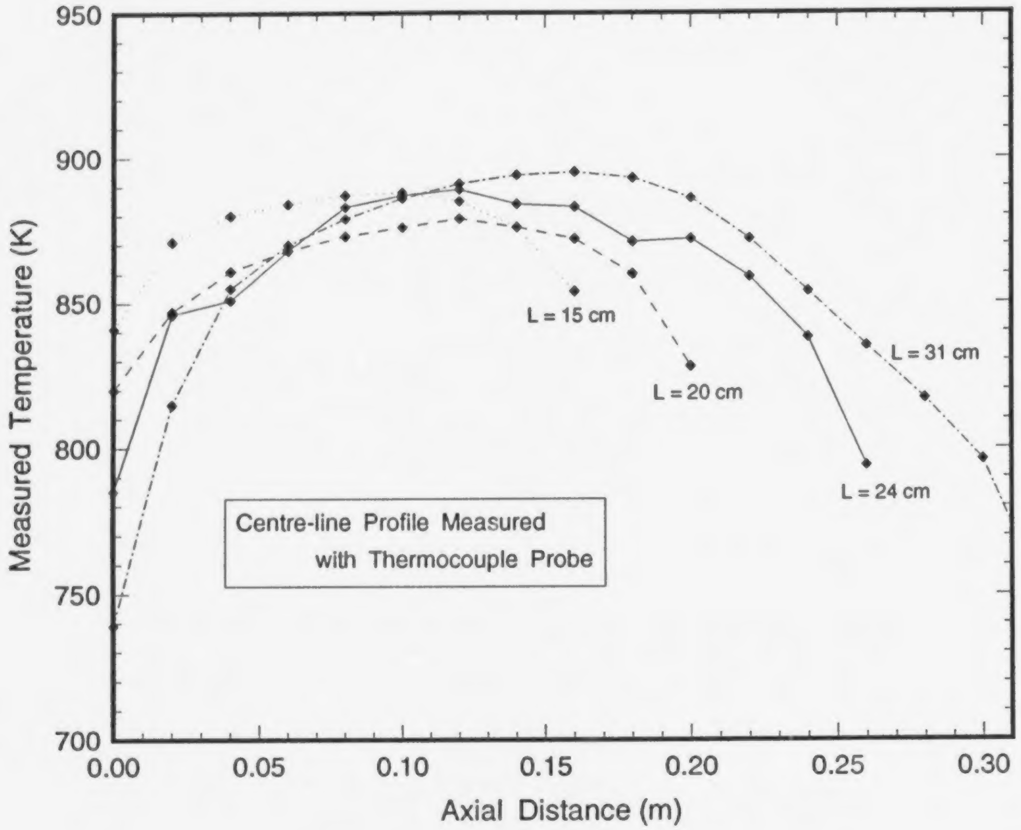

Experiment numbers: cat3 (3d), cat4 (4a), cat5 (5f), cat6 (6a)

Figure 2-4. Measured axial temperature profiles for catalytic combustion at different reactor lengths.

3

DEVELOPMENT OF THE MATHEMATICAL MODEL

A two dimensional mathematical model for the single channel monolith reactor was developed to analyse the experimental data. It can incorporate the effects of internal and external radiation, conduction in the channel and thermocouple probe wall, fully developed or developing gas flow as well as homogeneous and catalytic wall reaction. The model consists of a series of non-linear partial differential equations which were solved using the Galerkin finite element method. This model is an extension of a model that has been described in detail in an earlier work [40]. In this chapter a summary of the model is given and a description of the modifications made for this particular study.

3.1 The Governing Equations

A two-dimensional axisymmetric model was developed to simulate the reactor system outlined previously in Chapter 2. Even though a 2-D model is more complex than a 1-D model, it offers many advantages. The presence of catalytic reaction at the channel wall and a parabolic velocity profile makes the assumption of a constant radial concentration and temperature profile, inherent in a 1-D model, unrealistic. A 1-D model also requires correlations for the mass and heat transfer coefficients at the wall. Good correlations do not exist for reaction conditions, especially when the flow is thermally non-developed [40].

Coupled non-linear mole and energy balance equations are required to model the reactor system. The unsteady-state mole balance (advection-diffusion) equation may be written in terms of the mole fraction of PCB, (see for example [41]) :

$$\nabla \cdot (D \rho \nabla Y_{pcb}) - \rho (V \cdot \nabla Y_{pcb}) - R_H = \frac{\partial(\rho Y_{pcb})}{\partial t} \tag{3-1}$$

Equation (3-1) can then be expressed in terms of cylindrical coordinates

$$\frac{1}{r}\frac{\partial}{\partial r}\left[r D \rho \frac{\partial Y_{pcb}}{\partial r} \right] + \frac{\partial}{\partial z}\left[D \rho \frac{\partial Y_{pcb}}{\partial z} \right] - \rho V_z \frac{\partial Y_{pcb}}{\partial z} - R_H = \frac{\partial(\rho Y_{pcb})}{\partial t} \tag{3-2}$$

and is subject to the following boundary conditions:

$$Y_{pcb} = Y_{pcb_o} \qquad @z = 0 \quad all\ r \neq R \tag{3-3}$$

$$- D\rho \frac{\partial Y_{pcb}}{\partial r} = R_W \qquad @r = R \quad all\ z \tag{3-4}$$

$$\frac{\partial Y_{pcb}}{\partial z} = 0 \qquad @z = L \quad all\ r \neq R \tag{3-5}$$

$$\frac{\partial Y_{pcb}}{\partial r} = 0 \qquad @r = 0 \quad all\ z \tag{3-6}$$

where Equation (3-6) is the boundary condition for an empty tube.

The unsteady-state energy balance equation can be expressed as, (see for example [41]) :

$$\frac{1}{\rho\ Cp} \nabla \cdot (k_f \nabla T) - V \cdot \nabla T - \frac{\Delta H_R}{\rho\ Cp} R_H = \frac{\partial T}{\partial t} \tag{3-7}$$

Both the ∂t terms in Equations (3-1) and (3-7) are equal to zero for steady-state analysis. Subsequently, it will be shown in Section 3.7, that even for transient analysis these terms can also be assumed equal to zero.

Equation (3-7) can similarly be written in cylindrical coordinates and the following boundary conditions used:

$$T = T_o \qquad @z = 0 \quad all\ r \neq R \tag{3-8}$$

$$\frac{\partial T}{\partial z} = 0 \qquad @z = L \quad all\ r \neq R \tag{3-9}$$

$$\frac{\partial T}{\partial r} = 0 \qquad @r = 0 \quad all\ z \tag{3-10}$$

$$k_f \frac{\partial T}{\partial r} = Q_{gen} + Q_{axC} + Q_{eR} + Q_{iR} \qquad @r = R \quad all\ z \tag{3-11}$$

where Equation (3-10) is the boundary condition for an empty tube.

Q_{gen} is the heat generated (W m^{-2}) by the catalytic reaction at the channel wall (if present) and is given by:

$$Q_{gen} = (-\Delta H_R) R_W \tag{3-12}$$

Q_{axC} is the heat transfer (W m^{-2}) due to axial conduction in the channel wall. Assuming the wall temperature across the wall thickness δ_w is equal to the inside wall temperature T_{Wi} then by considering a control volume:

$$Q_{axC} = k_w \delta_w \frac{\partial^2 T_{Wi}}{\partial z^2} \tag{3-13}$$

Q_{eR} is the heat flux (W m^{-2}) due to external radiation between the furnace and the outside surface of the channel wall, see Figure 3-1. Considering the furnace as a black body with a large enclosing area, the radiation heat transfer $\hat{Q}_{eR}$ in W can be first expressed as:

$$\hat{Q}_{eR} = A_e \epsilon_{we} \sigma (T_F^4 - T_{We}^4) \tag{3-14}$$

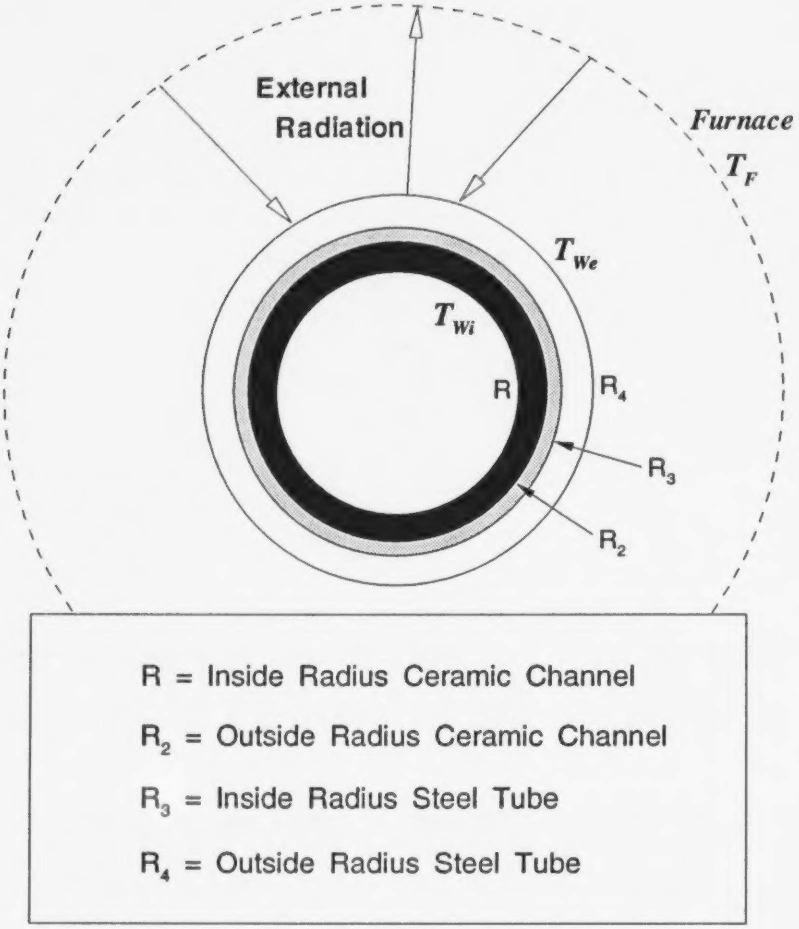
External Radiation
Furnace
T_F
T_{We}
T_{Wi}
R
R_4
R_3
R_2
R = Inside Radius Ceramic Channel
R_2 = Outside Radius Ceramic Channel
R_3 = Inside Radius Steel Tube
R_4 = Outside Radius Steel Tube

Figure 3-1. External radiation exchange with the furnace.

or in the form of a radiation heat transfer coefficient

$$\hat{Q}_{eR} = A_e \epsilon_{we} \sigma (T_F + T_{We})(T_F^2 + T_{We}^2)(T_F - T_{We}) \tag{3-15}$$

where T_F and T_{We} are the furnace wall temperature and the temperature of the external channel wall surface respectively, and A_e is the area of the external channel wall surface. The net heat transfer by external radiation $\hat{Q}_{eR}$ will be equal to the heat transfer due to radial conduction across the composite channel wall $\hat{Q}_{rC}$ ie.

$$\hat{Q}_{eR} = \hat{Q}_{rC} = \frac{(T_{We} - T_{Wi})}{\left[\left(\dfrac{\ln\dfrac{R_4}{R_3}}{2\pi k_{ss} L}\right) + \left(\dfrac{\ln\dfrac{R_3}{R_2}}{2\pi k_{air} L}\right) + \left(\dfrac{\ln\dfrac{R_2}{R}}{2\pi k_c L}\right)\right]} \tag{3-16}$$

where k_x is the thermal conductivity of the stainless steel, air and ceramic materials of the channel wall and R_x their respective inside and outside radii. From Equation (3-15) and (3-16) the external wall temperature T_{We} can be eliminated and Q_{eR} detemined as a flux based on the inside surface area, which can then be implemented as a boundary condition in Equation (3-11), thus:

$$Q_{eR} = \frac{\hat{Q}_{eR}}{2\pi R L} = (T_F - T_{Wi})\left[\frac{1}{\dfrac{R_4}{R}\epsilon_{we}\sigma(T_F + T_{We})(T_F^2 + T_{We}^2)} + \lambda_w\right]^{-1} \tag{3-17}$$

where λ_w is the radial wall conduction resistance across the composite channel wall given by the following:

$$\lambda_w = R\left[\left(\frac{\ln\dfrac{R_4}{R_3}}{k_{ss}}\right) + \left(\frac{\ln\dfrac{R_3}{R_2}}{k_{air}}\right) + \left(\frac{\ln\dfrac{R_2}{R}}{k_c}\right)\right] \tag{3-18}$$

Note this analysis ignores the effect of radiation transfer across the air gap which would reduce the effective heat transfer resistance of the channel wall, see Section 4A.6.

Q_{iR} the final term in Equation (3-11), is the heat transfer (W m^{-2}) due to internal radiation in the channel. The gas phase was assumed to be essentially transparent to radiation since the amount of CO_2 and H_2O present was minimal.

In this study the Reynolds number for the reactor was below 300, corresponding to laminar flow. Assuming ideal gas behaviour, fully developed flow in an empty tube and negligible reactor pressure drop, the axial gas velocity at any position will be given by the following equation :

$$V_Z(z,r) = 2\langle V_{Z_o}\rangle \left[1 - \left[\frac{r}{R}\right]^2\right] \frac{T(z,r)}{T_o} \qquad \textbf{(3-19)}$$

where T_o is the inlet temperature and $\langle V_{Zo}\rangle$ is the average inlet velocity.

3.2 Physical Properties

The physical properties of the reactor system used in the model are detailed in Table 3-1. The channel wall density, heat capacity and axial thermal conductivity were calculated using a volume weighted average since the channel wall consists of a ceramic, air gap and stainless steel composite, details are given in Appendix A.1. The calculation of the radial conduction resistance λ_w is also given in Appendix A.1, it was found that the 0.6 mm air gap constituted the dominant conduction resistance in the composite channel wall. A high value for the emissivity of the inside ceramic and external stainless steel wall was used, since inspection of the experimental apparatus after several experimental runs revealed that the walls were fairly black due to oxidation.

The heat capacity of the gas phase was calculated using a 4th-order polynomial in temperature for each component, taking constants from [42]. The heat of reaction for the combustion of PCB is also defined in terms of a fourth order polynomial in temperature using the standard heat of reaction and heat capacity data, Appendix A.2 explains this in more detail. The thermal conductivity of the gas was treated as a linear function of temperature using values for air and nitrogen given by [43].

Table 3-1. Physical properties of the reactor system.

CHANNEL WALL (steel/air/ceramic composite)	
δ_w total wall thickness	5.25×10^{-3} m
ρ_w wall density	5049 kg m^{-3}
Cp_w wall heat capacity	850 J kg^{-1} K^{-1}
k_w axial wall thermal conductivity	11.92 W m^{-1} K^{-1}
λ_w radial wall conduction resistance	8.41×10^{-3} K m^2 W^{-1}
ϵ_{wi} emissivity of inside wall	0.8
ϵ_{wo} emissivity of outside wall	0.7
THERMOCOUPLE PROBE	
δ_p probe wall thickness	0.4×10^{-3} m
ρ_p probe wall density	7800 kg m^{-3}
Cp_p probe wall heat capacity	502 J kg^{-1} K^{-1}
k_p axial probe thermal conductivity	22 W m^{-1} K^{-1}
ϵ_p emissivity of the probe wall	0.8

The molecular diffusion coefficient for PCB in air was determined using the Fuller et al. empirical relation [44], which gives reliable predictions at moderate to high temperatures with an accuracy of 5-10 percent:

$$D = D_k \frac{T^{1.75}}{P} \tag{3-20}$$

where P has units of Pa, T is in K and $D_k = 2.5322 \times 10^{-5}$ Pa m^2 K$^{-1.75}$ s^{-1} to give D in m^2 s^{-1} (see Appendix A.3). Values for the diffusion coefficient of PCB obtained using Equation (3-20) compare well with experimental values found in the literature for biphenyl and chlorobenzene, see Table 3-2. The calculated diffusion coefficient for PCB is lower than chlorobenzene and biphenyl at corresponding conditions of temperature and pressure. This is expected since a typical PCB molecule has a higher molecular weight and volume.

Table 3-2. Molecular diffusion coefficient for PCB.

Conditions	Literature value of D (m^2 s^{-1}) for Chlorobenzene	Literature value of D (m^2 s^{-1}) for Biphenyl	Calculated value of D (m^2 s^{-1}) for PCB using Equation (3-20)
air[*] 1 atm 303 K	7.50×10^{-6}	-	5.50×10^{-6}
air[†] 1 atm 332 K	9×10^{-6}	-	6×10^{-6}
air[*] 1 atm 273 K	-	6.10×10^{-6}	4.58×10^{-6}
air[†] 1 atm 491 K	-	16.0×10^{-6}	13.0×10^{-6}

[*] Data taken from Perry et al. [43]

[†] Data taken from Gilliland et al. [45]

3.3 PCB Combustion Kinetics

The rate of the homogeneous and catalytic reaction, R_H and R_W respectively, must be expressed in terms of a kinetic rate expression. Assuming that the average number of chlorine atoms per molecule of Aroclor 1242 is 3.1 with an average molecular weight of 261, the combustion of this PCB can be represented by the following reaction [46]:

$$C_{12}H_{6.9}Cl_{3.1} + 12.95\ O_2 \Rightarrow 12\ CO_2 + 1.9\ H_2O + 3.1\ HCl$$

This reaction will occur homogeneously in the bulk phase and also heterogeneously at the channel wall when the channel is coated with the chromia catalyst. In reality these are two connected processes *ie* the reaction at the catalyst surface produces radicals which may influence the homogeneous reaction in the bulk phase and *vice versa*. For simplicity, it is often assumed that they are two separate and distinct sets of reactions and the homogeneous and heterogeneous reaction are modelled separately [22]. This approach is adopted in this study.

It is difficult to use a reaction mechanism strategy for the modelling of the kinetics, where the overall reaction is broken down into steps of elementary reactions. Often the intermediate reaction steps are not known or poorly understood and the resulting model is complicated and unsuitable for most design purposes. An alternative is to use a global reaction expression, but it be must be remembered that the kinetics may not be applicable outside the range of conditions in which the original data were obtained. The thermal oxidation of chlorinated organics has previously been successfully modelled using pseudo first order reaction kinetics [47,48]. The oxygen in this experimental study was also in large excess and so essentially constant, hence the following homogeneous reaction kinetics were assumed:

$$R_H = A_H \exp\left[-\frac{E_H}{R_g T}\right] C_{pcb} \tag{3-21}$$

where C_{pcb} is the concentration of PCB in the gas phase and A_H, E_H are the Arrhenius pre-exponential factor and activation energy for the homogeneous reaction respectively. Using the ideal gas law, the concentration of PCB can then be converted to mole fraction :

$$C_{pcb} = \rho Y_{pcb} = \frac{Y_{pcb} P}{R_g T} \tag{3-22}$$

where P is the operation pressure of the reactor.

Manning [49] studied the catalytic combustion of several chlorinated organics using a chromia catalyst in a fluid bed reactor and found the reaction to be first order with respect to the chlorocarbon species. Greene and Subbanna [50] also successfully modelled the combustion of Aroclor 1254 PCB in monolithic reactor using a first order type model. Hence, the heterogeneous kinetics for the catalytic combustion of PCB on the chromia coated channel wall were taken to be :

$$R_W = A_W \exp\left[-\frac{E_W}{R_g T}\right] C_{pcb} \tag{3-23}$$

where C_{pcb} is the concentration of PCB adjacent to the wall. Even if the catalytic reaction can be modelled by a Langmuir-Hinshelwood type mechanism, at high temperatures the overall rate will still tend to first order since the equilibrium constant for exothermic adsorption $\ll 1$.

3.4 Solution Methodology

It was shown in the previous sections that a mathematical description of the reactor gives two coupled partial differential equations (PDE) with complex boundary conditions. A finite element solution was employed for the solution since it offers strong advantages over other possible strategies:

i) By using a weak variational form of the PDE the flux boundary conditions can be incorporated in a mathematically rigorous way.

ii) It is easy to use a non-uniform (unstructured) mesh with variable element size. This can be important for as it allows the use of a fine mesh near the channel wall where temperature and concentration gradients maybe steep but a coarser mesh elsewhere. This can reduce the size of the problem to be solved at no cost in accuracy.

The Galerkin finite element method was used for solution of the PDE. This involves first discretising the solution domain Ω into a number of finite element domains Ω^e. Then by using an appropriate interpolation function ψ the unknowns Y_{pcb} and T can be approximated for each finite element:

$$Y_{pcb}(z,r) = \sum_{i=1}^{m} \psi_i Y_{pcb\,i} \qquad \textbf{(3-24)}$$

$$T(z,r) = \sum_{i=1}^{m} \psi_i T_i \qquad \textbf{(3-25)}$$

where m is the number of nodes associated with each finite element. In this study $m = 6$ as P2 triangular elements were used which have 6 nodes, see Figure 3-2(a). The interpolation functions ψ_i, of the triangular element are quadratic Langrangian polynomials [51].

As Equations (3-24) and (3-25) are only approximations to the unknowns in the two PDE, the solutions obtained are not exact and hence, result in residual errors. The aim is to minimise the residual error over each Ω^e. This is done by setting the integral of the weighted residual error to zero. For the Galerkin finite element method the weight functions are chosen to be the interpolation functions ψ. Hence, if this procedure is applied to the mole and energy balance equations described in Section 3.1, with the use

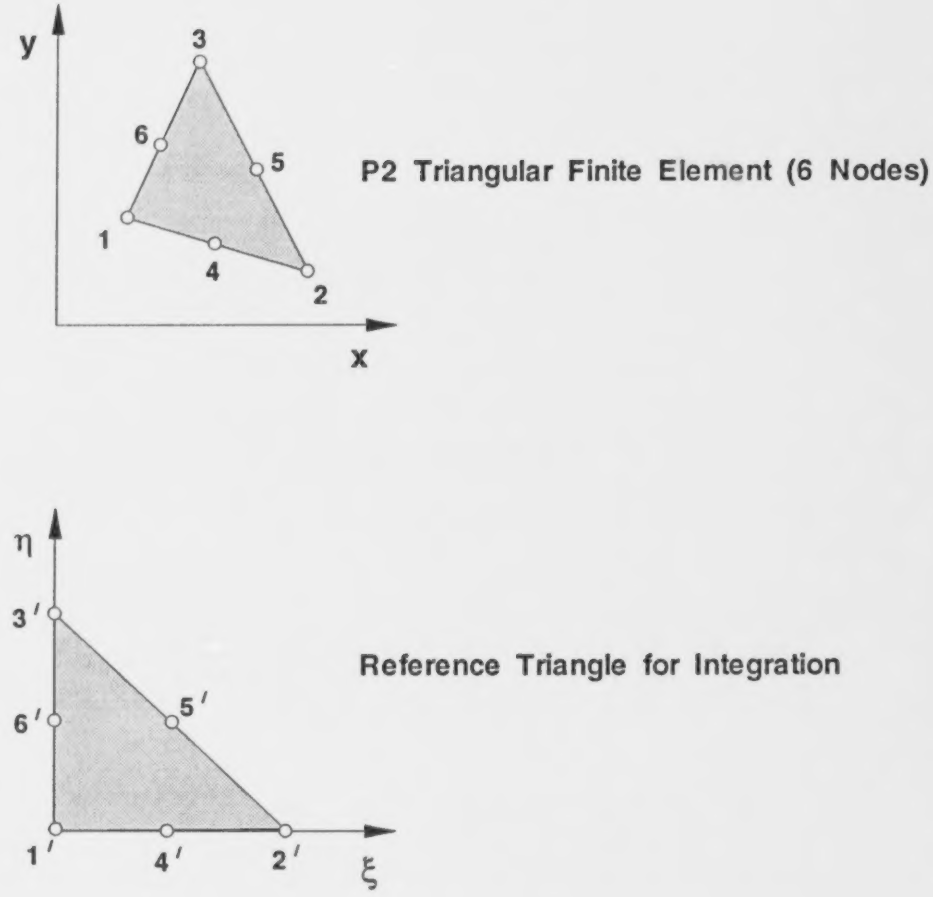

P2 Triangular Finite Element (6 Nodes)

Reference Triangle for Integration

y
x
1
2
3
4
5
6
η
ξ
1′
2′
3′
4′
5′
6′

Figure 3-2(a). P2 triangular finite element and reference triangle.

of Green's theorem (multi-dimensional integration by parts), the following formulations are obtained:

$$\begin{aligned}\int_{\Omega^e} \nabla\psi D \nabla Y_{pcb}\, d\Omega^e &+ \int_{\Omega^e} \psi A_H \exp\left[-\frac{E_H}{R_g T}\right] Y_{pcb}\, d\Omega^e \\ &+ \int_{\Omega^e} \psi\, V\cdot\nabla Y_{pcb}\, d\Omega^e - \oint_{\Gamma^e} \psi D\,[n]\cdot\nabla Y_{pcb}\, d\Gamma^e = 0\end{aligned} \tag{3-26}$$

$$\begin{aligned}\int_{\Omega^e} \left[\frac{R_g k_f}{P\,Cp}\right] T\nabla\psi\,\nabla T\, d\Omega^e &+ \int_{\Omega^e} \psi\, V\cdot\nabla T\, d\Omega^e \\ &+ \int_{\Omega^e} \psi \left[\frac{\Delta H_R A_H}{Cp}\right] Y_{pcb} \exp\left[-\frac{E_H}{R_g T}\right] d\Omega^e \\ &- \oint_{\Gamma^e} \psi \left[\frac{R_g\, T}{P\,Cp}\right] k_f\,[n]\cdot\nabla T\, d\Gamma^e = 0\end{aligned} \tag{3-27}$$

where Γ^e is the boundary and $\oint$ the contour integral which only requires evaluation when an element edge lies on a boundary of the mesh.

For the mole balance equation the flux at the channel wall equals the rate of catalytic reaction as stated in Equation (3-4). Therefore, at the wall, the countour integral in Equation (3-26) becomes:

$$-\oint_{\Gamma^e} \psi D \frac{\partial Y_{pcb}}{\partial r}\, d\Gamma^e = \oint_{\Gamma^e} \psi A_W \exp\left\{-\frac{E_W}{R_g\, T}\right\} Y_{pcb}\, d\Gamma^e \tag{3-28}$$

For the rest of the boundary this integral has a value of zero, since the flux is zero at the centre-line and exit, while Dirichlet conditions are imposed at the entrance, see Equations (3-3) to (3-6).

For the energy balance equation, the contour integral at the channel wall in Equation (3-27) can be evaluated by substitution of Equation (3-11). After simplification this yields:

$$
\begin{aligned}
-\oint_{\Gamma^e} \psi \left[\frac{R_g\, T}{P\, Cp} \right] k_f \frac{\partial T}{\partial r}\, d\Gamma^e \\
= \oint_{\Gamma^e} \psi \Big\{ \; \frac{\Delta H_R}{Cp} Y_{pcb}\, A_W \exp\left(- \frac{E_W}{R_g T} \right) \; - \; \frac{k_w\, \delta_w\, R_g\, T}{P\, Cp} \frac{\partial^2 T_{Wi}}{\partial z^2} \qquad (3\text{-}29) \\
- \; \frac{\epsilon_{we}\, \sigma\, R_g\, T}{P\, Cp} \left[\frac{R + \delta_w}{R} \right] (T_F^4 - T_{We}^4) \; - \; \frac{R_g T}{P\, Cp} Q_{iR} \; \Big\} d\Gamma^e
\end{aligned}
$$

while it has a value of zero on the centreline, entrance and exit boundaries, see Equations (3-8) to (3-11).

The second derivative of the wall temperature T_{Wi} was determined by curve-fitting a tenth-order polynomial to the wall temperature profile using standard least-squares analysis, and subsequently computing the second derivative analytically. An alternative, method for including the effect of axial wall conduction in the reactor model was developed at a later stage in this study, and is explained in Section 3.7.

Initially the external wall temperature T_{We} in Equation (3-17) is unknown. Hence the following iterative scheme is used to determine Q_{eR} since the radial conduction resistance λ_w across the composite (steel/air/ceramic) channel wall is known.

i) Assume $T_{We} = T_{Wi} = T_{@\, r = R}$

ii) Calculate the net rate of external radiation flux Q_{eR} using Equation (3-17)

iii) Compute T_{We} using the radial conduction equation:

$$T_{We} = T_{Wi} + \lambda_w Q_{eR} \qquad (3\text{-}30)$$

iv) Compare new T_{We} with initial guess. Repeat steps i) to iv) until convergence, which usually required 6-7 iterations.

The heat transfer due to internal radiation Q_{iR}, is evaluated by dividing the inside surface into a number of discrete isothermal surfaces of length equal to one finite element. Assuming that these surfaces can be treated as grey diffuse reflectors (directional and wavelength independent emissivity), the net flux to any surface *j* is given by:

$$Q_{r_j} = (J_j - E_{b_j}) \left[\frac{\epsilon_j}{1 - \epsilon_j} \right] \tag{3-31}$$

where E_b is the blackbody radiation,

$$E_b = \sigma \, T^4_{wi_j} \tag{3-32}$$

J is the radiosity (accounts for all of the radiant energy leaving a surface) and ϵ is emissivity set equal to ϵ_{wi}. The radiosity of each surface J_j will depend on the radiation exchange between it and all other elements, as well as the exit and entrance. Since at the exit and entrance, the surface is radiating to a relatively large area, they are assumed to be black bodies. Thus, for N_i interior segments, plus the entrance and exit which are denoted with subscripts 1 and 2 respectively, the equation which determines J_j is:

$$(E_{b_j} - J_j) \left[\frac{\epsilon_j}{1-\epsilon_j} \right] = \left[\sum_{k=1}^{N_i} F_{jk}(J_j - J_k) \right] + K_{j1}(J_j - E_{b1}) + K_{j2}(J_j - E_{b2}) \tag{3-33}$$

and E_{b1} and E_{b2} are defined by the entrance and exit temperatures for radiation,

$$E_{b1} = \sigma \, T^4_{OR} \qquad and \qquad E_{b2} = \sigma \, T^4_{LR} \tag{3-34}$$

The constant F_{jk} is the view factor, *ie* the fraction of radiation leaving surface *j* which strikes surface *k*. K_{j1} and K_{j2} are the view factors for the reactor ends. For any two arbitrary surface elements *j* and *k* of lengths $2w_j$ and $2w_k$ respectively, inside a channel of radius R, with a distance of s between the mid-point of the elements, the F_{jk} will be:

$$F_{jk} = \phi_k - \frac{1}{8}(2\eta - \beta - 1)\sqrt{4 + (\xi - \phi_j - \phi_k)^2}$$

$$+ \frac{1}{8}(2\eta - \beta + 1)\sqrt{4 + (\xi + \phi_j - \phi_k)^2} + \frac{1}{8}(2\eta + \beta - 1)\sqrt{4 + (\xi - \phi_j + \phi_k)^2} \qquad (3\text{-}35)$$

$$- \frac{1}{8}(2\eta + \beta + 1)\sqrt{4 + (\xi + \phi_j + \phi_k)^2}$$

where the dimensionless parameters are defined as $\xi = s/R$, $\phi_j = w_j/R$, $\phi_k = w_k/R$, $\eta = s/(2wj)$ and $\beta = w_k/w_j$. Now consider a segment of length $2w_j$ with a mid-point a distance z from the entrance and $(L - z)$ from the exit, the entrance and exit view factors are then given by:

$$K_{j1} = \frac{(\gamma_1 + 1)}{8}\sqrt{4 + (\theta_1 + \phi_j)^2} - \frac{(\gamma_1 - 1)}{8}\sqrt{4 + (\theta_1 - \phi_j)^2} - \frac{\theta_1}{2} \qquad (3\text{-}36)$$

$$K_{j2} = \frac{(\gamma_2 + 1)}{8}\sqrt{4 + (\theta_2 + \phi_j)^2} - \frac{(\gamma_2 - 1)}{8}\sqrt{4 + (\theta_2 - \phi_j)^2} - \frac{\theta_2}{2} \qquad (3\text{-}37)$$

where $\Theta_1 = z/R$, $\Theta_2 = (L-z)/R$, $\gamma_1 = z/w_j$ and $\gamma_2 = (L-z)/w_j$. Appendix A.4 gives a detailed derivation of Equations (3-35) to (3-37).

The integrals in Equations (3-26) and (3-27) were evaluated using Gaussian (Hammer) integration in a reference element domain (ξ, η):

$$\int_0^1 \int_0^{1-\xi} g(\xi, \eta)\, d\xi\, d\eta \cong \sum_{k=1}^{n_g} w_k\, g(\xi_k, \eta_k) \qquad (3\text{-}38)$$

where $g(\xi_k, \eta_k)$ is the value of the function g at the Gaussian integration point k, w_k is the Gaussian weighting coefficient for point k and n_g is the number of integration points. In this study a six-point Gaussian quadrature method was used ($n_g = 6$), the reference triangle is illustrated in Figure 3-2(a). Similarly, the contour integrals were evaluated using four-point Guassian integration.

Upon substitution of Equations (3-24) and (3-25) into (3-26) and (3-27), six simultaneous equations for the concentration problem and six simultaneous equations for the temperature problem are obtained for each element in the mesh. Finally, the contributions of all the element equations are assembled into two global matrix equations to obtain a solution over the entire domain Ω:

$$[\![M_Y]\!]\,[\,Y_{pcb}\,] \;=\; [\,F_Y\,] \tag{3-39}$$

$$[\![M_T]\!]\,[\,T\,] \;=\; [\,F_T\,] \tag{3-40}$$

where $[\![M_Y]\!]$ and $[\![M_T]\!]$ are the global concentration and temperature matrices and $[F_Y]$ and $[F_T]$ are the global concentration and temperature vectors respectively. The global equations were then solved using a Newton-Raphson technique, in which the Jacobian matrix was built and inverted by LU factorization. This operation is expensive in computation time and so it is desirable to minimise the number of times the Jacobian is factorised. The option existed in the model to factorise the Jacobian and then use it in a number of subsequent iterations before factorising the Jacobian again. This is a quasi-Newton type method which may save computation time. However, for this problem, optimal convergence was obtained when the Jacobian matrix was factorised every iteration step. The algorithm that gave the best convergence behaviour is summarised below :

i) Build and factor the global Jacobian matrix $[\![J_Y]\!]$ for the mole balance equation, using an initial solution or reference values of temperature and concentration.

ii) Implement one Newton iteration to the concentration problem and apply $[\Delta Y_{pcb}]$ the calculated correction :

$$\left[\Delta Y_{pcb}^{n+1}\right] \;=\; -[\,F_Y\,][\![J_Y]\!]^{-1} \tag{3-41}$$

$$\left[Y_{pcb}^{n+1} \right] = \left[Y_{pcb}^{n} \right] + \left[\Delta Y_{pcb}^{n+1} \right] \qquad \textbf{(3-42)}$$

iii) Build and factor the global Jacobian matrix $[\![J_T]\!]$ for the energy balance equation using the latest values of temperature and concentration.

iv) Implement one Newton iteration to the temperature problem and apply [ΔT] the calculated correction :

$$\left[\Delta T^{n+1} \right] = -\left[F_T \right][\![J_T]\!]^{-1} \qquad \textbf{(3-43)}$$

$$\left[T^{n+1} \right] = \left[T^{n} \right] + \left[\Delta T^{n+1} \right] \qquad \textbf{(3-44)}$$

v) Build and factor the global Jacobian matrix for the mole balance equation using the latest values of temperature and mole fraction.

vi) Repeat steps ii) to v) until the difference in subsequent iterations for the solution [Y_{pcb}] and [T] is less than a preset tolerance.

Two finite element meshes used in this investigation are shown in Figure 3-2(b), the first represents a uniform mesh with 1984 elements, the second a non-uniform mesh with 924 elements, both meshes are for a 25 cm long empty channel. The non-uniform mesh is finer in the region close to the channel wall so that sharp temperature and concentration gradients can be captured. The uniform mesh contains elements that are equivalent in size to the elements adjacent to the channel wall in the non-uniform mesh.

3.5 Model Development due to the Thermocouple Probe

During the experimental work the axial temperature profile along the reactor was measured using a thermocouple traversed inside a thin metal sleeve that was fixed along the centre-line of the reactor. In developing the reactor model it must be considered that the thermocouple probe will cause two effects; the gas velocity profile will be altered

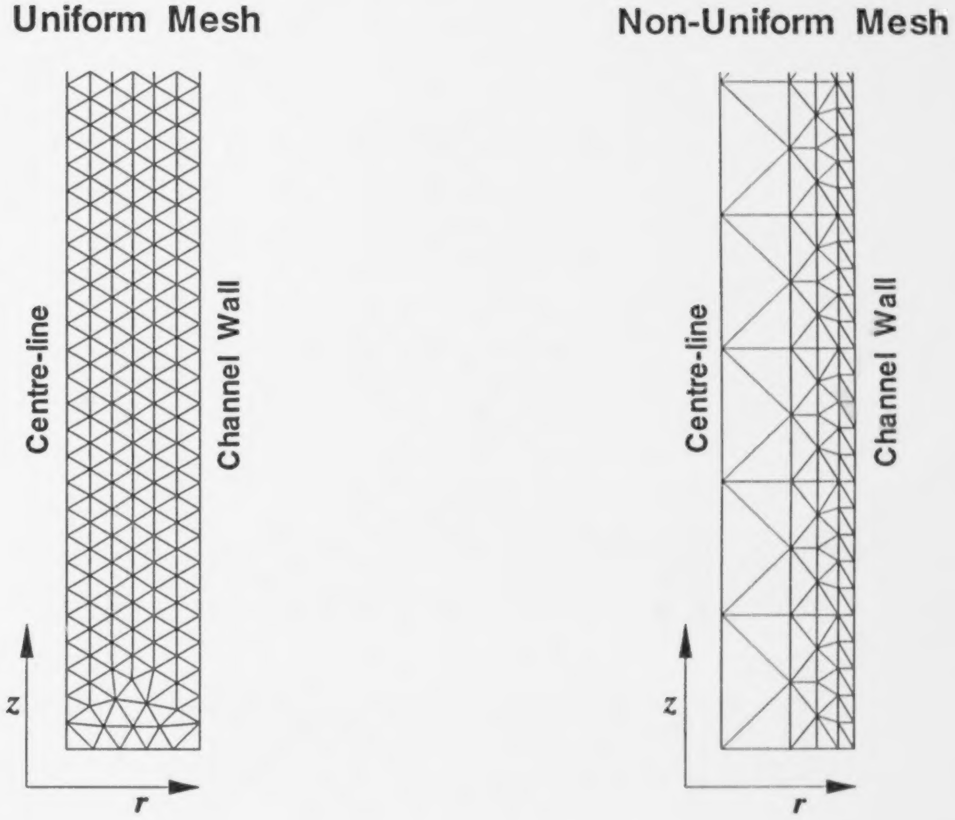
Uniform Mesh
Centre-line
Channel Wall
z
r
Non-Uniform Mesh
Centre-line
Channel Wall
z
r

Figure 3-2(b). Examples of the finite element mesh.

from that of an empty tube due to zero slip on the probe wall; the centre-line temperature will be altered due to radiation exchange with the channel wall and the ends.

To account for the effect of the probe on the velocity profile, instead of Equation (3-19), the following equation for fully developed laminar flow in an annulus was used [52]:

$$V_{z_o}(r) = 2 \langle V_{z_o} \rangle \left[\frac{R^2 - r^2 - 2 r_m^2 \ln \left[\frac{R}{r} \right]}{R^2 + R_p^2 - 2 r_m^2} \right] \tag{3-45}$$

where V_{Zo} is the radial profile of the axial velocity at the reactor inlet and r_m is the position of maximum velocity (zero shear), which is given by the equation:

$$r_m^2 = \frac{R^2 - R_p^2}{2 \ln \left[\frac{R}{R_p} \right]} \tag{3-46}$$

As before the axial velocity is then adjusted for expansion with temperature by assuming ideal gas behaviour and negligible pressure drop over the reactor length:

$$V_Z(z,r) = V_{z_o}(r) \frac{T(z,r)}{T_o} \tag{3-47}$$

The reactor model was also modified to incorporate radiation exchange between the channel and probe wall and radiation from the walls out the two reactor ends, see Figure 3-3. Instead of the empty-tube boundary condition at the centre-line, Equation (3-10), the following boundary condition is now used at the probe wall:

$$k_f \frac{\partial T}{\partial r} = Q_{axC} + Q_{iR} \qquad @ r = R_p \quad all\ z \tag{3-48}$$

This takes account of heat transfer by radiation from the probe as well as axial heat conduction along the probe wall. As previously described in Section 3.1 the wall surfaces

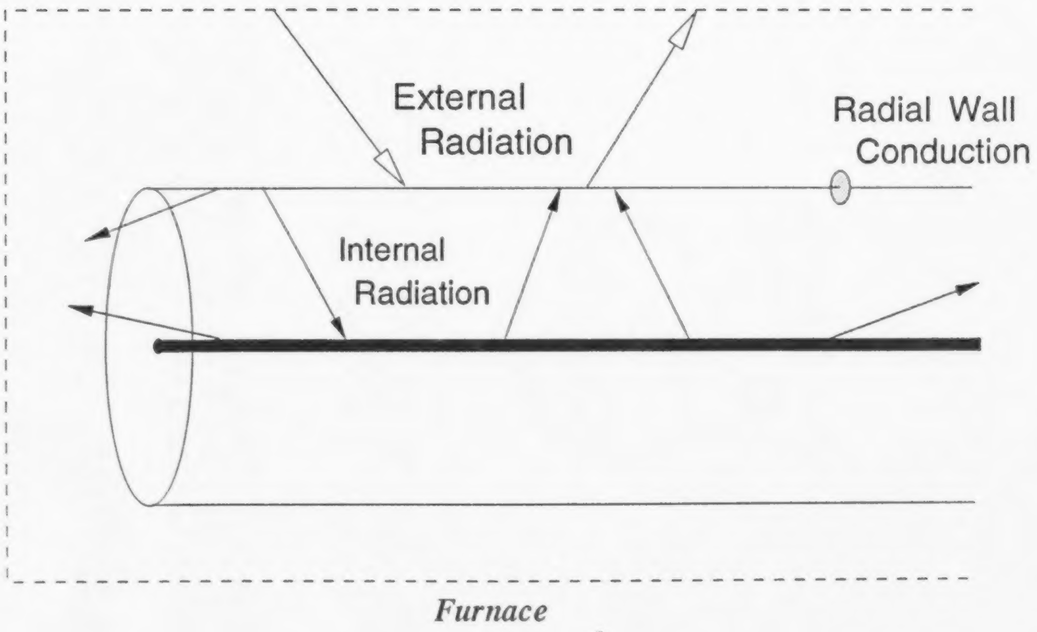
External
Radiation
Radial Wall
Conduction
Internal
Radiation
Furnace

Figure 3-3. Model development due to internal radiation to the probe.

were divided into a number of discrete isothermal elements and each element assumed to be grey diffuse reflectors. However in this case, the view factors F_{jk} now have to be calculated for an annular geometry. These were evaluated based on the work of Leuenberger *et al.*[53] who derived analytical expressions for the view factors of various cylindrical assemblies. Details of the view factor calculation are given in Appendix A.5.

3.6 Developing Velocity Profile in an Annulus

The experimental reactor had a stainless steel manifold installed at the entrance to provide even flow distribution. Smoke tests showed that this manifold produced a reasonably good plug flow profile at the inlet. The velocity profile would then theoretically develop to full laminar parabolic flow over a distance L_D (the developing length), this is illustrated in Figure 3-4(a).

At the experimental conditions used in this study the Reynolds number based on an annulus was approximately 270.

$$Re = \frac{\langle V_z \rangle \rho \, d_e}{\mu} \qquad \textit{where} \quad d_e = 2(R - R_p) \tag{3-49}$$

At this value the developing length is a significant fraction of the overall channel length and so developing flow may be important. The reactor model was modified so that the gas velocity profile could be one of the following options:

i) Developing flow in an annulus (plug flow to full laminar parabolic).
ii) Fully developed laminar flow in an annulus, Equations (3-45) to (3-47).

In both cases the velocity profile is subject to changes in gas density.

The developing velocity profile was simulated by solving the set of Navier-Stokes equations using the POLY2D software package from Rheotec Inc. of Quebec, Canada. The program uses a penalty Galerkin finite element method with *Crouzeix-Raviart*

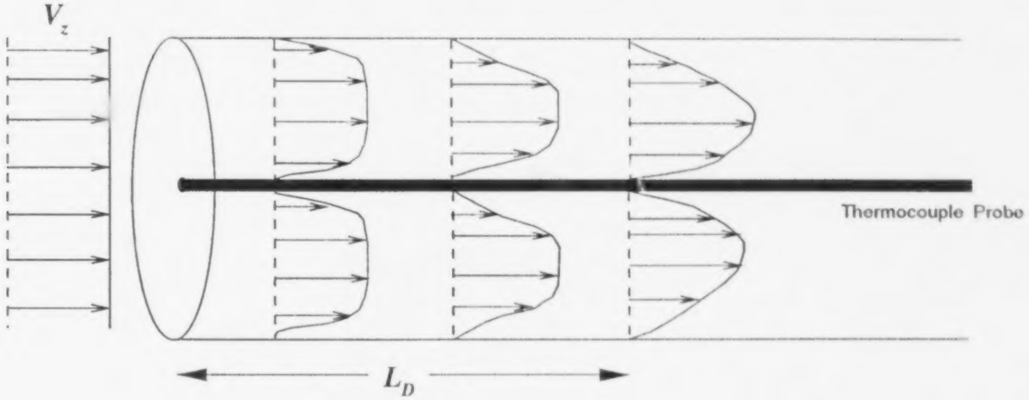
V_z
Thermocouple Probe
L_D

Figure 3-4(a). Developing laminar flow in the reactor annulus.

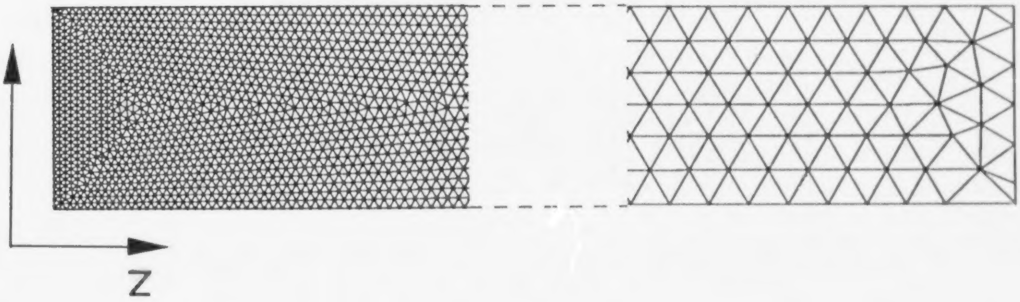

Figure 3-4(b). Finite element mesh for the Navier-Stokes solution.

elements [54]. The finite element mesh used contained approximately 6000 elements for a 25 cm length channel and is shown in Figure 3-4(b). The mesh is fine at the reactor entrance where the velocity profile is changing rapidly, but as the profile tends to fully developed the mesh becomes coarser. In this way unnecessary computation time is avoided. The Navier-Stokes equations were solved for incompressible flow at the inlet gas temperature T_o using the following boundary conditions:

$$V = \langle V_o \rangle \qquad @z = 0 \quad all\ r \neq R,\ R_p \tag{3-50}$$

$$V = 0 \qquad @r = R \quad all\ z \tag{3-51}$$

$$V = 0 \qquad @r = R_p \quad all\ z \tag{3-52}$$

$$V = 2\langle V_o \rangle \left[\frac{R^2 - r^2 - 2r_m^2 \ln\left[\frac{R}{r}\right]}{R^2 + R_p^2 - 2r_m^2} \right] \qquad @z = L \tag{3-53}$$

The last boundary condition given in Equation (3-53) represents fully developed flow at the outlet of the channel and is a result of specifying a constant arbitrary pressure and zero radial velocity at $z = L$. The velocity solution $V_{z,ro}$ is stored and then used by the reactor model, by interpolating the results onto the coarser reactor finite element mesh. This again saves computation time. The reactor model adjusts the simulated velocity profile for changes in gas temperature using the ideal gas law at constant pressure:

$$V_{z,r} = V_{z,r_o} \frac{T(z,r)}{T_o} \tag{3-54}$$

Solution of the Navier-Stokes equations gave a reactor pressure drop of about 5 Pa at the experimental conditions, so the assumption of negligible pressure drop is valid.

Summarising, the following solution algorithm is used to account for developing flow:

i) Solution of the Navier-Stokes equations for incompressible flow at the inlet gas temperature T_O.

ii) Reactor model uses this velocity solution.

- Interpolation onto the coarser finite element mesh for the reactor
- Adjustment of the velocity for expansion with temperature

Figure 3-5 shows a typical developing velocity profile generated using the algorithm, the radial profiles have been generated at 0.5 cm intervals along the length. At the experimental conditions, $Re \approx 270$, the developing length (to reach 99% of the downstream maximum velocity) was calculated to be $L_D = 7$ cm. For an empty tube of the same diameter and at equivalent conditions the developing length is considerably greater, $L_D = 16$ cm. The probe introduces an additional surface for drag and thus causes more rapid velocity development. As can be seen developing flow produces a small radial velocity component V_r as flow is pushed towards the channel core. The flow in the core is also more influenced by the boundary layer on the channel wall since the probe has a much smaller diameter compared to the inside channel.

Developing laminar flow in an annulus has been previously studied by Sparrow and Lin [55] and Heaton *et al.* [56], both authors developed an approximate analytical solution to the velocity profile assuming incompressible flow. The results of Sparrow and Lin [55] gave satisfactory agreement with experimental measurements with air. The simulated results obtained using the described algorithm compare well with their analytical method over a range of Reynolds numbers, see Table 3-3.

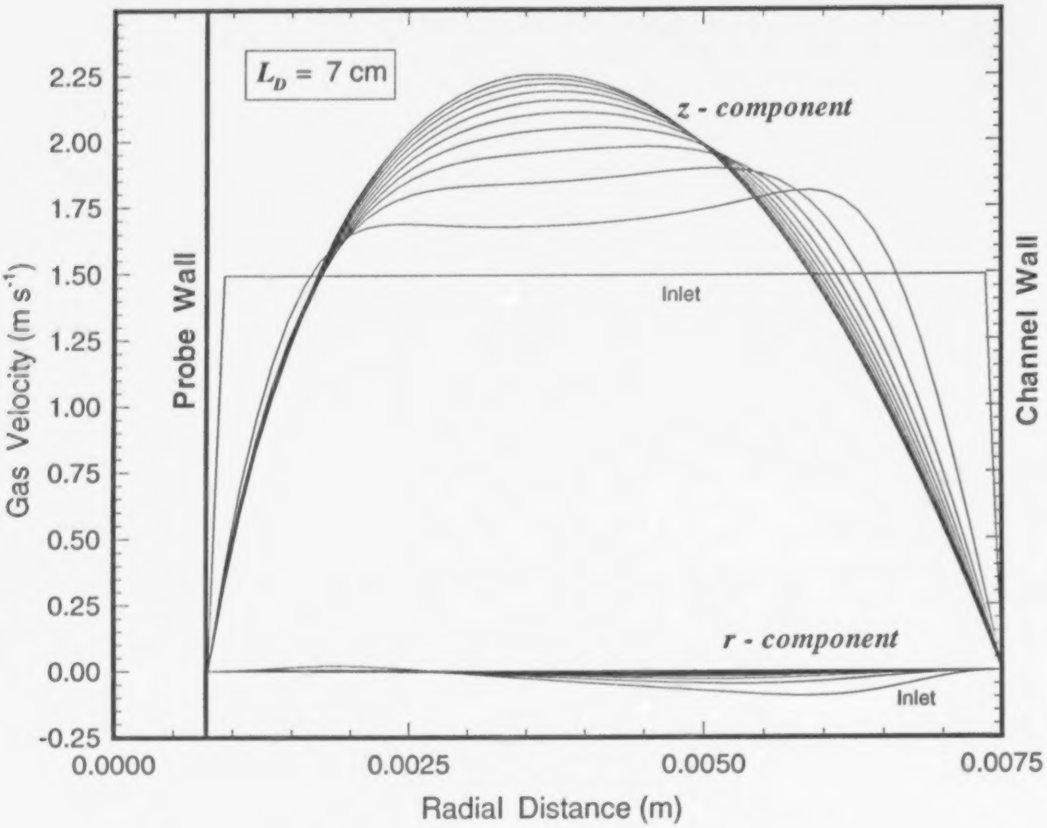

Conditions: pcb1 (5, 1a); Re = 271; $\langle V_{ZO} \rangle$ = 1.493 m s^{-1}; T_O = 746 K; profile spacing = 5 mm

Figure 3-5. Developing velocity profile in the reactor annulus.

Table 3-3. Developing flow lengths at different Reynolds numbers.

Reynolds No.	Simulated developing length* L_D (cm)	Literature developing length† L_D (cm)
89	1.8	2.2
133	2.7	3.3
177	3.6	4.4
265	5.3	6.2

* Length required to reach 99 % of the maximum outlet velocity

† Analytical method of Sparrow and Lin [55]

3.7 Convergence Behaviour and the Transient Algorithm

Testing of the previously described reactor model showed that it was generally stable and reliable but it was difficult to obtain a converged solution when the following conditions were imposed :

i) Internal radiation in the channel at an emissivity value, $\epsilon_{wi} > 0.5$: This is probably due to the non-linearity inherent in the 4th order radiation calculation.

ii) Axial wall conduction Q_{axC} : The method of curve-fitting a tenth-order polynomial to the wall temperature (see Section 3.4) introduced slight oscillations in the axial wall temperature profile which caused the solution method to become unstable.

iii) Catalytic reaction with an inlet PCB mole fraction, $Y_{pcb} > 5 \times 10^{-3}$: This is thought to be some numerical instability present in the solution methodology.

The reactor model was modified in order to obtain a converged solution for the above cases. A loading strategy was implemented that uses an initial converged solution as a starting point, and then by changing one of the model parameters in small increments a converged solution could be obtained at more stringent conditions. Best results were obtained by loading on the inlet velocity $\langle V_{Zo} \rangle$ and the internal emissivity value ϵ_{wi} in the reactor model.

Another improvement to the convergence behaviour was achieved by using systematic relaxation for successive iterations of the mole and energy balance equations. This was implemented using the following steps:

$$\left[Y_{pcb}^{n+1} \right] = \left[Y_{pcb}^{n} \right] + \left[\Delta Y_{pcb}^{n+1} \right] \qquad \textbf{(3-55)}$$

$$\left[Y_{pcb}^{n+2} \right] = \left[Y_{pcb}^{n+1} \right] + \left[\Delta Y_{pcb}^{n+2} \right] \qquad \textbf{(3-56)}$$

$$\left[Y_{pcb}^{n+1} \right] = \left[Y_{pcb}^{n} \right] + \left[\Delta Y_{pcb}^{n+1} \right] + wt \left[\Delta Y_{pcb}^{n+2} \right] \qquad \textbf{(3-57)}$$

and similarly for the energy balance equation:

$$\left[T^{n+1} \right] = \left[T^{n} \right] + \left[\Delta T^{n+1} \right] + wt \left[\Delta T^{n+2} \right] \qquad \textbf{(3-58)}$$

where wt is a weight factor, n the coupling iteration number and $[\Delta Y_{pcb}]$, $[\Delta T]$ are corrections calculated using the Newton-Raphson scheme (see Section 3.4). A weight factor of $wt = 0.25$ was found to be the best value to damp out oscillations encountered in successive iterations.

However, even with these modifications, for certain cases is was still difficult to obtain a converged solution. Hence the model was further modified so that it was possible to solve the energy balance equation using a transient algorithm, effectively using loading in time to obtain a solution. The thermal mass of the wall (thermocouple probe and the channel wall) is much greater than the gas phase. This means that the wall temperature is changing relatively slowly compared with the gas temperature and so the gas can be assumed to be at pseudo steady-state with the wall at any given instant in time. Hence, the ∂t term in Equation (3-7) is assumed equal to zero and the only transient term involved is the wall temperature. Provided that the time step is greater than the average residence time of the gas in the channel this assumption is valid. In this study the average residence time of the gas was less than 0.25 seconds and a time step of 10 seconds was found to give satisfactory results.

Solution of the transient problem has been previously addressed in the original development of the model for a monolith reactor [40]. Here a fourth order Runga-Kutta (RK4) method was implemented for solution of the wall temperature T_W, *viz*:

The wall boundary condition for the energy balance is rewritten as a function of temperature and concentration:

$$\frac{dT_W}{dt} = f(T_W,\ Y_{pcb_w}) \tag{3-59}$$

and then solved using the RK4 method as given below:

$$T_W^{t+\Delta t} = T_W^t + \frac{1}{6}(k_1 + 2k_2 + 2k_3 + k_4) \tag{3-60}$$

where:

$$k_1 = \Delta t\, f(T_W^t) \tag{3-61}$$

$$k_2 = \Delta t\, f(T_W^t + \tfrac{1}{2}k_1) \tag{3-62}$$

$$k_3 = \Delta t\, f(T_W^t + \tfrac{1}{2}k_2) \tag{3-63}$$

$$k_4 = \Delta t\, f(T_W^t + k_3) \tag{3-64}$$

The RK4 scheme was found to be fairly reliable except when axial wall conduction was included in the model. Curve-fitting a polynomial to the wall temperature still caused the system to become unstable. The RK4 scheme also requires solution of the coupled steady-state problem four times which is expensive in computation time. In order to alleviate these problems a new solution methodology was developed. The model was now solved in three stages, this would incorporate the axial wall conduction and wall end effects in a more rigorous way:

i) Solve the channel wall temperature profile using a one-dimensional finite element method; transient solution using a second order accurate Gear scheme for time discretization:

$$\frac{\partial T_W^t}{\partial t} = \frac{3T_W^t - 4T_W^{t-\Delta t} + T_W^{t-2\Delta t}}{2\Delta t} \qquad \textbf{(3-65)}$$

ii) Solve the thermocouple probe wall temperature profile using a one-dimensional finite element method; transient solution using the Gear scheme.

iii) Solve the gas phase mole and energy balance equations using the previously described steady state scheme, with the channel and probe wall temperatures imposed as Dirichlet boundary conditions.

This transient algorithm was found to be stable and reliable, it also gave consistant steady state results with the previous solution methodology described in Section 3.4. Figure 3-6 illustrates the effects incorporated in the model and the steps in the algorithm. Equation (3-11) is rewritten as a one-dimensional transient in temperature for the channel wall:

$$\begin{aligned}\frac{dT_{Wi}}{dt} = \frac{(-\Delta H_R)\,R_W}{\delta_w\,\rho_w\,Cp_w} + \frac{k_w}{\rho_w\,Cp_w}\left[\frac{\partial^2 T_{Wi}}{\partial z^2}\right] \\ - \frac{k_f}{\delta_w\,\rho_w\,Cp_w}\left[\frac{\partial T}{\partial r}\right]_{r=R} + \frac{(Q_{eR} + Q_{iR})}{\delta_w\,\rho_w\,Cp_w}\end{aligned} \qquad \textbf{(3-66)}$$

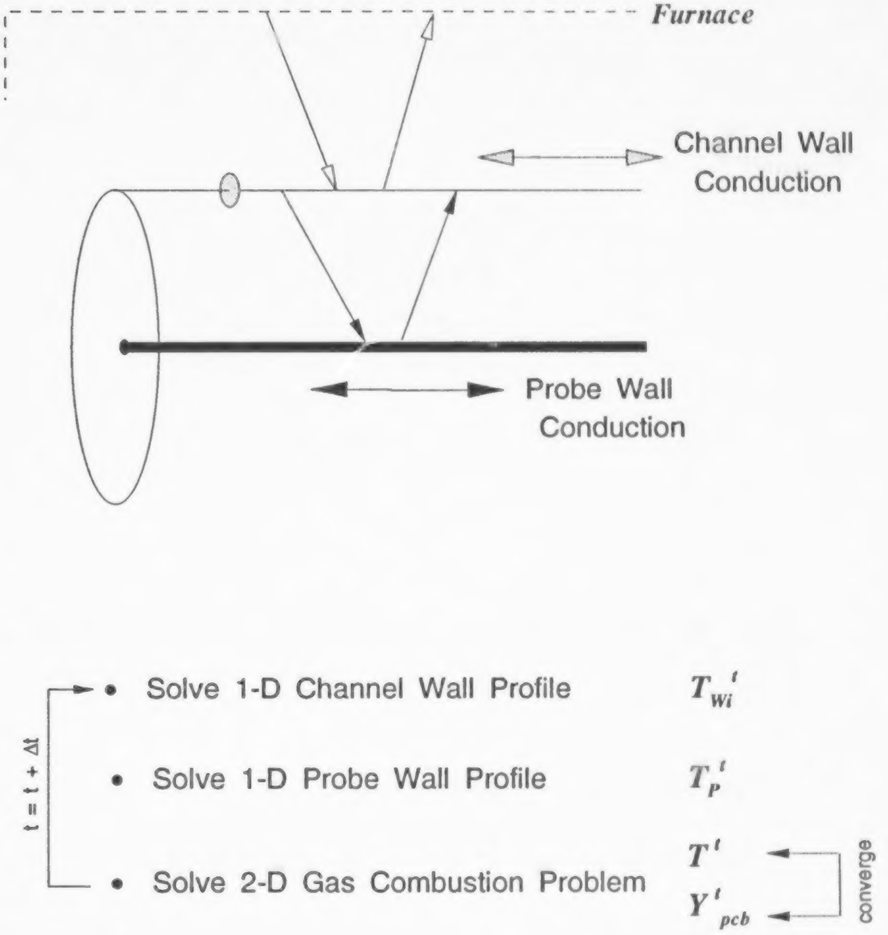
Furnace
Channel Wall Conduction
Probe Wall Conduction
Solve 1-D Channel Wall Profile
T_{Wi}^{t}
t = t + Δt
Solve 1-D Probe Wall Profile
T_{P}^{t}
Solve 2-D Gas Combustion Problem
T^{t}
Y^{t}_{pcb}
converge

Figure 3-6. The reactor model and the transient algorithm.

which is subject to the zero flux boundary condition (insulated) at the ends:

$$\frac{\partial T_{Wi}}{\partial z} = 0 \qquad @\ z = 0\ or\ L \tag{3-67}$$

Similarly for the probe wall, Equation (3-48) is rewritten as a one-dimensional transient in temperature:

$$\frac{dT_P}{dt} = \frac{k_p}{\rho_p\, Cp_p}\left[\frac{\partial^2 T_P}{\partial z^2}\right] - \frac{k_f}{\delta_p\, \rho_p\, Cp_p}\left[\frac{\partial T}{\partial r}\right]_{r=R_p} + \frac{Q_{iR}}{\delta_p\, \rho_p\, Cp_p} \tag{3-68}$$

which is subject to either the zero flux boundary condition (insulated):

$$\frac{\partial T_P}{\partial z} = 0 \qquad @\ z = 0\ or\ L \tag{3-69}$$

or the constant external temperature boundary condition at the ends, see Figure 3-7:

$$-\,k_p\frac{\partial T_P}{\partial z} = h_{eff}(T_P - T_{ref1}) \qquad @\ z = 0 \tag{3-70}$$

$$k_p\frac{\partial T_P}{\partial z} = h_{eff}(T_P - T_{ref2}) \qquad @\ z = L \tag{3-71}$$

where T_{ref} is a constant temperature that the probe cools down to over an exterior distance L^* which defines an effective heat transfer coefficient, h_{eff} :

$$h_{eff} = \frac{k_p}{L^*} \tag{3-72}$$

The transient equations for the channel and thermocouple probe wall problem, Equations (3-66) and (3-68) respectively, are discretised using 1-D quadratic finite elements and integrated using a four-point Gaussian quadrature scheme. Each 1-D quadratic element also forms one edge of a triangular P2 element that lies on the wall boundaries for the 2-D gas finite element problem. Hence, in order to solve the reactor

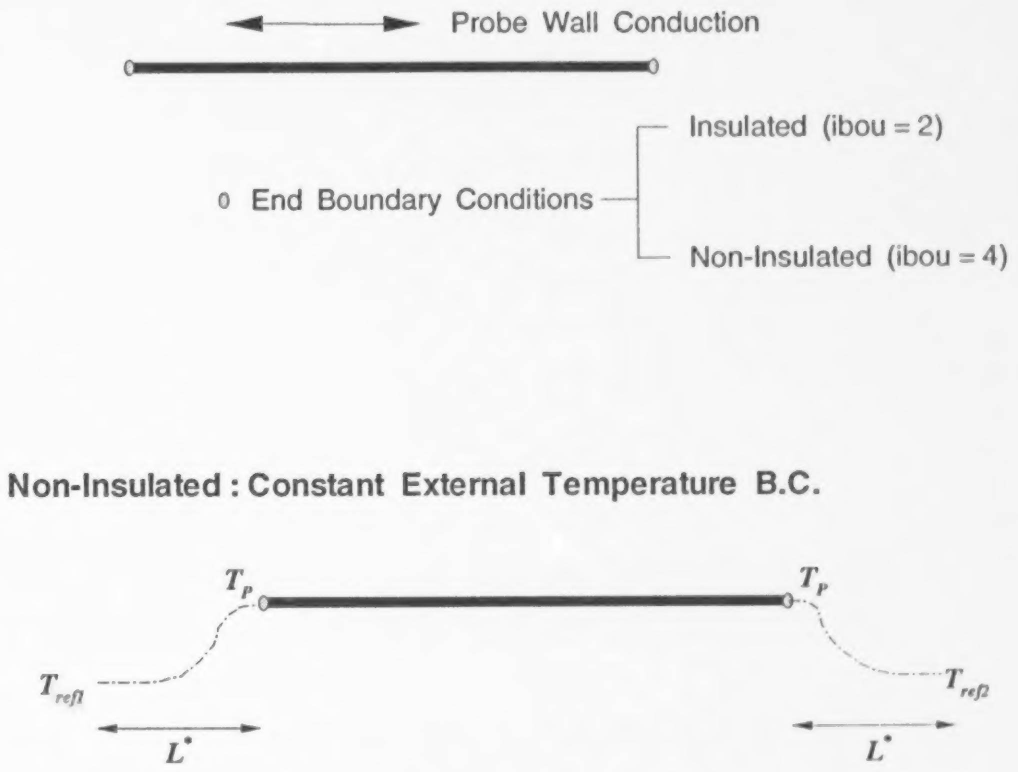
Probe Wall Conduction
Insulated (ibou = 2)
0 End Boundary Conditions
Non-Insulated (ibou = 4)
Non-Insulated : Constant External Temperature B.C.
T_P
T_P
T_{refl}
T_{ref2}
L^*
L^*

Figure 3-7. Non-insulated boundary condition for the probe.

model in the three stages explained above, it is necessary to transfer the nodal temperature values calculated from the transient wall problems onto the corresponding nodes that form the wall boundaries for the 2-D gas problem.

3.8 Validation of the Model

In order to have confidence in the results obtained using the reactor model, the implementation of the code and the selection of finite element mesh size, the following checks were made:

i) The Nusselt number for fully-developed thermal flow with constant wall temperature or constant wall flux should be 3.66 and 4.36 respectively. In the original development of the monolith model [40], the *Nu* number was computed at both of the described wall boundary conditions. The simulated *Nu* numbers were found to be within 1% of the analytical values.

ii) The global energy balance for the reactor channel with external radiation and PCB combustion (using the kinetics developed in Chapter 4) was checked by hand calculation. This gave satisfactory agreement with the results obtained with the model.

iii) Simulated results were compared utilising two different finite element meshes; a non-uniform mesh with 924 elements and a uniform mesh with 1984 elements, see Figure 3-2(b). The coarser non-uniform mesh gave identical temperature and concentration profiles as the uniform mesh.

Finally the different effects that can be incorporated in the reactor model with their respective model numbers are summarised in Table 3-4. These model numbers will be used in the description of the simulation results given in Chapter 4. For example, **Model 109 (annular velocity profile; ibou = 2)** represents a reactor model that uses a laminar developing velocity profile in an annulus, includes the effects of internal radiation and axial wall conduction, has an insulated boundary condition for the ends of the probe and is solved using the transient algorithm. A typical parameter file for the mathematical model of the monolith reactor is also shown in Appendix B.1.

Table 3-4. Options available in the reactor model.

Model Option No.	Effects Incorporated in the Model
velocity profile	laminar flow in empty tube or annular geometry
0 * *	fully developed flow
1 * *	developing flow over a distance L_D
* 0 *	internal radiation and axial wall conduction (see ibou option)
* 7 *	internal radiation but no axial wall conduction
* 6 *	no internal radiation and no axial wall conduction
* * 8	steady-state : temperature and concentration
* * 9	transient algorithm : temperature and concentration
ibou = 2	insulated B.C. for probe conduction
ibou = 4	constant external temperature B.C. for probe conduction

4

NUMERICAL RESULTS AND DISCUSSION

In this chapter the numerical results obtained using the reactor model described in Chapter 3 are presented and discussed. The consequence of including different phenomena in the reactor model and the evaluation of the homogeneous and catalytic kinetics are explained. Results are presented so that the reader can see how the work progressed and the conclusions that were drawn at successive stages. In this way the importance of including different effects in the model can be clearly shown. The chapter is divided into two sections corresponding to the two parts of the experimental work that were described in Chapter 2:

4A : Modelling of the uncoated channel experiments (homogeneous combustion)

4B : Modelling of the catalyst coated channel experiments (homogeneous and catalytic combustion)

Although the work is presented separately, the numerical modelling described in Sections 4A and 4B was not completed independently. The homogeneous kinetics derived in 4A were subsequently used in 4B when the effects of both homogeneous and catalytic reaction are studied. The results obtained in 4B also gave further insight into the modelling of the homogeneous experiments described in 4A.

4A : UNCOATED CHANNEL EXPERIMENTS

4A.1 Preliminary Homogeneous Kinetics

Recall from Section 3.3, the pseudo first order kinetics assumed for the homogeneous oxidation of the PCB mixture known as Aroclor 1242:

$$R_H = A_H \exp\left[-\frac{E_H}{R_g T}\right] \frac{P\,Y_{pcb}}{R_g T} \tag{4-1}$$

It was first necessary to ascertain if the homogenous combustion could be adequately modelled using first order dependent kinetics and if so, to obtain an idea of the magnitude of the two parameters A_H and E_H in the kinetic expression.

Initially to simplify the problem, a temperature independent homogeneous rate constant k_H (effectively E_H equals zero) was employed with a basic reactor model; empty tube velocity profile and no internal radiation in the channel (Model 068). Using this model the nine uncoated experiments given in Table 2-3 and 2-4 were simulated by altering the value of k_H to match the respective experimental conversions. Table 4-1 gives the values of k_H that matched the experimental conversions and the radial average temperature $T_{L/2}$ simulated at the midpoint of the reactor (z = 12.5 cm). Effectively these values of k_H are rate constants for the homogeneous combustion at different inlet PCB concentrations and inlet temperatures. Using the values of the simulated $T_{L/2}$ it was possible to write k_H in terms of a set of E_H and A_H values.

Selecting experiment number pcb1 (5,1a) for example, then from Table 4-1 :

$$k_H = A_H \exp\left[-\frac{E_H}{R_g T}\right] = 1.63\ s^{-1} \tag{4-2}$$

Table 4-1. Results for temperature independent kinetics

Experiment number	Experimental Y_{pcbL} (x 10^6)	Model Y_{pcbL} (x 10^6)	Rate constant k_H (s^{-1})	Model $T_{L/2}$ (K)
pcb1 (5, 1a)	2926	2928	1.63	834
pcb2 (5, 1b)	3289	3288	1.93	853
pcb3 (5, 1e)	4294	4289	3.26	922
pcb4 (5, 1c)	3830	3830	3.04	902
pcb5 (5, 1d)	4678	4678	1.99	874
pcb6 (10, 2b)	3977	3975	2.22	907
pcb7 (10, 2c)	2761	2763	6.87	1108
pcb8 (10, 2d)	2547	2548	6.88	1098
pcb9 (10, 2e)	2246	2249	9.44	1244

Model 068 ($E_H = 0$; empty tube velocity profile; correct average inlet velocity; coarse mesh; 924 elements) rearranging, a set of E_H and A_H values can then be calculated using $T_{L/2}$

$$A_H = \frac{k_H}{\exp\left[-\frac{E_H}{R_g\, T_{L/2}}\right]} = \frac{1.63}{\exp\left[-\frac{E_H}{8.314 \times 834}\right]} \qquad \textbf{(4-3)}$$

Figure 4-1 shows a plot of $\log(A_H)$ versus E_H using calculated values for each of the experiments based on the method explained in the example above. Each line on this plot gives a set of E_H and corresponding A_H values, that form a kinetic expression which matches the experimental conversion for that particular experimental run. It can be seen from Figure 4-1 that the lines intersect in the region of $E_H = 30 - 50$ kJ mol^{-1} and thus give a kinetic expression that satisfies all nine experimental runs. It was concluded that a first order kinetic model is reasonable for the homogeneous oxidation of PCB and the following estimate for the rate parameters were obtained:

$$E_H \simeq 40,000 \text{ J mol}^{-1}$$

$$A_H \simeq 562 \text{ s}^{-1}$$

However, it must be stressed that this is only a rough estimate since in deriving these rate parameters a temperature independent kinetic model was used and internal radiation effects were ignored.

4A.2 Temperature and Concentration Profiles

Typical temperature and concentration profiles generated using the Model 078 with an empty tube velocity profile and the preliminary homogeneous kinetics given above are given in Figures 4-2 to 4-4. From these plots the following points can be observed:

i) The rate of homogeneous reaction is highest adjacent to the channel wall. This is primarily due to the longer residence time of the gas.

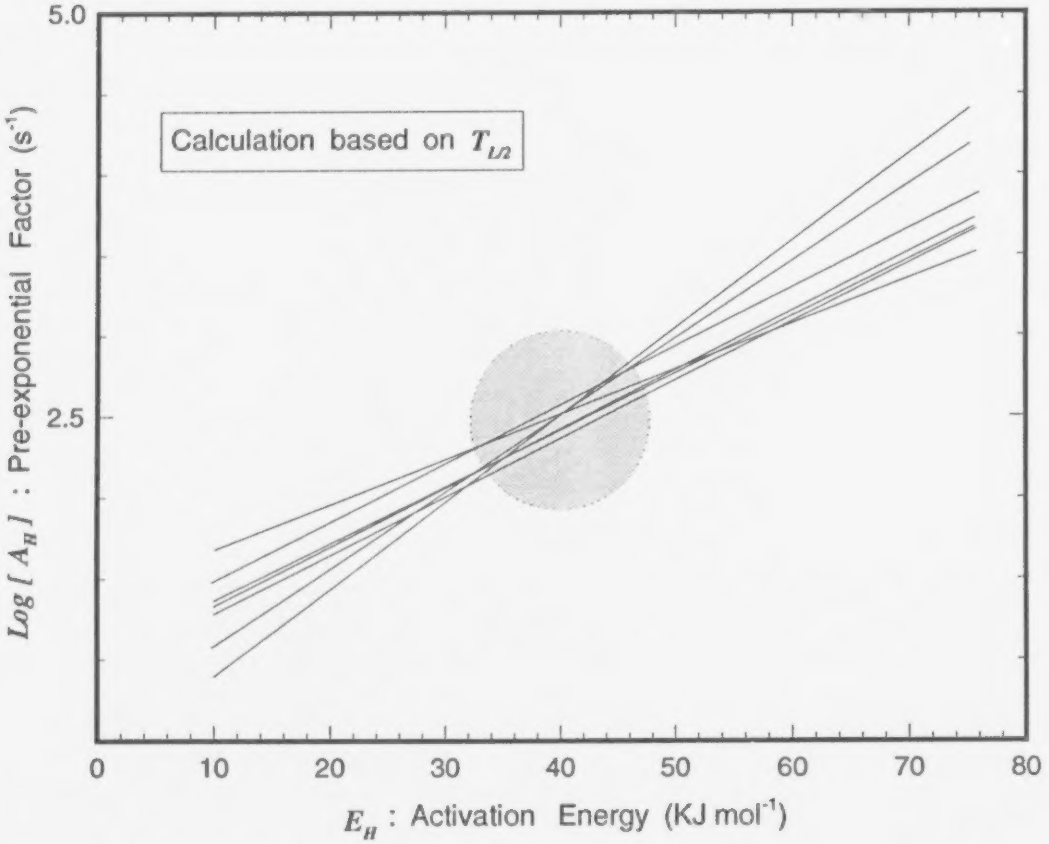

Figure 4-1. Preliminary homogeneous kinetics.

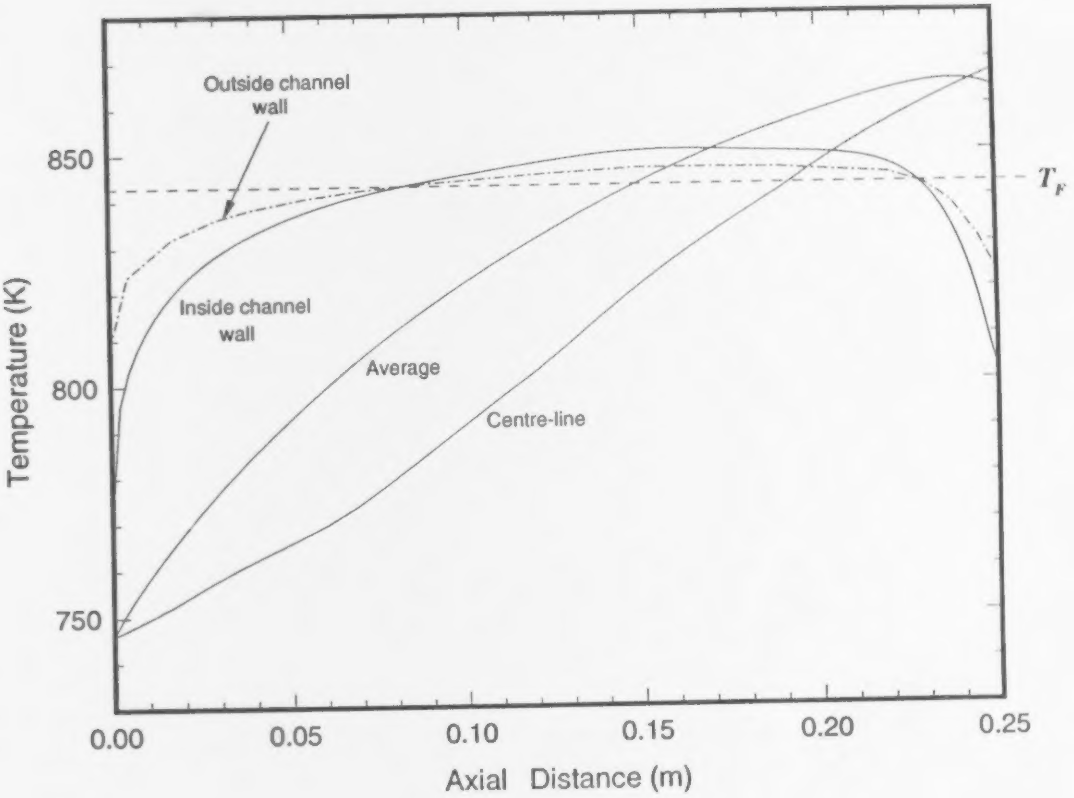

Model 078 (pcb1 (5, 1a); $A_H = 562\ \mathrm{s}^{-1}$, $E_H = 40\ \mathrm{kJ\ mol}^{-1}$; empty tube velocity profile;
$T_F = 843$ K; $T_{LR} = 450$ K; $\epsilon_{wi} = 0.5$; coarse mesh; 924 elements)

Figure 4-2. Simulated axial temperature profile.

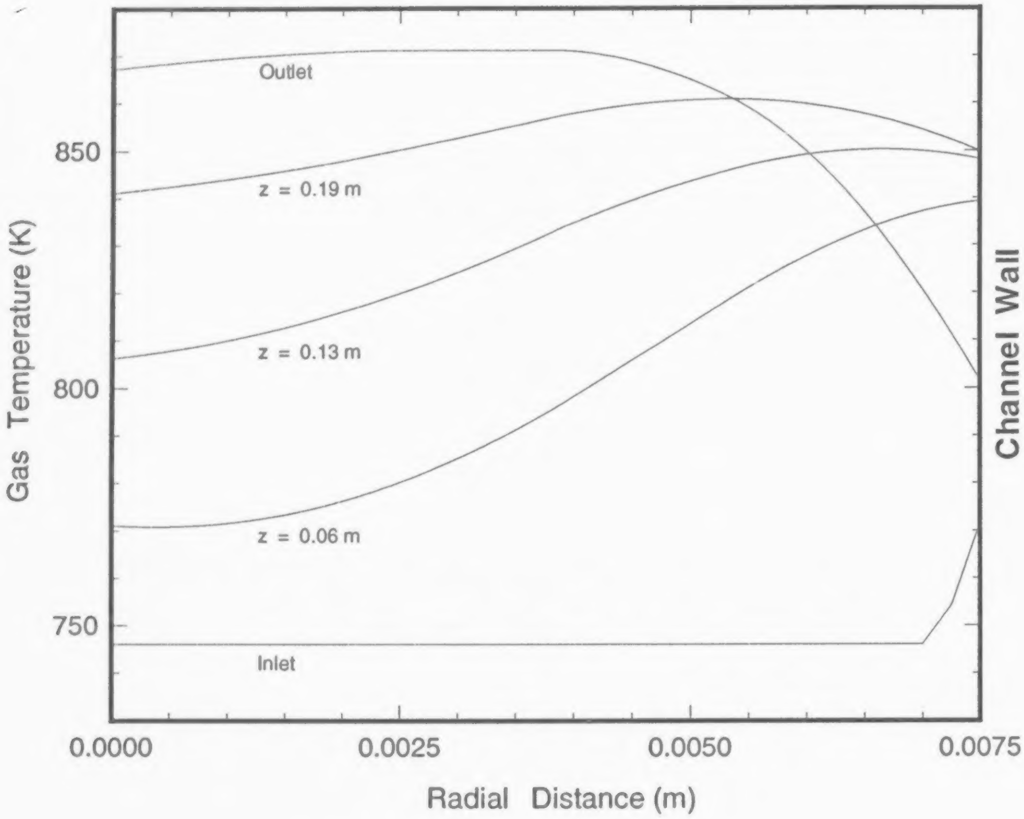

Model 078 (pcb1 (5, 1a); $A_H = 562\ \mathrm{s}^{-1}$, $E_H = 40\ \mathrm{kJ\ mol}^{-1}$; empty tube velocity profile; $T_F = 843$ K; $T_{LR} = 450$ K; $\epsilon_{wi} = 0.5$; coarse mesh; 924 elements)

Figure 4-3. Simulated radial temperature profile.

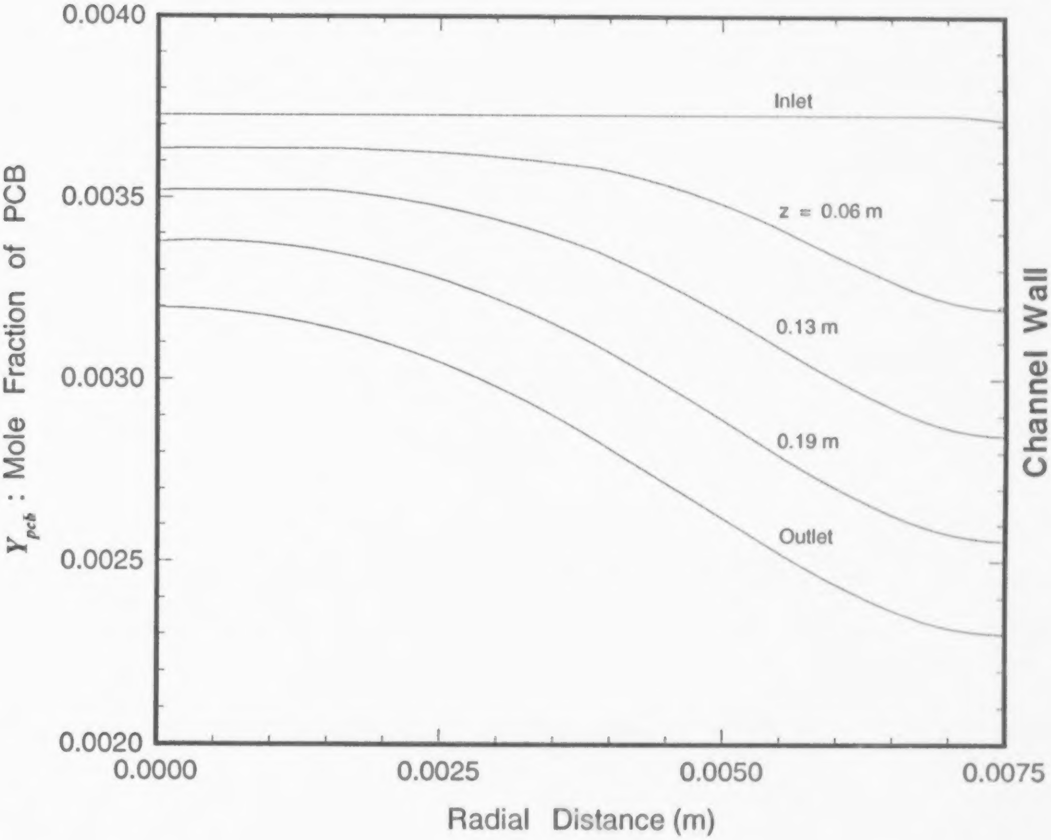

Model 078 (pcb1 (5, 1a); $A_H = 562\ s^{-1}$, $E_H = 40$ kJ mol^{-1}; empty tube velocity profile; $T_F = 843$ K; $T_{LR} = 450$ K; $\epsilon_{wl} = 0.5$; coarse mesh; 924 elements)

Figure 4-4. Simulated radial concentration profile.

ii) The wall temperature drops off close to the channel exit due to internal radiation out the exit of the channel. The extent of the drop off in channel wall temperature is affected by the outlet temperature that the channel surface is radiating to T_{LR}. It is difficult to know the value of T_{LR} with accuracy, since it will depend on the outlet gas temperature and the extent of heat loss from the reactor system beyond the exit. In the reactor model a value of $T_{LR} = 450$ K was used which was thought to be reasonable. Later, the sensitivity of the model results to the T_{LR} value will be shown. Similarly, for radiation out of the entrance of the channel, the inlet radiation temperature T_{OR} was set equal to the average inlet gas temperature T_O.

iii) The radiation exchange between the external channel wall and the furnace, switches direction at $z = 0.08$ m as combustion proceeds and the wall temperature exceeds the furnace temperature T_F. Notice the corresponding behaviour of internal and external channel wall temperatures. This switch in the direction of radiation transfer occurs again at $z = 0.23$ m when the wall temperature drops off due to radiation out of the exit. Effectively the channel wall is heating and cooling the gas at different regions along the reactor length.

iv) The radial temperature profiles are non-uniform and steep near the wall. This demonstrates the superiority of a 2-D mathematical model. Note that the radial profiles at the end of the reactor have a maximum between the wall and the centre-line. This is caused by the wall cooling the gas when it is radiating to the furnace.

v) The axial centre-line temperature profile is significantly different from the shape of the experimental profiles measured with the thermocouple probe (see Figure 2-3). This highlights the difference between the empty tube centre-line temperature and the corresponding centre-line probe wall temperature.

4A.3 Optimisation of the Homogeneous Kinetics

Section 4A.1 describes how an initial estimate was determined for the kinetic constants for the homogeneous combustion of the PCB. The next stage in the work was to optimize the value of the two parameters A_H and E_H in the kinetic expression so that the model gave the closest match to the experimental conversions. This was achieved by determining values of A_H and E_H which minimised the sum of the residual square errors ΣR^2 between the experimental and simulated outlet PCB mole fraction Y_{pcbL} for the nine experiments. The sum of the squares of the residual error is given by:

$$\sum_{1}^{9} R^2 = \left[\frac{Exp.\ Y_{pcbL} - Model\, Y_{pcbL}}{Exp.\ Y_{pcbL}}\right]^2 \qquad \textbf{(4-4)}$$

From Figure 4-1 it was concluded that the activation energy for the reaction was in the range E_H = 30 - 50 kJ mol^{-1}. Thus, initially setting E_H = 30 kJ mol^{-1}, the reactor model was run at a selected A_H value for each of the experimental conditions. Using Equation (4-4) a value of ΣR^2 was then calculated for E_H = 30 kJ mol^{-1} at that particular A_H value. The A_H value in the reactor model was then changed and the procedure repeated to calculate a series of ΣR^2 values. These values were then plotted and, by using a third order polynomial curve fit, Figure 4-5 was obtained. The minimum of this curve corresponds to the best value of the kinetic parameter A_H at E_H = 30 kJ mol^{-1}.

This process was repeated to obtain ΣR^2 versus A_H curves at E_H values of 40, 45 and 50 kJ mol^{-1}. If all these curves are now merged onto a 3-D contour plot, the lowest point represents the optimum homogeneous kinetic parameters. This is shown in Figure 4-6, where ΣR^2 is the contour variable. The optimum kinetic expression was found to be:

$$R_H = 473 \exp\left(-\frac{38{,}010}{R_g T}\right)\frac{P\, Y_{pcb}}{R_g T} \qquad \textbf{(4-5)}$$

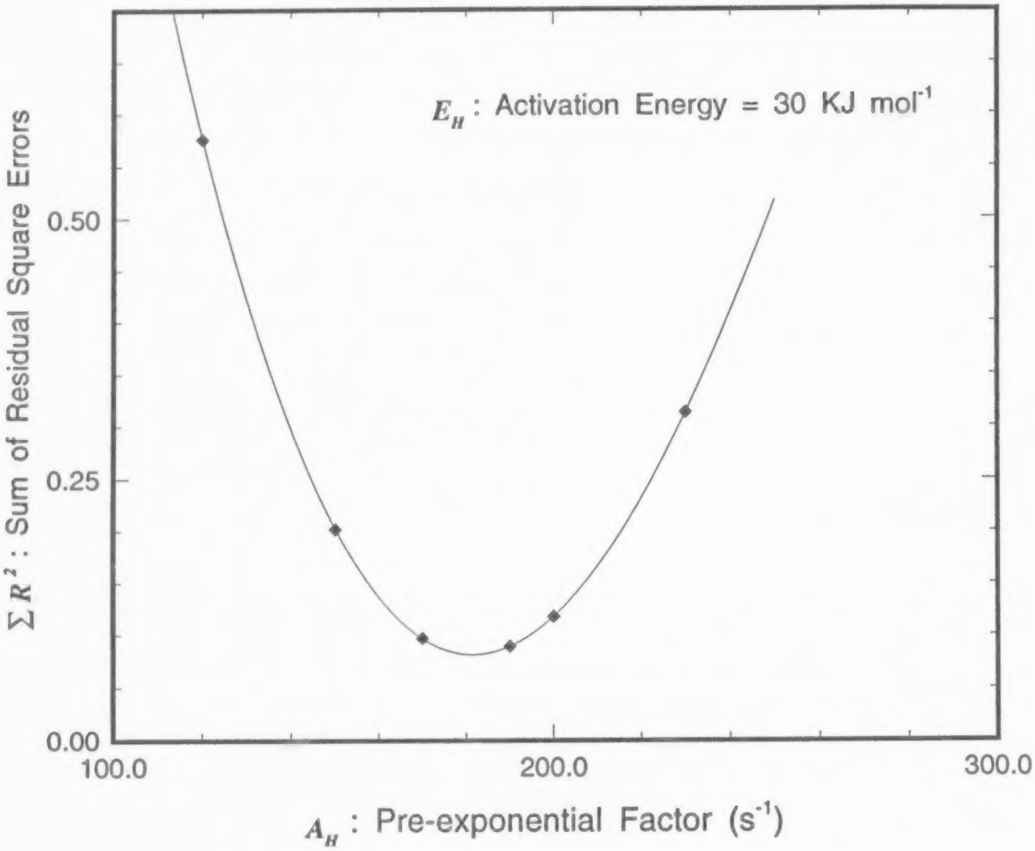

Figure 4-5. Plot showing the minimisation of the residual square error.

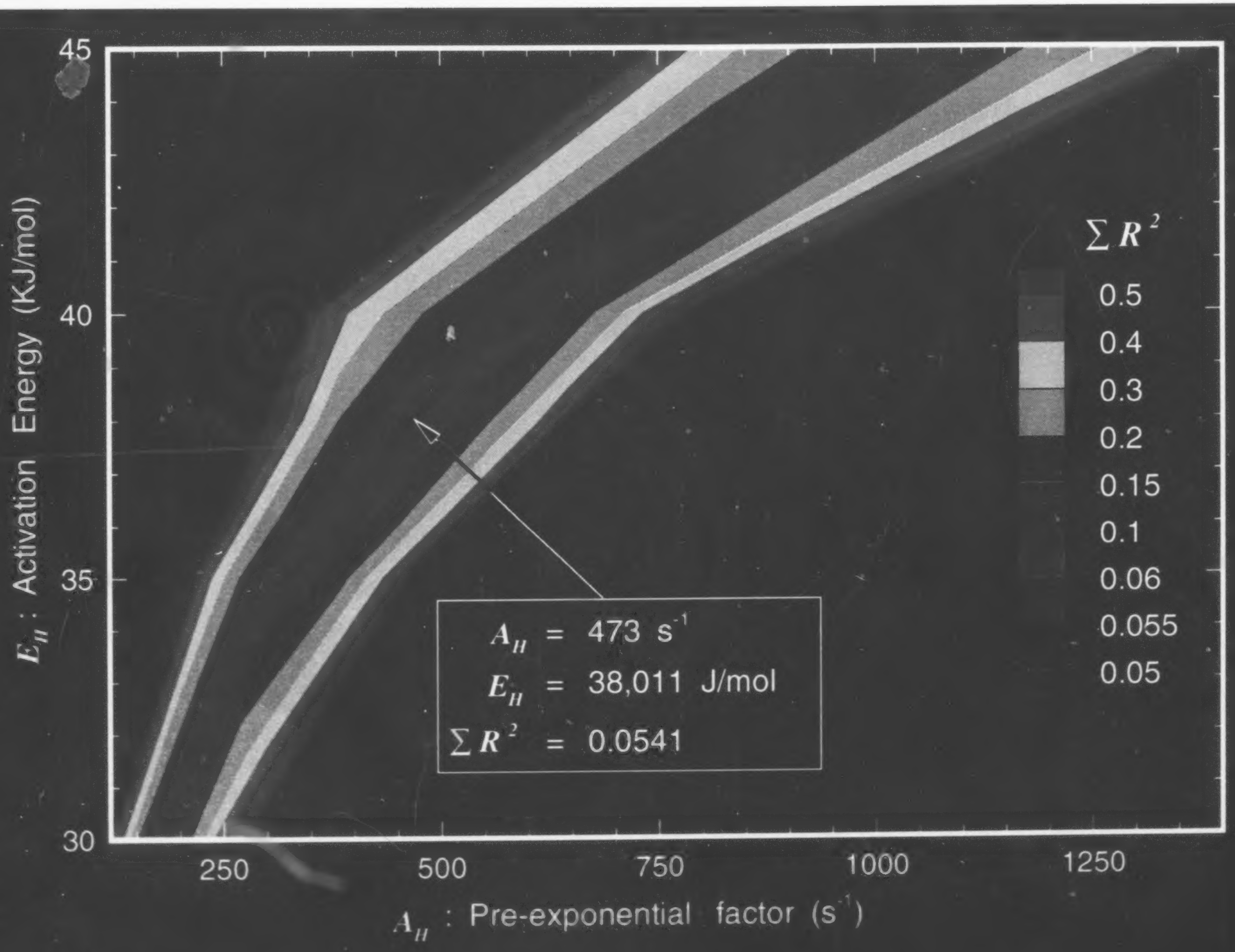

Figure 4-6. Residual square error contour plot.

A basic reactor model was used to derive this expression; empty tube velocity profile with no internal radiation or wall conduction in the channel (Model 068). Although this reactor model is relatively basic, in Section 4A.7 it will be shown that the kinetic expression is still valid if the complete reactor model is used.

Table 4-2 shows a comparison between the experimentally measured data and the results obtained using the reactor model with the homogeneous kinetics of Equation (4-5). By plotting these results on a logarithmic scale, see Figures 4-7, it can be seen that the predicted outlet PCB mole fractions are within 15% of the experimental values. Note that the predicted outlet average gas temperatures T_L given in Table 4-2 are considerably higher than the temperatures measured using the thermocouple probe.

4A.4 Incorporation of the Thermocouple Probe in the Model

In the previous sections it was shown that the temperatures measured with the thermocouple probe were significantly different from the centre-line and average temperature profiles simulated with an empty tube reactor model. This is because the thermocouple measures the temperature of the gas adjacent to probe wall which is affected by; zero gas velocity at the probe wall; internal radiation and axial wall conduction. In order to develop an accurate model of the reactor system the influence of the probe wall was incorporated.

Model 078 with an annular velocity profile and the homogeneous kinetics given in Equation (4-5) was used to simulate one of the experimental runs; pcb1 (5, 1a). The generated axial temperature profiles at different T_{LR} values are illustrated in Figure 4-8. The following can be observed:

i) Comparison of the probe profile with the empty tube profiles given in Figure 4-2, shows that the simulated results are significantly different.

ii) The shape of the probe wall profile is now more consistent with that of the measured profile.

Table 4-2. Evaluation of the homogeneous kinetics

Homogeneous Kinetics: E_H = 38,010 J mol^{-1}; A_H = 473 s^{-1}						
Experiment number	Y_{pcbL} Outlet mole fraction (x 10^6)		X_{pcb} Outlet conversion		T_L Outlet gas temperature (K)	
	Exp.	Model	Exp.	Model	Exp.*	Model †
pcb1 (5, 1a)	2926	2782	0.215	0.254	737	885
pcb2 (5, 1b)	3289	3184	0.243	0.267	734	905
pcb3 (5, 1e)	4294	4643	0.350	0.297	743	969
pcb4 (5, 1c)	3830	4147	0.338	0.283	746	941
pcb5 (5, 1d)	4678	4397	0.245	0.290	747	953
pcb6 (10, 2b)	3977	3555	0.260	0.338	802	990
pcb7 (10, 2c)	2761	2896	0.523	0.499	893	1164
pcb8 (10, 2d)	2547	2743	0.526	0.490	888	1146
pcb9 (10, 2e)	2246	1954	0.590	0.643	1012	1310

ΣR^2 Residual square error	0.057

Model 068 (empty tube velocity profile; correct average inlet velocity; coarse mesh; 924 elements)

* Experimentally measured outlet temperature using the thermocouple probe.

† Radial average outlet temperature calculated by reactor model.

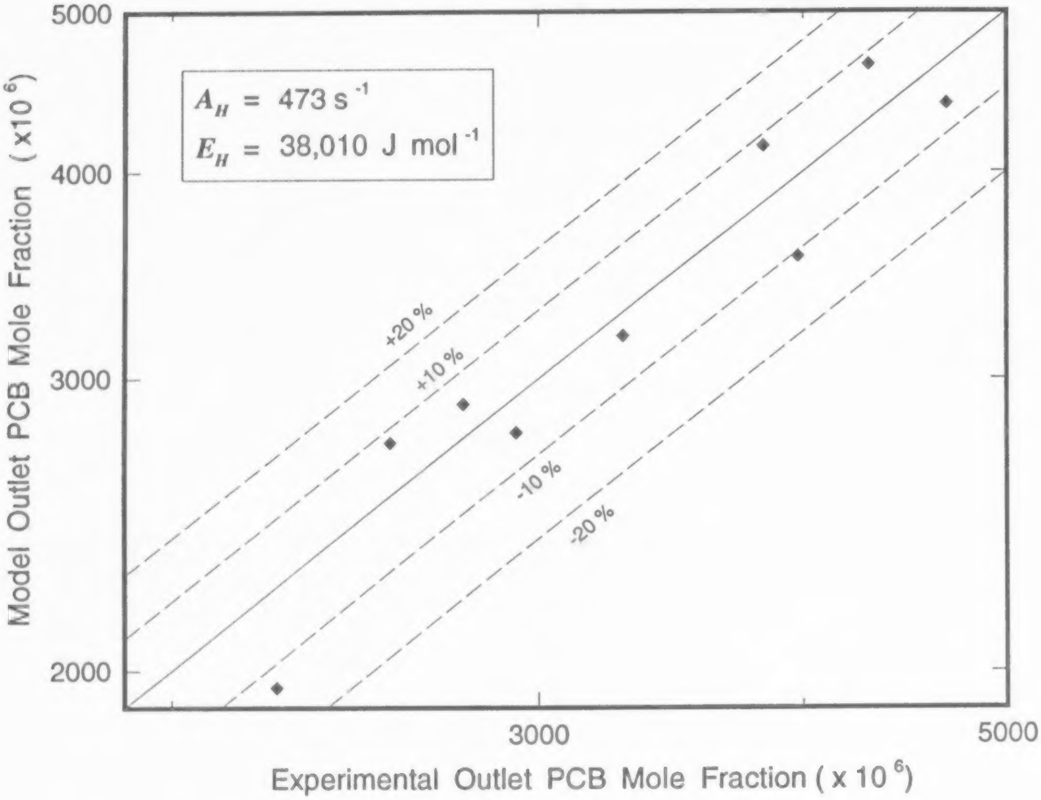

Figure 4-7. Evaluation of the homogeneous kinetics : Outlet mole fraction of PCB.

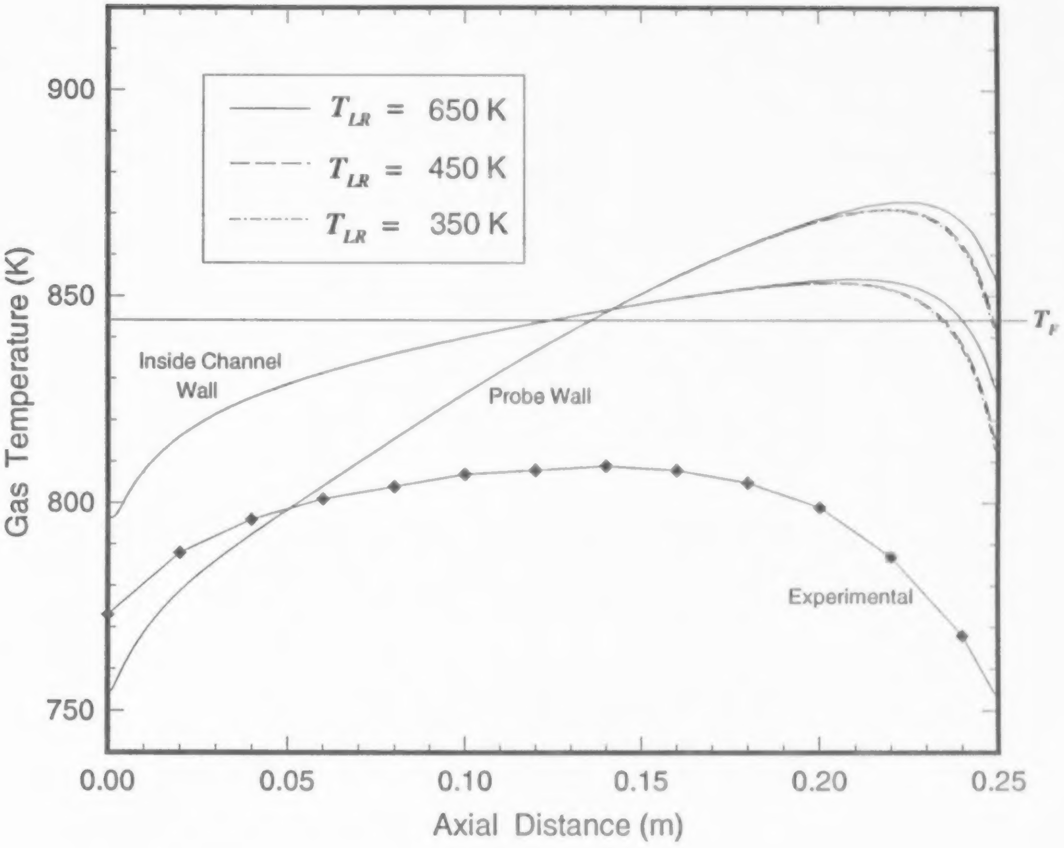

Model 078 (pcb1 (5, 1a); annular velocity profile; uniform mesh; 1654 elements; ϵ_{wl} = 0.4)

Figure 4-8. Axial temperature profiles with an annular geometry and at different T_{LR} values.

iii) The direction of radiation transfer between the external channel wall and the furnace; and the internal channel wall and the probe wall changes as combustion proceeds.

iv) The extent of drop off of the wall temperatures is not significantly effected by a value of T_{LR} less than 450K.

Corresponding radial temperature profiles are given in Figure 4-9 and the internal radiation fluxes in Figure 4-10. A positive flux signifies that the direction of net radiation is out from the surface and *vice versa*. Radiation to the reactor entrance and exit, and radiation exchange between the probe and channel wall are apparent. Simulated outlet conversions and average temperatures given in Table 4-3 also show the consequence of introducing a probe in the model.

Table 4-3. Effect of the thermocouple probe on the simulation

Simulation results for experiment number : pcb1 (5, 1a)		
Model description	Model Y_{pcbL} (x 10^6)	Model T_L (K)
Model 068 : Empty tube velocity profile	2782	885
Model 068 : Annular velocity profile	2772	893
Model 168 : Annular velocity profile and developing flow	2766	894
Model 078 : Annular velocity profile and internal radiation	2772	885

Model *68 (empty tube or annular velocity profile; correct inlet average velocity; 1654 or 924 elements)
Model 078 (annular velocity profile; uniform mesh; 1654 elements; ϵ_{wi} = 0.4; T_{LR} = 450 K)

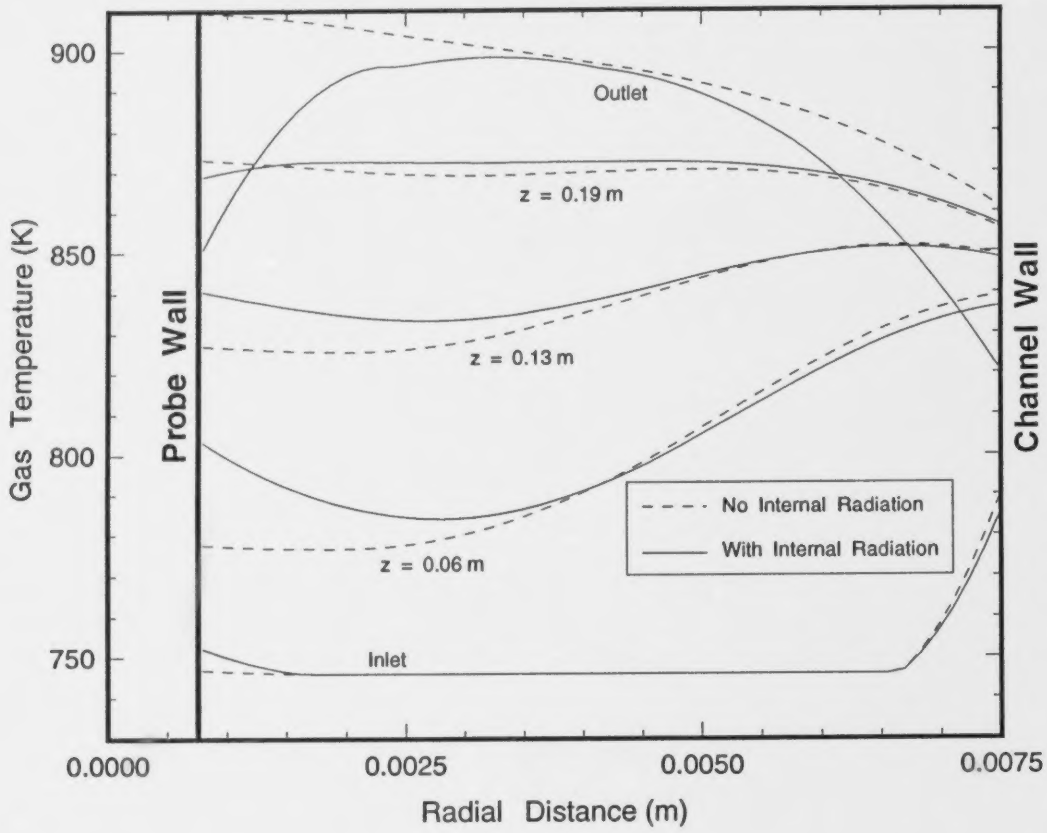

Model 068 (pcb1 (5, 1a); annular velocity profile; uniform mesh; 1654 elements)
Model 078 (pcb1 (5, 1a); annular velocity profile; uniform mesh; 1654 elements; $\epsilon_{wi} = 0.4$; $T_{LR} = 450$ K)

Figure 4-9. Radial temperature profiles with an annular geometry : effect of internal radiation.

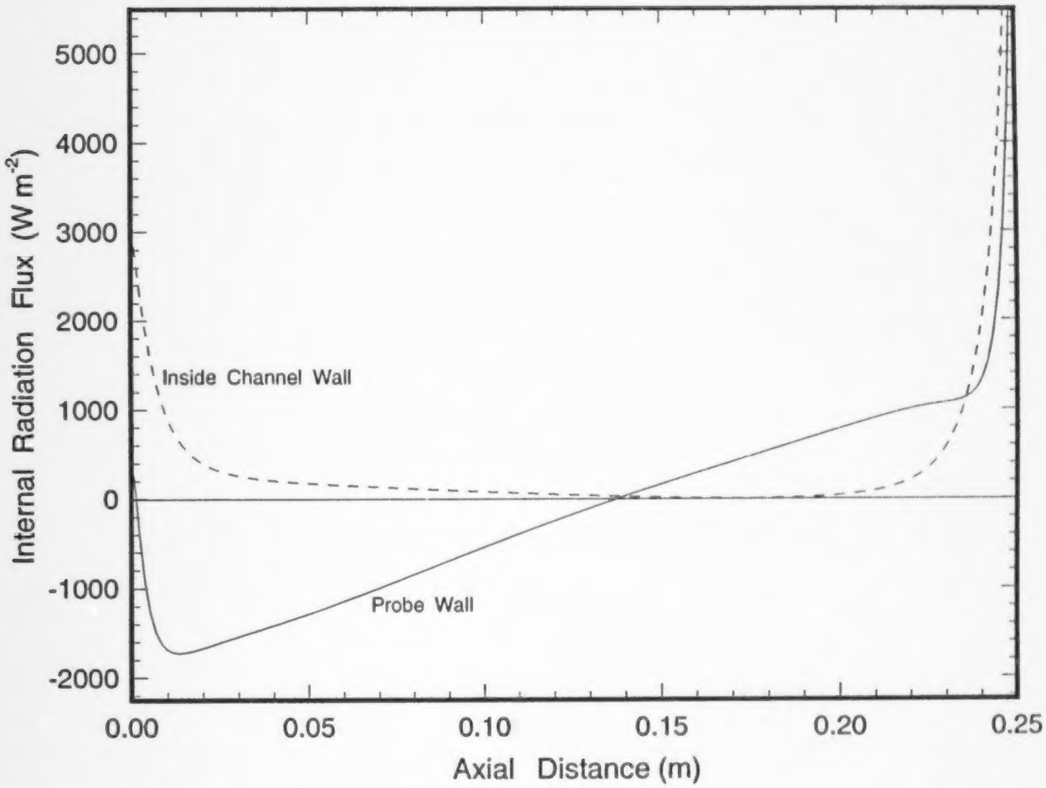

Model 078 (pcb1 (5, 1a); annular velocity profile; uniform mesh; 1654 elements; ϵ_{wi} = 0.4; T_{LR} = 450 K)

Figure 4-10. Internal radiation flux plot

As can be seen from the table, Model *68 was employed with both a developing and a fully developed velocity profile. The following was concluded:

i) At the same mass flowrates, the conversion in the annular geometry is slightly higher than the empty tube. This is a consequence of a greater tendency towards a plug flow profile in the annular geometry.

ii) Developing flow causes a slight increase in conversion over the fully developed case. This is due to the presence of a plug profile at the inlet of the channel when the flow is developing. However, at a developing length of $L_D \approx 6$ cm the effect was found to be minimal and the temperature profiles are virtually identical with the fully developed case.

iii) Although internal radiation affects the wall temperature profiles there is not a significant effect on the outlet conversion. A decrease in the average outlet temperature is apparent due to radiation from the channel and probe wall to the exit.

It was now necessary to assess the effect of including axial wall conduction in the reactor model. Figures 4-11 and 4-12 show the axial temperature profiles simulated using Model 009 with an insulated probe boundary condition (ibou = 2) and a constant external temperature boundary condition (ibou = 4). From these plots the following can be observed:

i) Axial wall conduction tends to flatten out the wall temperature profiles particularly near the entrance and exit of the channel.

ii) As expected the non-insulated boundary condition at the ends of the probe leads to a decrease in the wall temperatures near to the entrance and exit of the channel. As before with T_{LR} (the outlet temperature for radiation) it is difficult to know exactly what value to use for T_{ref2}; the outlet reference temperature for the probe boundary condition. For this simulation it was assumed that the probe wall will cool down to

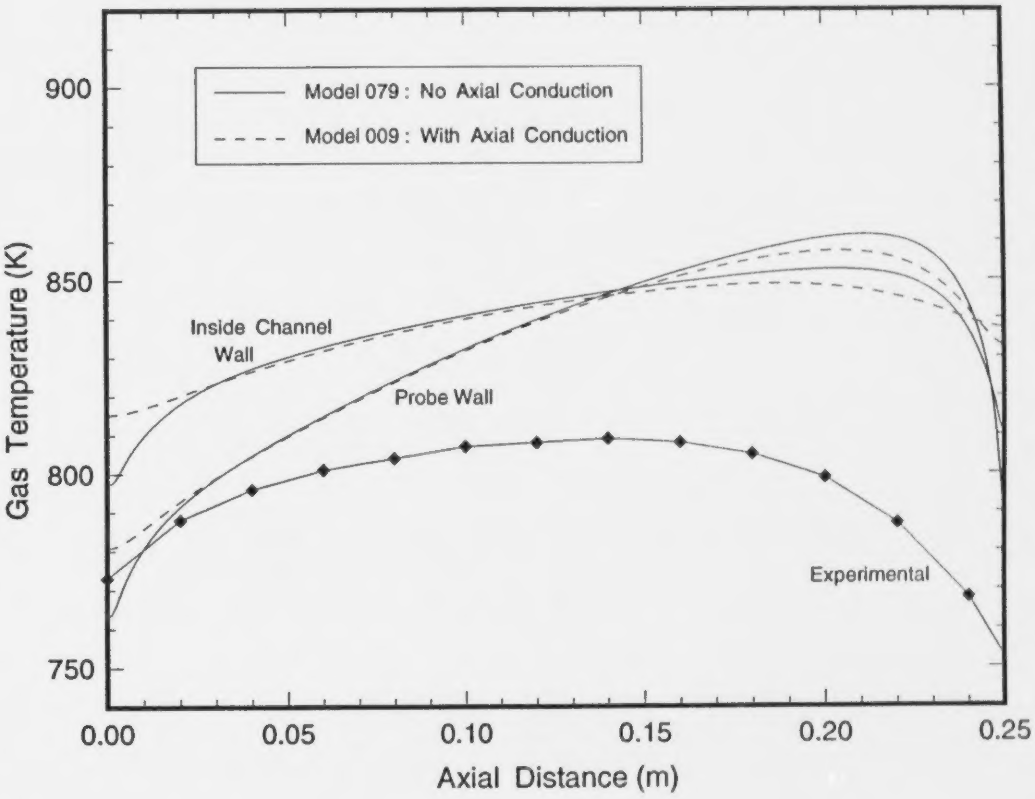

Model 079 (pcb1 (5, 1a); annular velocity profile; uniform mesh; 1654 elements; $\epsilon_{wi} = 0.5$; $T_{LR} = 450$ K)
Model 009 (...... $\epsilon_{wi} = 0.5$; $T_{LR} = 450$ K; ibou = 2)

Figure 4-11. Axial temperature profiles with and without axial wall conduction.

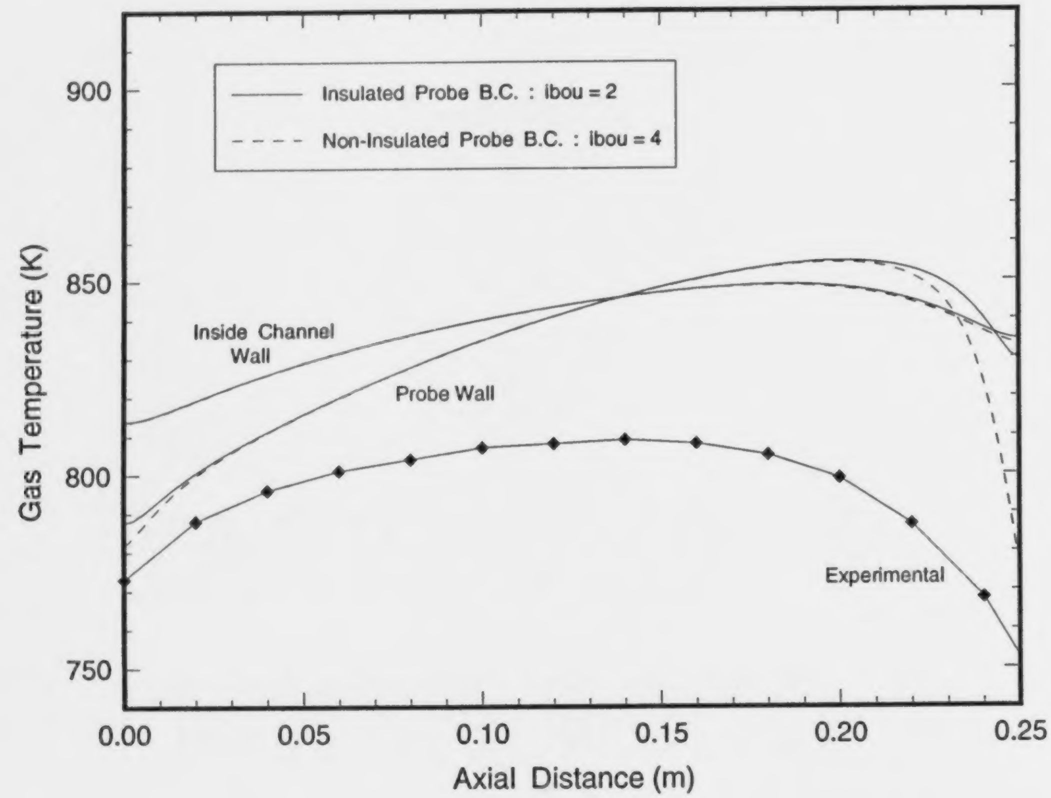

Model 009 (pcb1 (5, 1a); annular velocity profile; 1654 elements; $\epsilon_{wi} = 0.5$; $T_{LR} = 450$ K; ibou = 2)
Model 009 (...... ibou = 4; $h_{eff} = 440$ W m^{-2}; $T_{ref1} = T_O$; $T_{ref2} = 450$ K)

Figure 4-12. Axial temperature profiles with different probe boundary conditions.

T_{ref2} = 450 K over an exterior distance $L^* = 0.05$ m so that $h_{eff} = 440$ W m^{-2}. For the inlet reference temperature T_{ref1} it was assumed that heat losses are minimal preceding the channel entrance and so the average inlet gas temperature was used *ie* $T_{ref1} = T_O$.

4A.5 Heat and Mass Transfer Coefficients

The wall heat and mass transfer coefficients are commonly represented by the Nusselt number and the Sherwood numbers. The Nusselt number is a measure of the overall rate of heat transfer from surface to fluid compared with a theoretical rate which can be achieved by conduction alone with a static fluid. For the channel wall at $r = R$ and similarly for the probe wall at $r = R_p$ the Nu number can be defined as:

$$Nu = \frac{2R}{(T_{wi} - T_{avg})} \left[\frac{\partial T}{\partial r} \right]_{r=R} \qquad \textbf{(4-6)}$$

The Sherwood number can be similarly interpreted as the ratio of the actual mass transfer coefficient to the purely diffusive value. For the channel wall at $r = R$ and similarly for the probe wall at $r = R_p$ the Sh number can be defined as:

$$Sh = \frac{2R}{(Y_{pcb_{avg}} - Y_{pcb_w})} \left[\frac{\partial Y_{pcb}}{\partial r} \right]_{r=R} \qquad \textbf{(4-7)}$$

where the subscript *avg* in both equations denotes the average quantity across the channel radius. These quantities are defined by the following two equations:

$$T_{avg} = \frac{\int_{R_p}^{R} V_z(r)\, \rho\, Cp\, T(r)\, 2\pi r\, dr}{\int_{R_p}^{R} V_z(r)\, \rho\, Cp\, 2\pi r\, dr} \qquad \textbf{(4-8)}$$

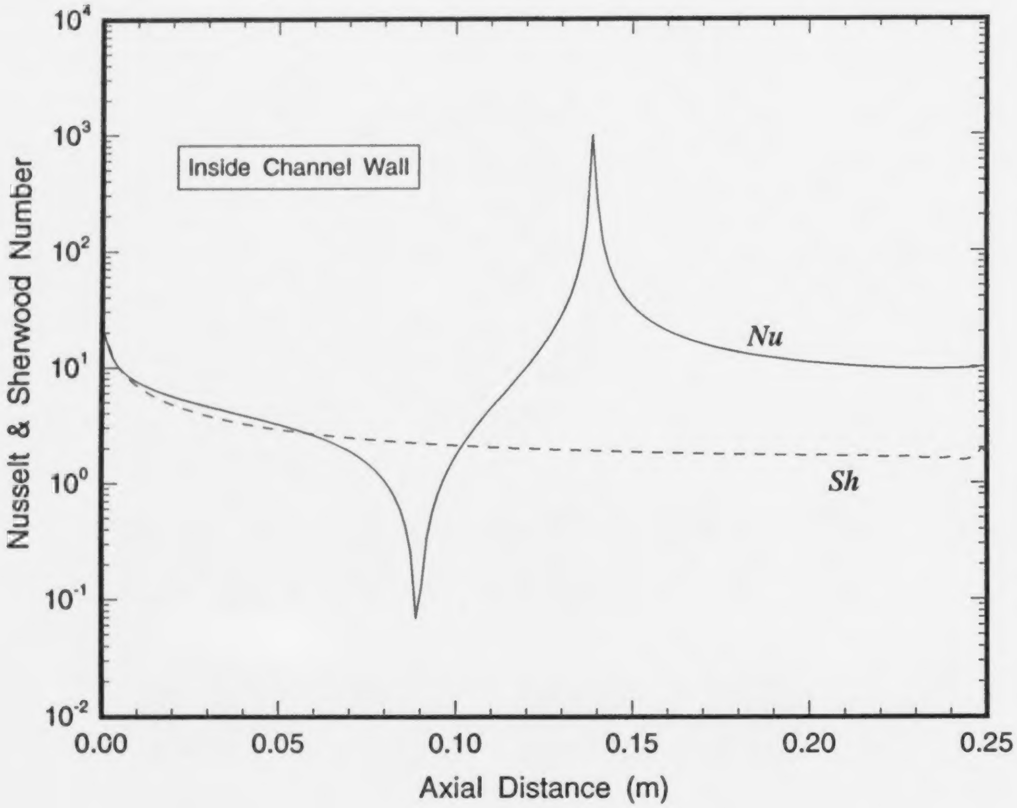

Model 079 (pcb1 (5, 1a); annular velocity profile; uniform mesh; 1654 elements; $\epsilon_{wi} = 0.5$; $T_{LR} = 450$ K)

Figure 4-13(a). *Sh* and *Nu* number plot for the inside channel wall.

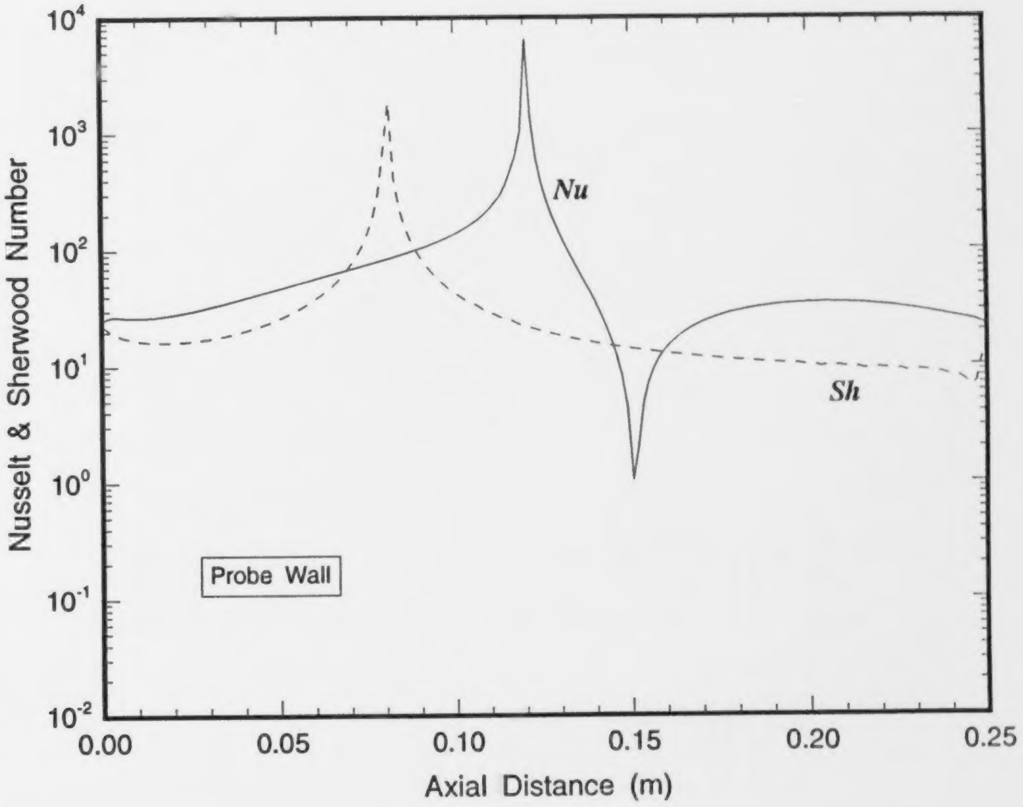

Model 079 (pcb1 (5, 1a); annular velocity profile; uniform mesh; 1654 elements; $\epsilon_{wi} = 0.5$; $T_{LR} = 450$ K)

Figure 4-13(b). *Sh* and *Nu* number plot for the outside probe wall.

$$Y_{pcb_{avg}} = \frac{\int_{R_p}^{R} V_z(r)\, Y_{pcb}(r)\, 2\pi r\, dr}{\int_{R_p}^{R} V_z(r)\, 2\pi r\, dr} \qquad \textbf{(4-9)}$$

Figures 4-13(a) and 4-13(b) show typical *Nu* and *Sh* number plots for the channel wall and the probe wall. Internal and external radiation transfer as well as the presence of the combustion reaction causes the flow to be thermally non-developed. Consequently, the *Sh* and *Nu* number curves show discontinuities as the direction of heat or mass transfer at the wall changes or there is a switch in the magnitude of the average and wall values. This demonstrates the difficulty of obtaining accurate correlations for the heat and mass transfer coefficients and hence the advantage of using a 2-D model.

4A.6 Sensitivity Analysis

Table 4-4 gives the expected accuracy of the parameters that are used in the reactor model. With this in mind, the reactor model was used to determine the consequence of a variation in some of the parameter values and the importance of having accurate parameter data. Table 4-5 shows that Y_{pcbL} is most sensitive to the value of the average inlet velocity and gas temperature. Notice that the inlet temperature was reduced from T_O = 746K (the temperature measured upstream of the reactor entrance using the thermocouple probe) to a value of 733 K. This was performed so that a better match between the simulated and measured inlet probe temperatures was achieved. The radial wall conduction resistance was also reduced to a value of $\lambda_w = 1.15 \times 10^{-3}$ K m^2 W^{-1} by setting the conduction resistance of the air gap equal to zero. This showed the maximum effect of radiation transfer that occurs between the outside ceramic wall and the inside stainless steel wall *ie* across the air gap. Figures 4-14 to 4-17 show the corresponding variation in the wall temperature profiles for a change in the furnace temperature, average inlet velocity, internal emissivity value, radial wall conduction resistance and the average inlet temperature.

Table 4-4. Accuracy of the parameters in the model

Model parameter	Expected accuracy of parameter
$\langle V_{Zo} \rangle$ Average inlet velocity	$\pm$ 0.080 m s^{-1}
T_F Furnace temperature	$\pm$ 5 K
T_O Inlet temperature*	$\pm$ 3 K
Y_{pcbo} Inlet PCB mole fraction	$\pm$ 200 x 10^6
Y_{pcbL} Outlet PCB mole fraction - HPLC†	$\pm$ 200 x 10^6
ϵ_{we} Emissivity of external channel wall	0.6 - 0.9
ϵ_{wi} Emissivity of inside walls	0.5 - 0.9
T_{LR} Outlet temp. for internal radiation‡	400 - T_L K
T_{ref2} Outlet reference temp. for probe B.C.‡	400 - T_L K
ΔH_R Heat reaction - group contribution method	$\pm$ 280 kJ (mol of PCB)$^{-1}$
D Molecular diffusion coefficient	$\pm$ 2.5 x 10^{-6} m^2 s^{-1}
P Total pressure (Pa)	$\pm$ 10 Pa
λ_w Radial wall conduction resistance◇	$\pm$ 7.5 x 10^{-4} K m^2 W^{-1}

* Due to the presence of internal radiation, zero velocity and axial wall conduction, the inlet temperature measured with the thermocouple probe is only a rough indication of the average inlet temperature of the gas.

† The outlet PCB concentration was measured using an HPLC technique. As only PCB compounds showed up in the analysis, this value is a measure of the disappearance of PCB in the reactor and not necessarily the amount of PCB that underwent complete combustion.

‡ This value is dependent on the outlet gas temperature and the extent of heat loss from the experimental apparatus beyond the channel exit.

◇ Radiation transfer across the air gap will reduce the effective heat transfer resistance of the channel wall.

Table 4-5. Sensitivity analysis on the model parameters

Simulation results for experiment number : pcb1 (5, 1a)		
Model description	Model Y_{pcbL} (x 10^6)	Model T_L (K)
Basis simulation : Model 009*	2779	877
Furnace temperature :		
T_F = 848 K	2764	882
T_F = 838 K	2794	872
Average inlet velocity :		
$\langle V_{Zo} \rangle$ = 1.573 m s^{-1}	2830	874
$\langle V_{Zo} \rangle$ = 1.413 m s^{-1}	2723	879
External wall emissivity :		
ϵ_{we} = 0.5	2783	876
Internal wall emissivity :		
ϵ_{wi} = 0.6	2780	877
Inlet temperature :		
T_O = 733 K	2822	872
Heat of reaction for PCB :		
ΔH_R const. A = -5853 kJ mol^{-1}	2771	880
ΔH_R const. A = -5293 kJ mol^{-1}	2787	873
Radial wall resistance :		
λ_w = 9.16 x 10^{-3} K m^2 W^{-1}	2780	877
λ_w = 7.66 x 10^{-3} K m^2 W^{-1}	2778	877
λ_w = 1.15 x 10^{-3} K m^2 W^{-1}	2768	878

* Model 009 (annular velocity profile; uniform mesh; 1654 elements; T_{LR} = 450 K; ibou = 4; T_{ref1} = T_O; T_{ref2} = 450 K; h_{eff} = 440 W m^{-2}; ϵ_{wi} = 0.8; ϵ_{we} = 0.7; T_{LR} = 450 K; T_F = 843 K; T_O = 746 K; λ_w = 8.41 x 10^{-3} K m^2 W^{-1}; ΔH_R const. A = -5573 kJ mol^{-1}; $\langle V_{ZO} \rangle$ = 1.493 m s^{-1})

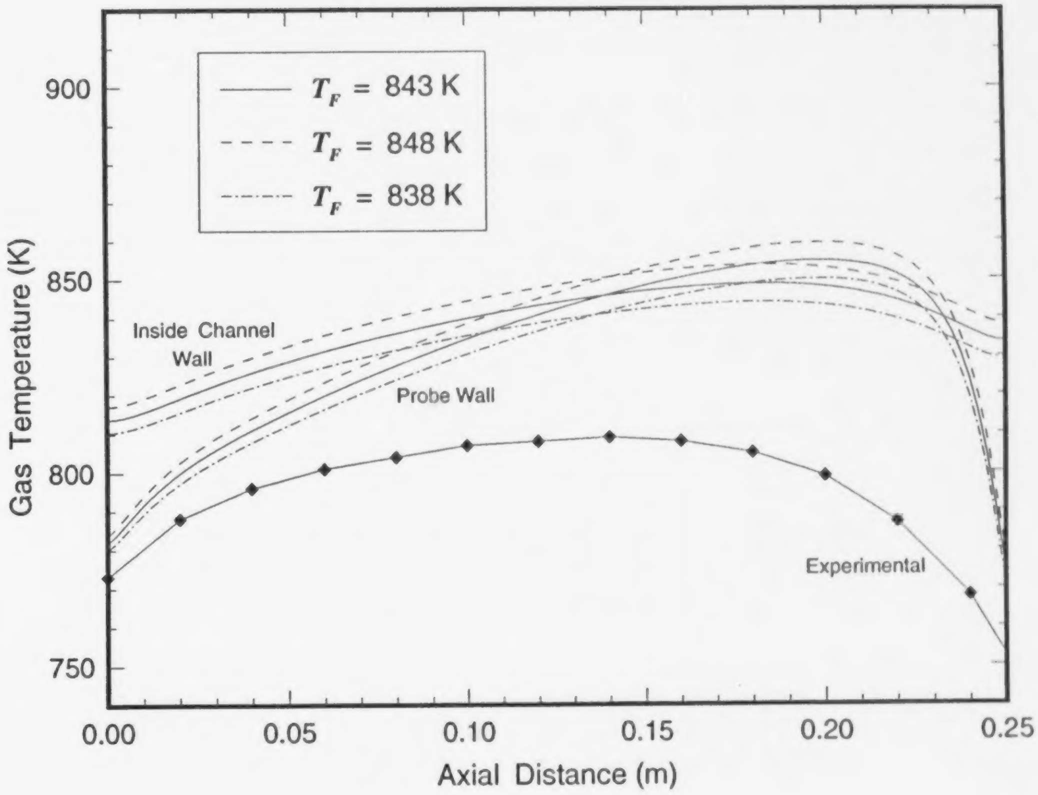

Model 009 (pcb1 (5, 1a); annular velocity profile; 1654 elements; T_O = 746 K; T_{LR} = 450 K; ibou = 4; $T_{refl} = T_O$; $T_{re\Omega}$ = 450 K; h_{eff} = 440 W m^{-2}; ϵ_{wi} = 0.8)

Figure 4-14. Sensitivity analysis : variation in furnace temperature.

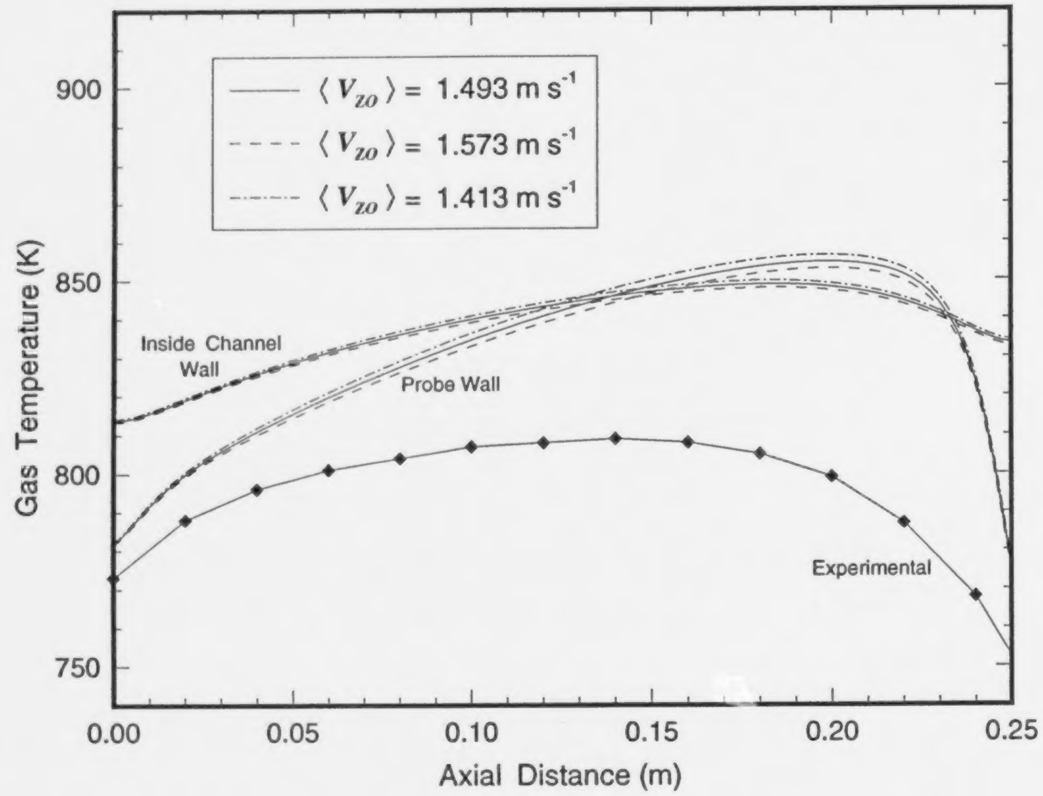

Model 009 (pcb1 (5, 1a); annular velocity profile; 1654 elements; $T_O = 746$ K; $T_{LR} = 450$ K; ibou = 4; $T_{refl} = T_O$; $T_{ref2} = 450$ K; $h_{eff} = 440$ W m^{-2}; $\epsilon_{wi} = 0.8$)

Figure 4-15. Sensitivity analysis : variation in average inlet velocity.

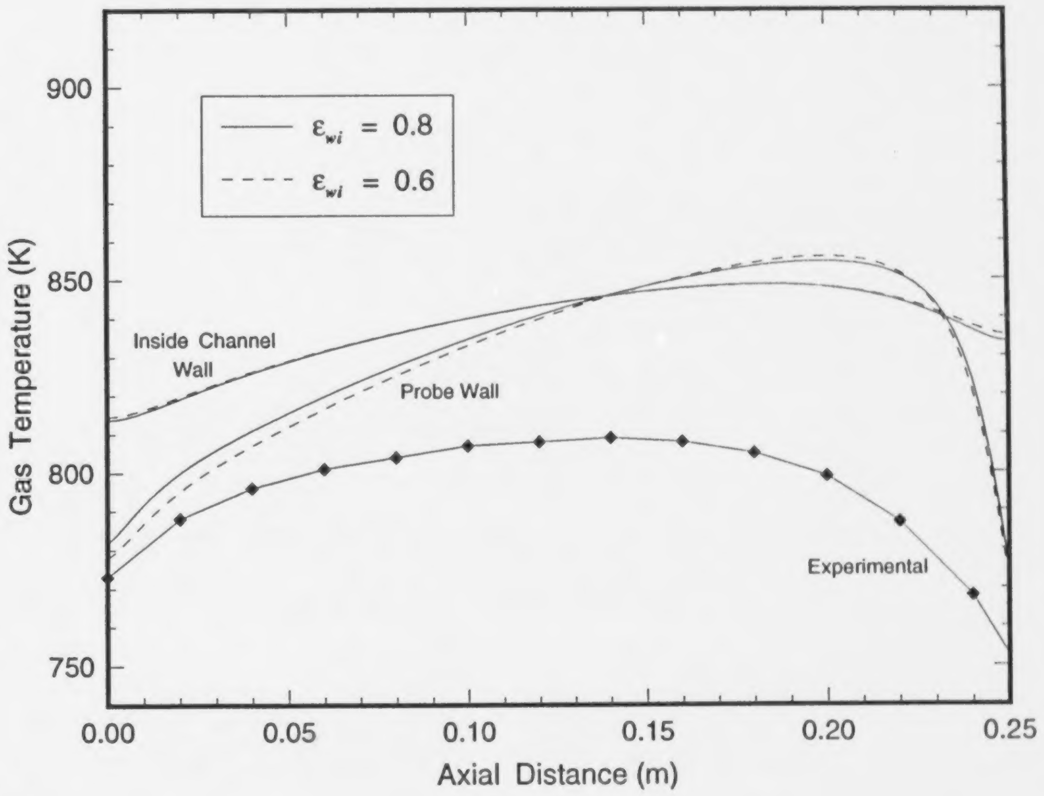

Model 009 (pcb1 (5, 1a); annular velocity profile; 1654 elements; T_o = 746 K; T_{LR} = 450 K; ibou = 4; T_{refl} = T_O; T_{ref2} = 450 K; h_{eff} = 440 W m^{-2})

Figure 4-16(a). Sensitivity analysis : variation in internal wall emissivity value.

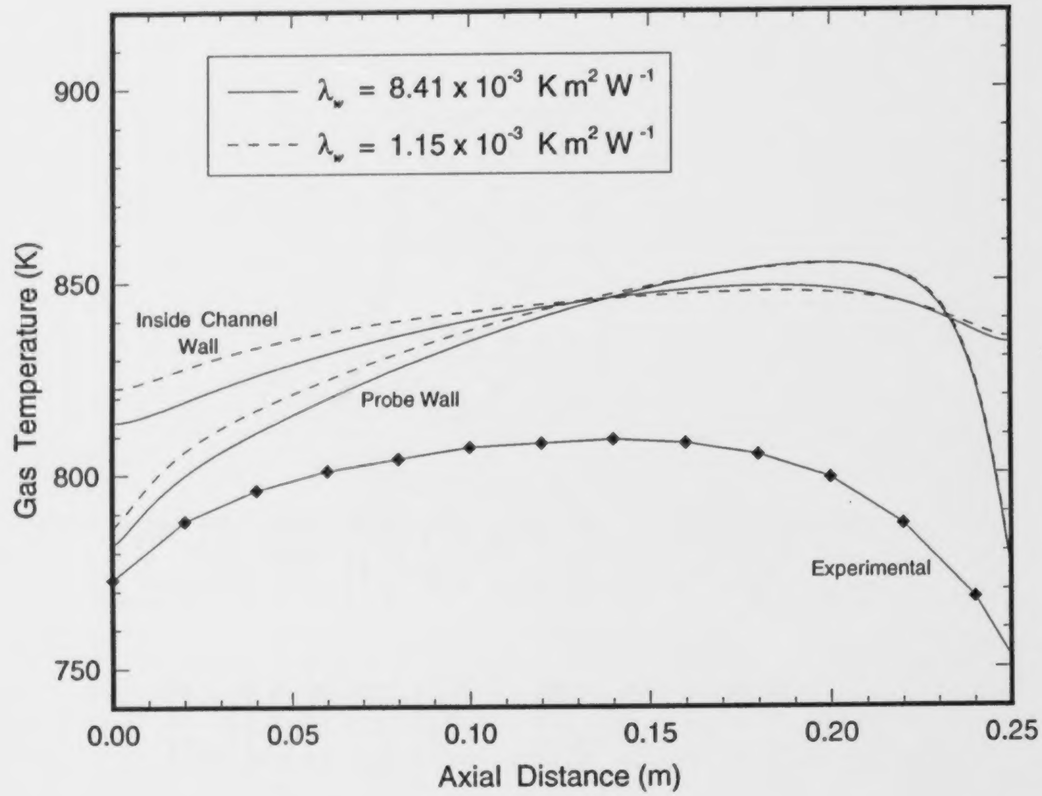

Model 009 (pcb1 (5, 1a); annular velocity profile; 1654 elements; T_O = 746 K; T_{LR} = 450 K; ibou = 4; T_{refl} = T_O; T_{refl2} = 450 K; h_{eff} = 440 W m^{-2}; ϵ_{wi} = 0.8)

Figure 4-16(b). Sensitivity analysis : variation in radial wall conduction resistance.

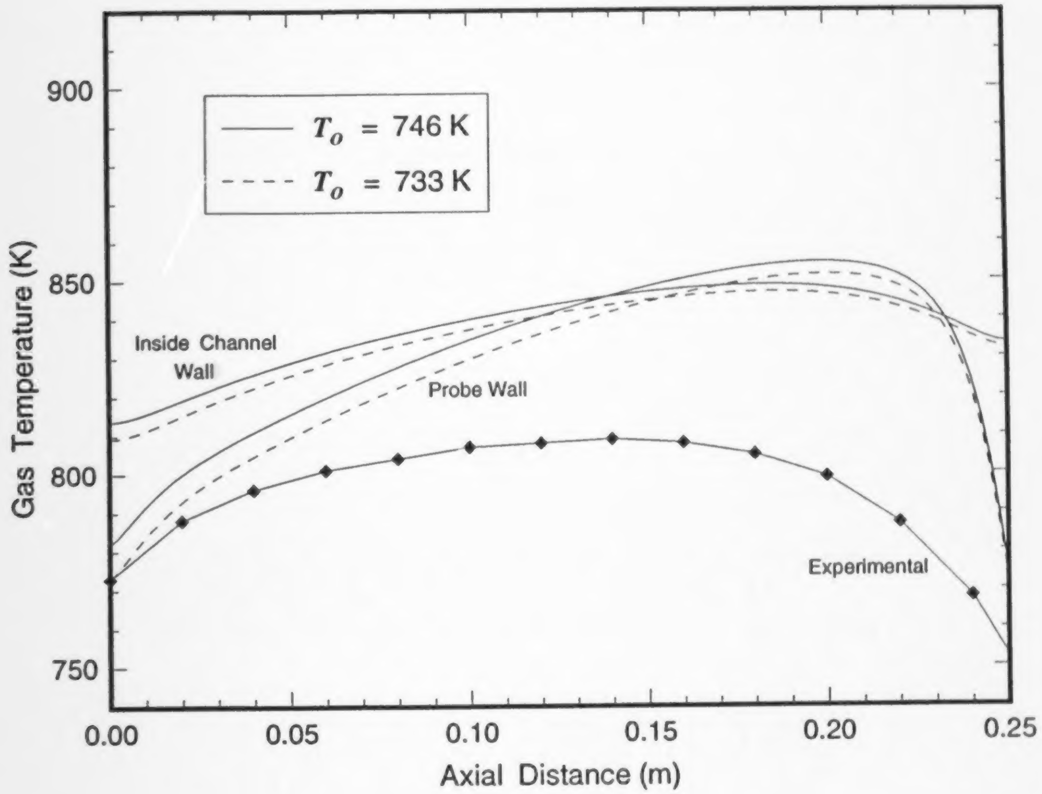

Model 009 (pcb1 (5, 1a); annular velocity profile; 1654 elements; T_{LR} = 450 K; ibou = 4; T_{refl} = T_O; T_{ref2} = 450 K; h_{eff} = 440 W m^{-2}; ϵ_{wt} = 0.8)

Figure 4-17. Sensitivity analysis : variation in average inlet gas temperature.

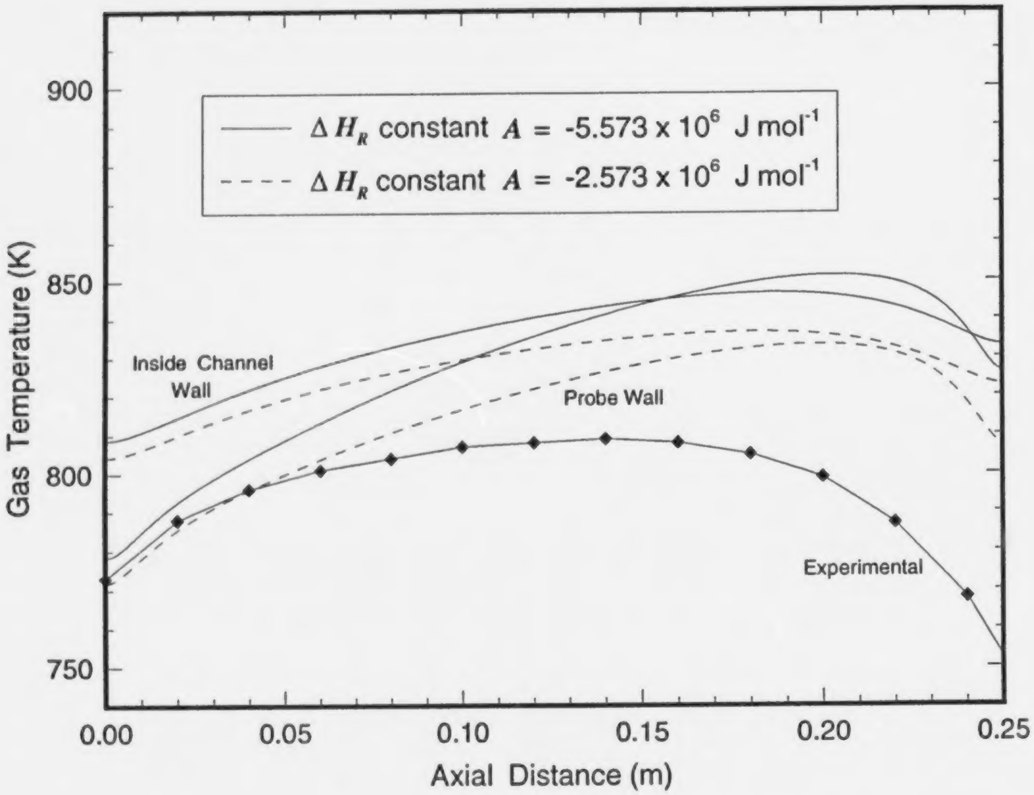

Model 009 (pcb1 (5, 1a); annular velocity profile; 1654 elements; T_O = 733 K T_{LR} = 450 K; ibou = 4; T_{refl} = T_O; T_{ref2} = 450 K; h_{eff} = 440 W m^{-2}; ϵ_{wi} = 0.8)

Figure 4-18. Sensitivity analysis : variation in the heat of reaction for PCB.

From Figure 4-12 it is apparent that the simulated probe wall temperature profile is still considerably higher than the measured thermocouple profile. However, it was found, that by reducing the heat of reaction ΔH_R in the model it was possible to reduce the discrepancy between the measured and simulated profiles, see Figure 4-18. The constant A in the fourth order temperature polynomial for ΔH_R (see Appendix A.2) was altered. An explanation for a reduction in the heat of reaction is the incomplete combustion of PCB in the uncoated channel experiments. For example, if the PCB molecule only cracked into two chlorobenzene molecules, the heat of complete combustion of chlorobenzene is -2991 kJ mol^{-1} while for the PCB it is -5558 kJ mol^{-1}. Since the experimental HPLC analysis only recorded the concentration of PCB at the reactor exit and not the concentration of HCl or CO_2 it is difficult to estimate the extent of complete combustion. This point will be addressed again in Section 4B.4.

4A.7 Verification of the Homogeneous Kinetics

The homogeneous kinetics were originally derived using a basic reactor model; empty tube velocity profile and no internal radiation or wall conduction (Model 068). It was now necessary to check if this kinetic expression is still valid if the complete reactor model is used. Model 009 was used to simulate the 9 experimental runs with the homogeneous kinetic expression given in Equation (4-5). As before ΣR^2 was calculated and then these results were compared with the previous evaluation of the kinetics, see Table 4-6. Comparing the two values of ΣR^2 it can be seen that the homogeneous kinetics are still valid after including all the phenomena in the reactor model. Even though the presence of internal radiation, wall conduction and an annular velocity profile has been shown to influence the wall temperature profiles significantly, the average outlet gas temperature and conversion are only slightly altered. Note the inlet gas temperatures T_O used for the Model 009 simulations are 20 - 30 K lower than the measured inlet probe temperatures that were used in Model 068 (see Table 2-3 and 2-4). This was performed so that Model 009 gave a better match between the simulated and experimental probe wall temperature profiles, see Figures 4-19(a) to 4-19(c).

Table 4-6. Verification of the homogeneous kinetics

Homogeneous Kinetics: E_H = 38,010 J mol^{-1}; A_H = 473 s^{-1}					
Experiment number	Y_{pcbL} Outlet mole fraction (x 10^6)			T_O Average inlet gas temperature used (K)	
	Exp.	Model 068*	Model 009†	Model 068*	Model 009†
pcb1 (5, 1a)	2926	2782	2822	746	733
pcb2 (5, 1b)	3289	3184	3247	755	740
pcb3 (5, 1e)	4294	4643	4787	749	734
pcb4 (5, 1c)	3830	4147	4289	753	733
pcb5 (5, 1d)	4678	4397	4564	753	733
pcb6 (10, 2b)	3977	3555	3699	798	778
pcb7 (10, 2c)	2761	2896	3069	902	882
pcb8 (10, 2d)	2547	2743	2892	903	883
pcb9 (10, 2e)	2246	1954	2159	1055	1025
ΣR^2 Residual square error		0.057	0.066		

* Model 068 (empty tube velocity profile; correct inlet average velocity; coarse mesh; 924 elements)

† Model 009 (annular velocity profile; uniform mesh; 1654 elements; T_{LR} = 450 K; ibou = 4; T_{refl} = T_O; T_{ref2} = 450 K; h_{eff} = 440 W m^{-2})

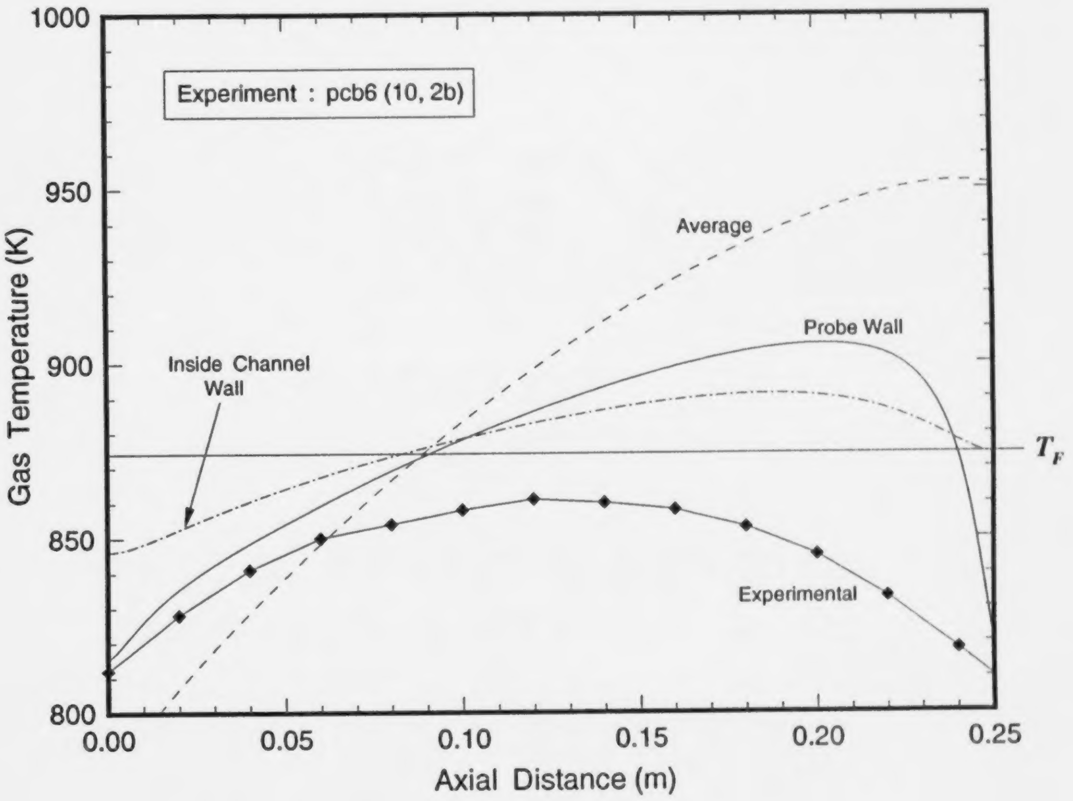

Model 009 (pcb6 (10, 2b); annular velocity profile; 1654 elements; T_{LR} = 450 K; T_O = 778 K; ibou = 4; T_{refl} = T_O; T_{ref2} = 450 K; h_{eff} = 440 W m^{-2})

Figure 4-19(a). Axial temperature profile with complete model.

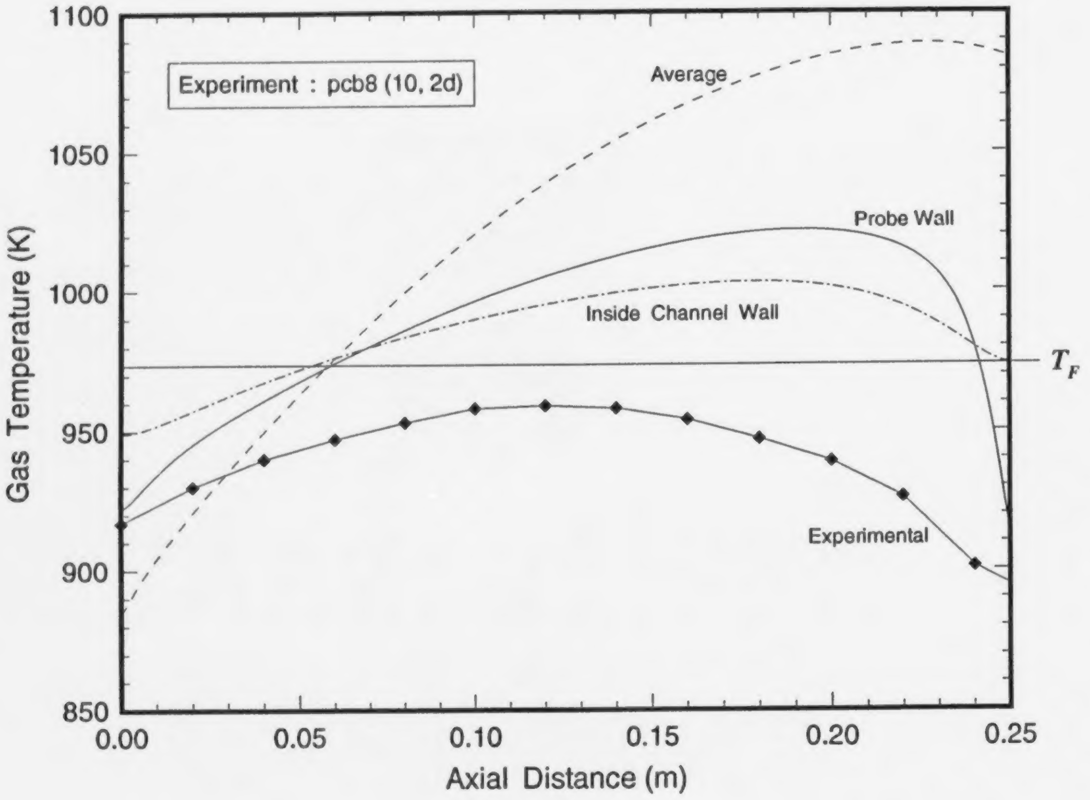

Model 009 (pcb8 (10, 2d); annular velocity profile; 1654 elements; T_{LR} = 450 K; T_O = 883 K; ibou = 4; T_{ref1} = T_O; T_{ref2} = 450 K; h_{eff} = 440 W m^{-2})

Figure 4-19(b). Axial temperature profile with complete model.

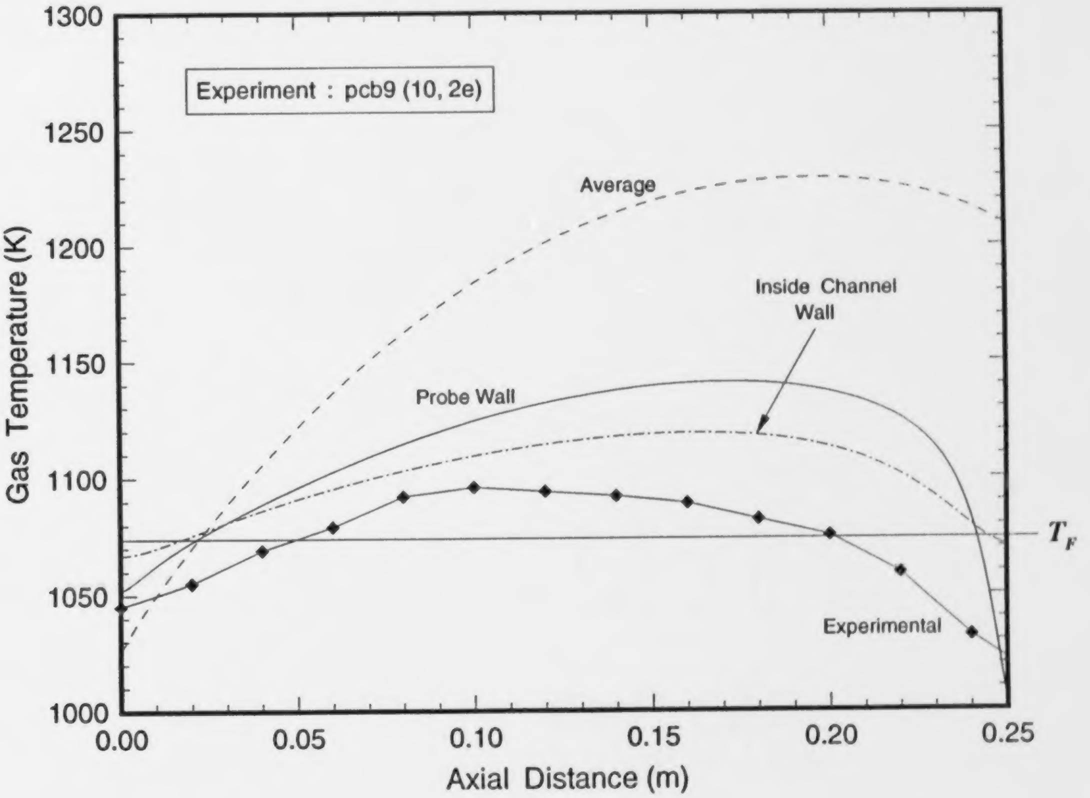

Model 009 (pcb9 (10, 2e); annular velocity profile; 1654 elements; T_{LR} = 450 K; T_O = 1025 K; ibou = 4; T_{refl} = T_O; T_{ref2} = 450 K; h_{eff} = 440 W m^{-2})

Figure 4-19(c). Axial temperature profile with complete model.

4B : CATALYST COATED CHANNEL EXPERIMENTS

4B.1 Preliminary Observations on Catalytic Reaction

The results described in Section 4A were obtained with a rate of catalytic reaction equal to zero ($R_W = 0$) as the uncoated channel experiments were being simulated. The second set of experiments were carried out with a channel coated with chromia catalyst *ie* the contributions of both homogeneous and catalytic reaction must now be included in the model. From Section 3.3, the catalytic reaction at the channel wall was assumed to be first order dependent:

$$R_W = A_W \exp\left[-\frac{E_W}{R_g T} \right] \frac{P\, Y_{pcb}}{R_g T} \qquad \textbf{(4-10)}$$

The next stage of this study was to determine the rate constants A_W and E_W for the catalytic reaction by simulating the experimental data given in Tables 2-5(a) and 2-5(b).

The homogeneous rate expression R_H given in Equation (4-5) was assumed to be valid for the catalytic experiments and was used in the reactor model for subsequent simulation work. Initially, a temperature independent catalytic rate constant k_W was employed in the model, effectively setting the activation energy E_W equal to zero. Using the experimental data recorded for the 24 cm length channel, the effects of including catalytic reaction were studied by changing the value of k_W. The contour plots given in Figures 4-20 and 4-21 show the temperature and concentration profiles simulated with the same experimental conditions with and without catalytic wall reaction. Note that the aspect ratio of the reactor has been altered in the plot for visual purposes. The aspect ratio should be 36 : 1 as the experimental channel has a length of 24 cm length and an inside radius of 0.67 cm. These results were obtained using Model 079 with an annular velocity profile and a uniform finite element mesh.

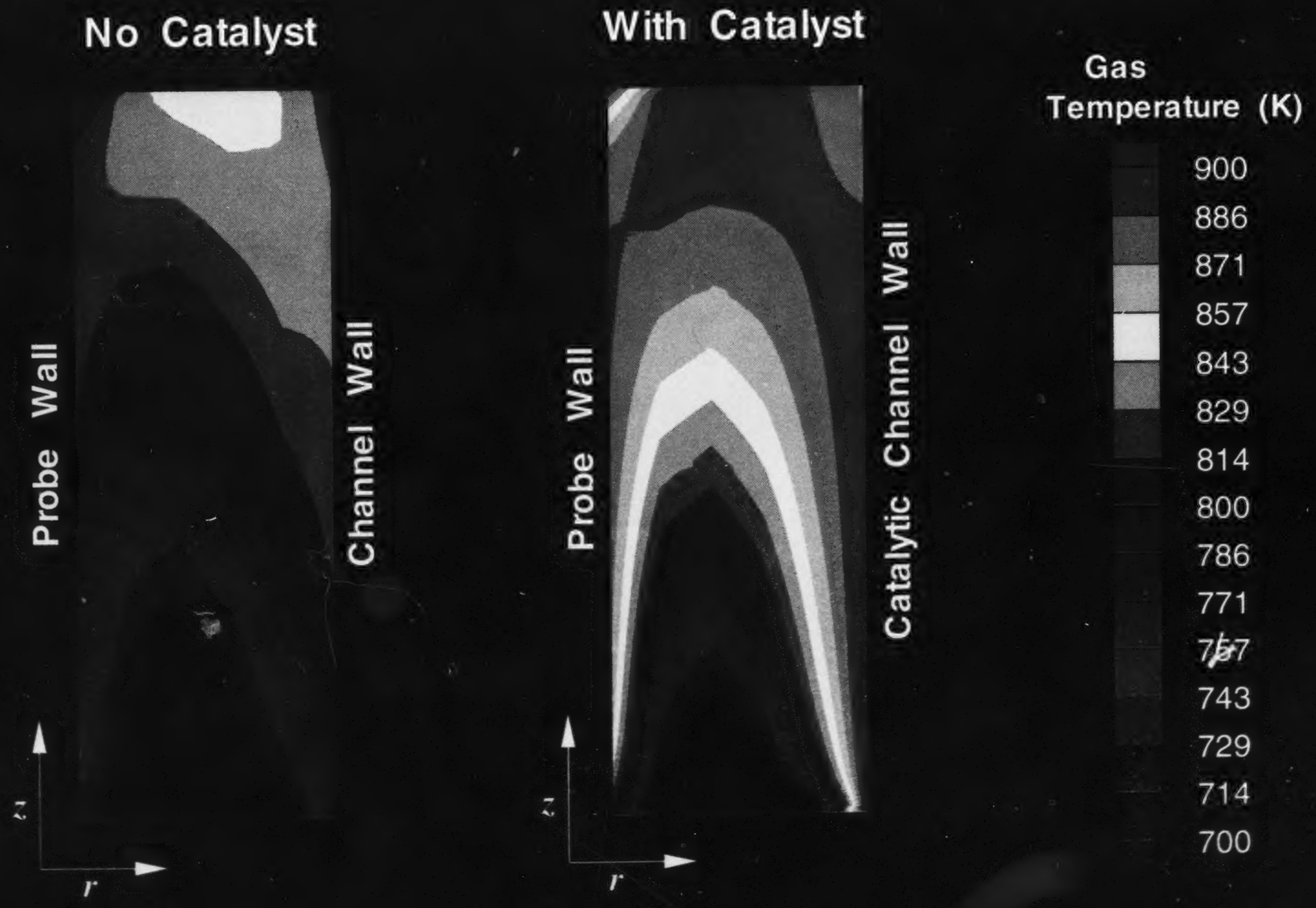

Figure 4-20. Comparison temperature profiles.

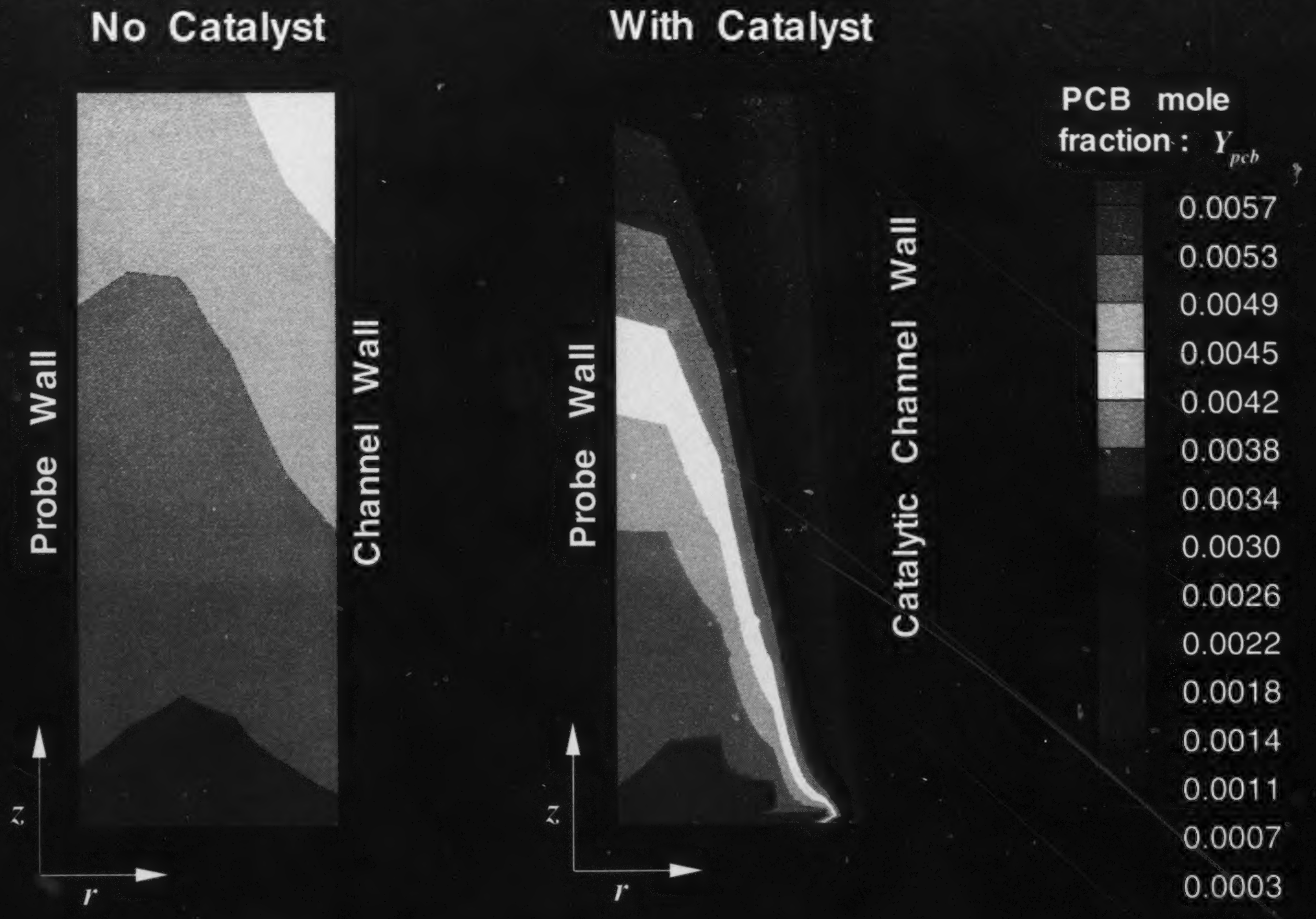

Figure 4-21. Comparison concentration profiles.

From the contour plots the following phenomena can be observed:

i) The temperatures in the catalytic coated channel are higher than in the uncoated channel. The difference in temperature is particularly pronounced in the region close to the channel wall where the catalytic reaction immediately takes off.

ii) The radiation from the probe and channel wall out the end of the channel causes a corresponding drop-off in wall temperature near the outlet.

iii) The conversion of PCB is substantially higher in the catalytic coated channel than in the uncoated channel. It is also apparent, for the coated channel the catalytic reaction takes off immediately hence the concentration of PCB in the region close to the channel wall is very low.

It was evident from the above analysis that the catalytic reaction is limited by the rate of diffusion of the PCB to the coated channel wall, as is clearly shown in the radial concentration plot, given as Figure 4-22. An example of the simulation results obtained for one of the experimental runs is given in Table 4-7. Even with a temperature dependent catalytic rate expression ($E_W \neq 0$) the model was found to under-predict all the experimental outlet conversions by 20 - 30 %.

4B.2 Model Analysis

Figures 4-23(a) to 4-23(f) shows the simulated temperature profiles for an experimental run as the model type is changed from a basic Model 069 to the complete Model 009. The consequence of including different phenomena in the reactor model is apparent, particularly if the channel and probe wall profiles are compared.

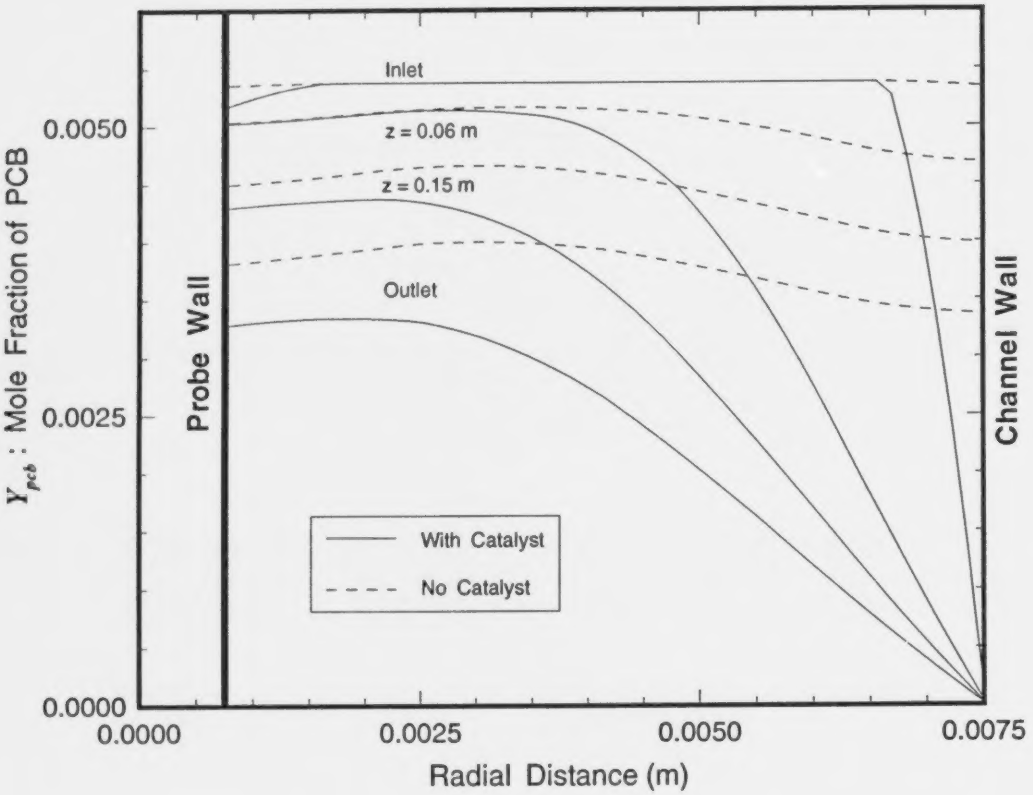

Model 069 (cat4 (4a); $A_H = 473\ s^{-1}$, $E_H = 38{,}010\ J\ mol^{-1}$; annular velocity profile; 1594 elements)

Figure 4-22. Radial concentration profile for catalytic reaction.

Table 4-7. Simulated conversions with different catalytic rate expressions

Experiment Number	cat4 (4a)
Channel Length	24 cm
Experimental Y_{pcbL}	1381×10^{-6}
Model Y_{pcbL} using : $k_W = 2$ m s^{-1}	2246×10^{-6}
Model Y_{pcbL} using : $k_W = 200$ m s^{-1}	2241×10^{-6}
Model Y_{pcbL} using* : $A_W = 3.25 \times 10^5$ m s^{-1} $E_W = 8.979 \times 10^4$ J mol^{-1}	2285×10^{-6}

Model 069 ($A_H = 473$ s^{-1}, $E_H = 38{,}010$ J mol^{-1}; annular velocity profile; uniform mesh; 1594 elements)

* This rate expression gives a rate constant of $k_W = 2$ m s^{-1}, at the simulated midpoint temperature $T_{L/2} = 900$ K.

Recall from Section 3.2, the molecular diffusion coefficient D for PCB in air was calculated using the following relation:

$$D = D_k \frac{T^{1.75}}{P} \tag{4-11}$$

where P has units of Pa, T is in K and $D_k = 2.532 \times 10^{-5}$ Pa m^2 K$^{-1.75}$ s^{-1} to give D in m^2 s^{-1}. The shown simulation results were obtained with the original and an increased value of D_k in Equation (4-11). The D_k constant was increased from 2.532×10^{-5} to 5.525×10^{-5} Pa m^2 K$^{-1.75}$ s^{-1} to give a better agreement between the experimental and simulated conversions. The validation of this procedure is explained in the next section. The inlet temperature T_O used in the model was also reduced to give a better agreement between the measured and simulated probe wall profile.

Typical radial temperature profiles with catalytic reaction present are shown in Figure 4-24(a). The corresponding internal radiation flux plot for the channel and probe wall is shown in Figure 4-24(b). This shows the complexity of the radiation interactions. Typical Nu and Sh number plots are also given in Figures 4-24(c) and 4-24(d).

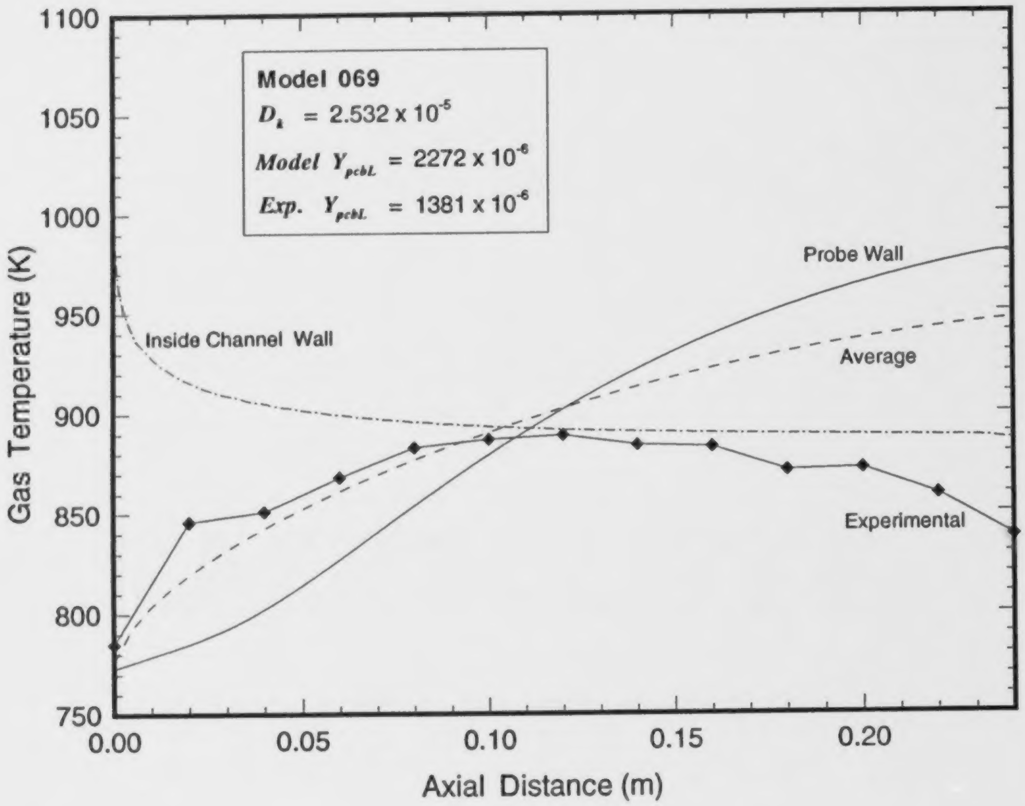

Model 069 (cat4 (4a); k_W = 2 m s^{-1}; annular velocity profile; 1594 elements; T_O = 773 K)

Figure 4-23(a). Temperature profiles : consequence of model type.

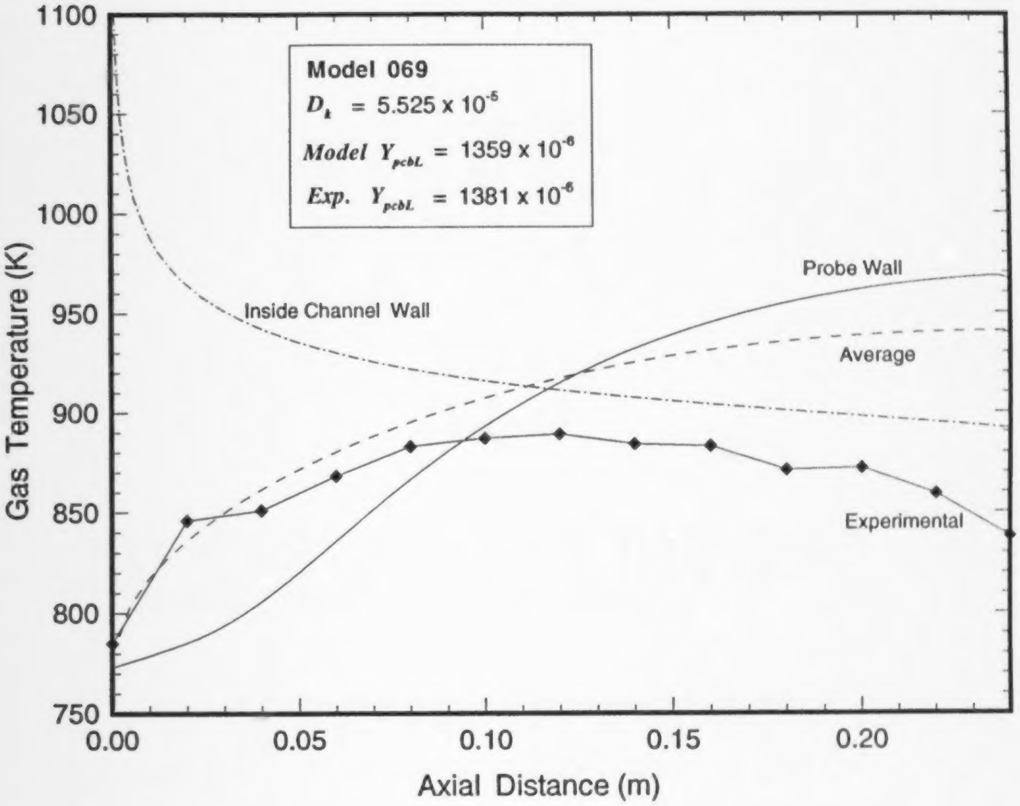

Model 069 (cat4 (4a); k_w = 2 m s^{-1}; annular velocity profile; 1594 elements; T_o = 773 K)

Figure 4-23(b). Temperature profiles : consequence of model type.

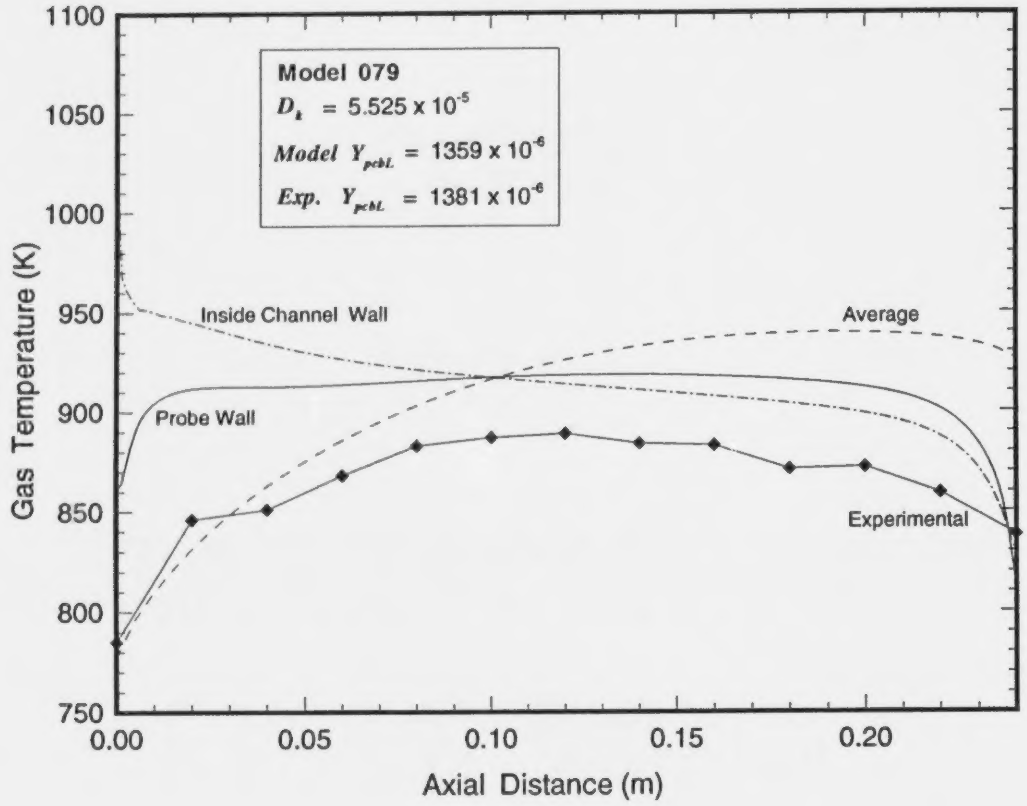

Model 079 (cat4 (4a); k_W = 2 m s^{-1}; annular velocity profile; 1594 elements; T_O = 773 K; T_{LR} = 450 K; ϵ_{wi} = 0.8)

Figure 4-23(c). Temperature profiles : consequence of model type.

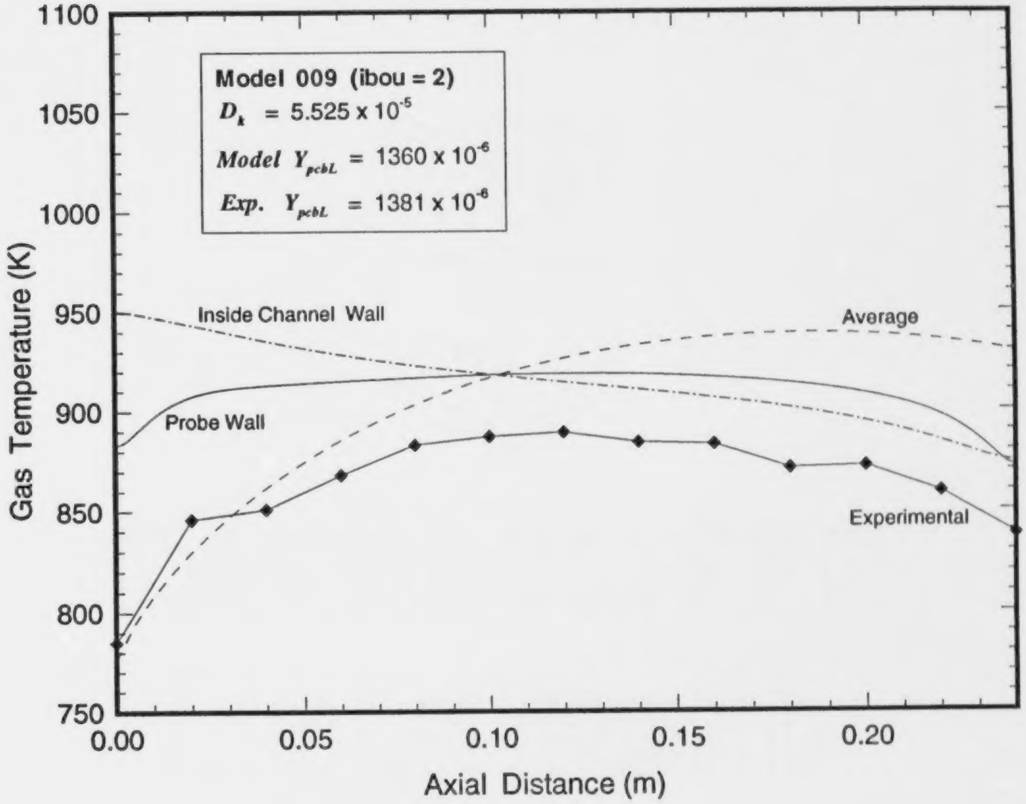

Model 009 (cat4 (4a); k_W = 2 m s^{-1}; annular velocity profile; 1594 elements; T_{LR} = 450 K; ϵ_{wi} = 0.8; T_O = 773 K; ibou = 2)

Figure 4-23(d). Temperature profiles : consequence of model type.

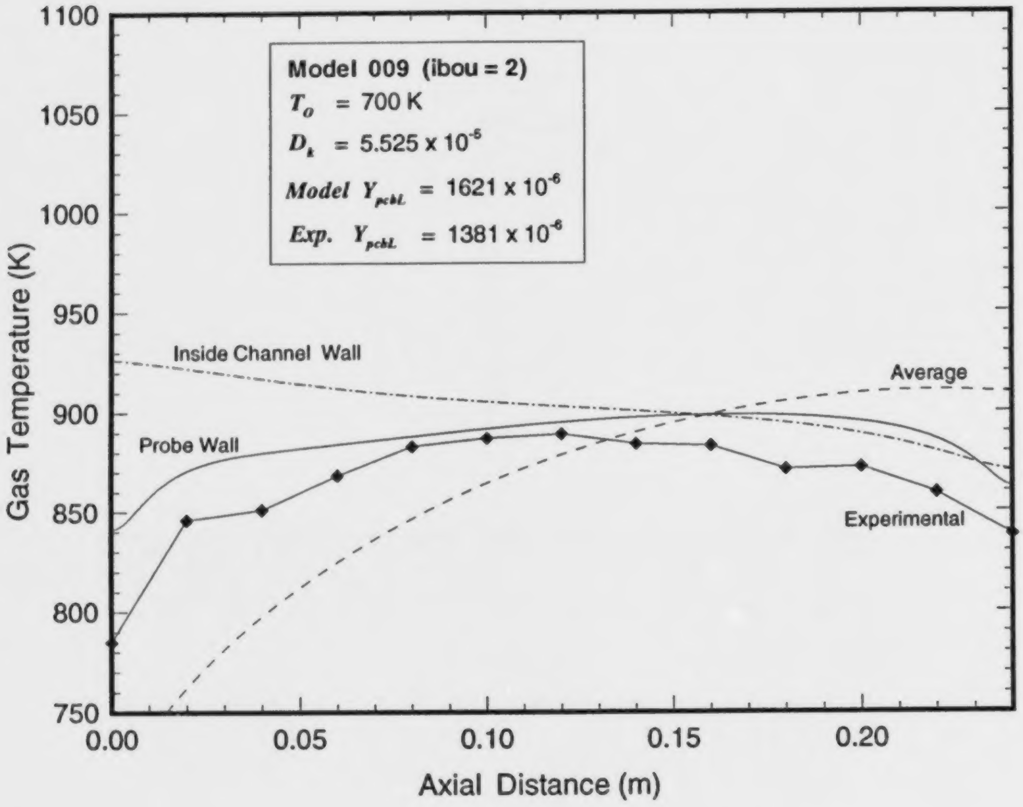

Model 009 (cat4 (4a); $k_W = 2$ m s^{-1}; annular velocity profile; 1594 elements; $T_{LR} = 450$ K; $\epsilon_{wi} = 0.8$; $T_O = 700$ K; ibou = 2)

Figure 4-23(e). Temperature profiles : consequence of model type.

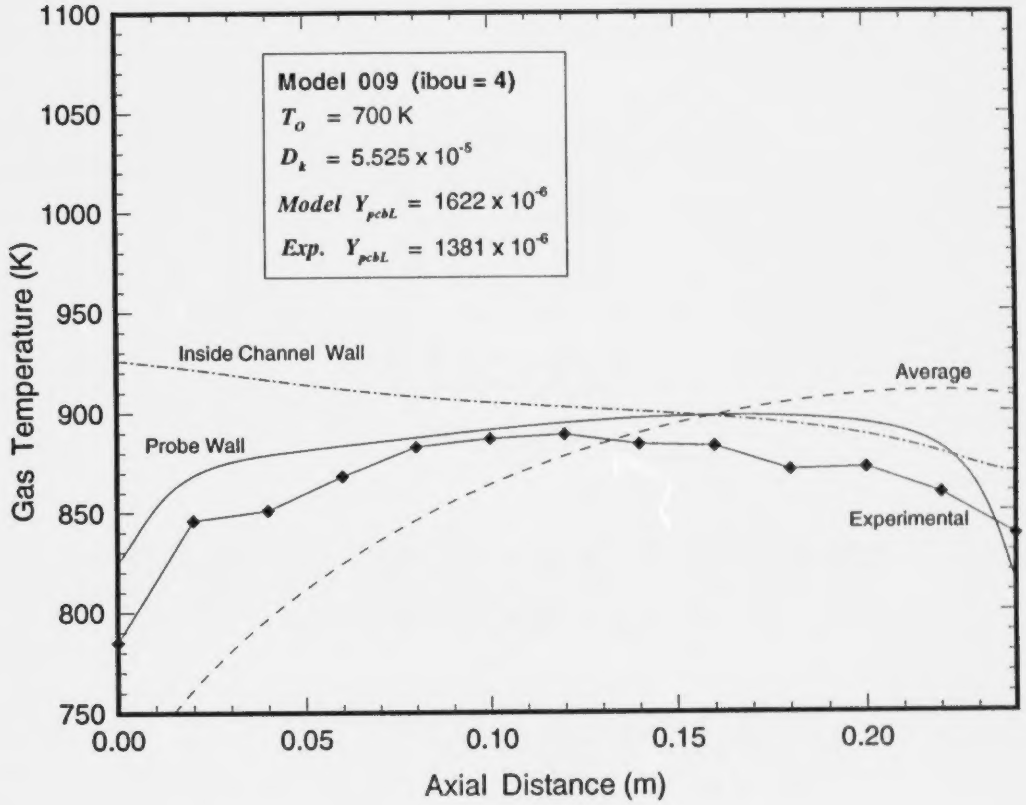

Model 009 (cat4 (4a); k_W = 2 m s^{-1}; annular velocity profile; 1594 elements; T_{LR} = 450 K; ϵ_{wi} = 0.8; T_O = 700 K; ibou = 4; T_{refl} = T_O; T_{refl2} = 450 K; h_{eff} = 440 W m^{-2})

Figure 4-23(f). Temperature profiles : consequence of model type.

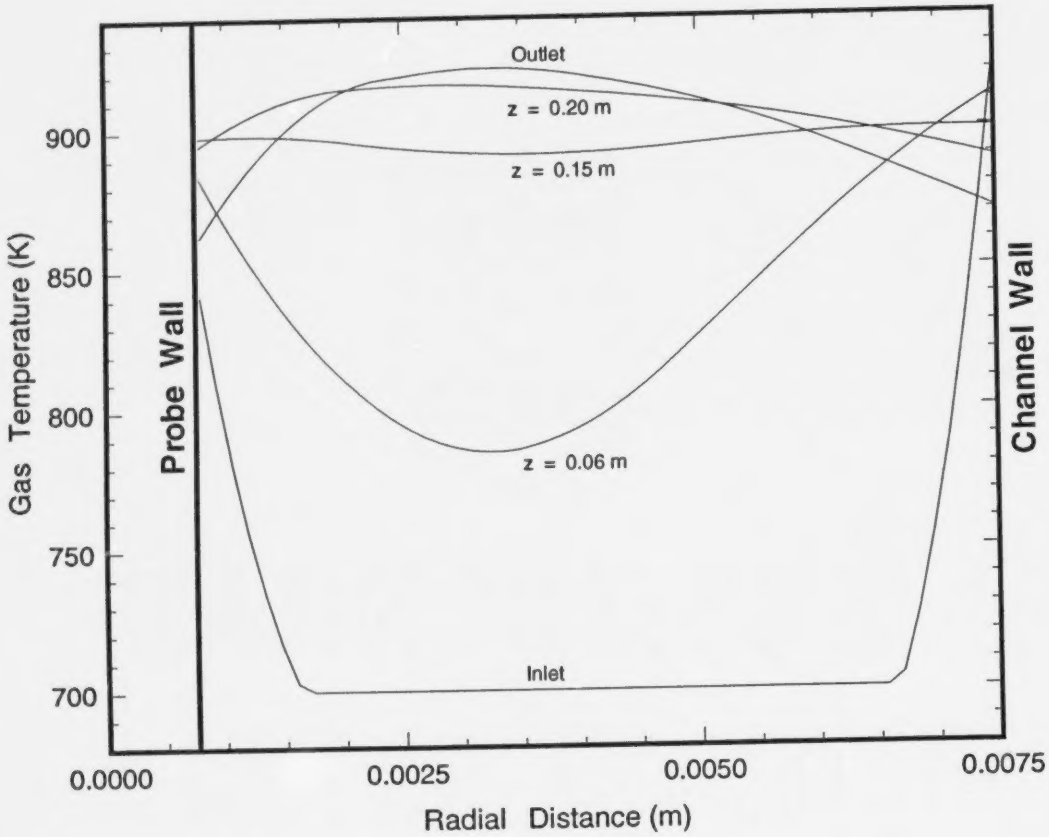

Model 079 (cat4 (4a); k_w = 2 m s^{-1}; annular velocity profile; 1594 elements; T_{LR} = 450 K; ϵ_{wi} = 0.8)

Figure 4-24(a) Radial temperature profile with catalytic reaction.

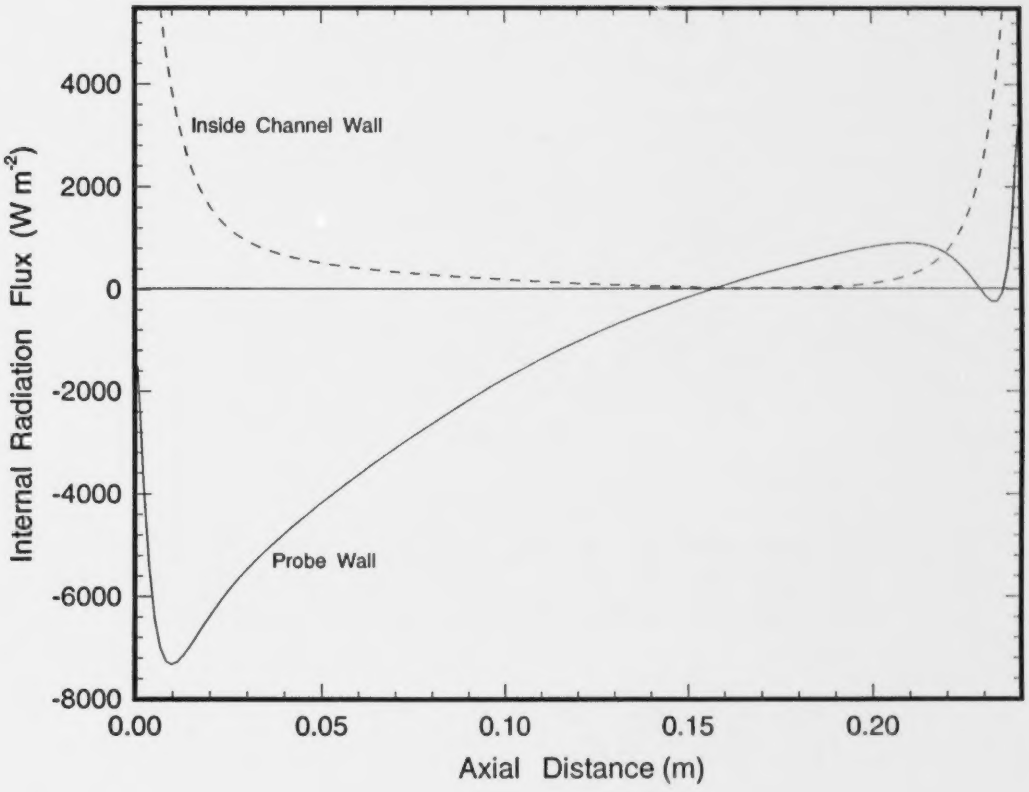

Model 079 (cat4 (4a); k_W = 2 m s^{-1}; annular velocity profile; 1594 elements; T_{LR} = 450 K; ϵ_{wi} = 0.8)

Figure 4-24(b) Internal radiation flux plot with catalytic reaction.

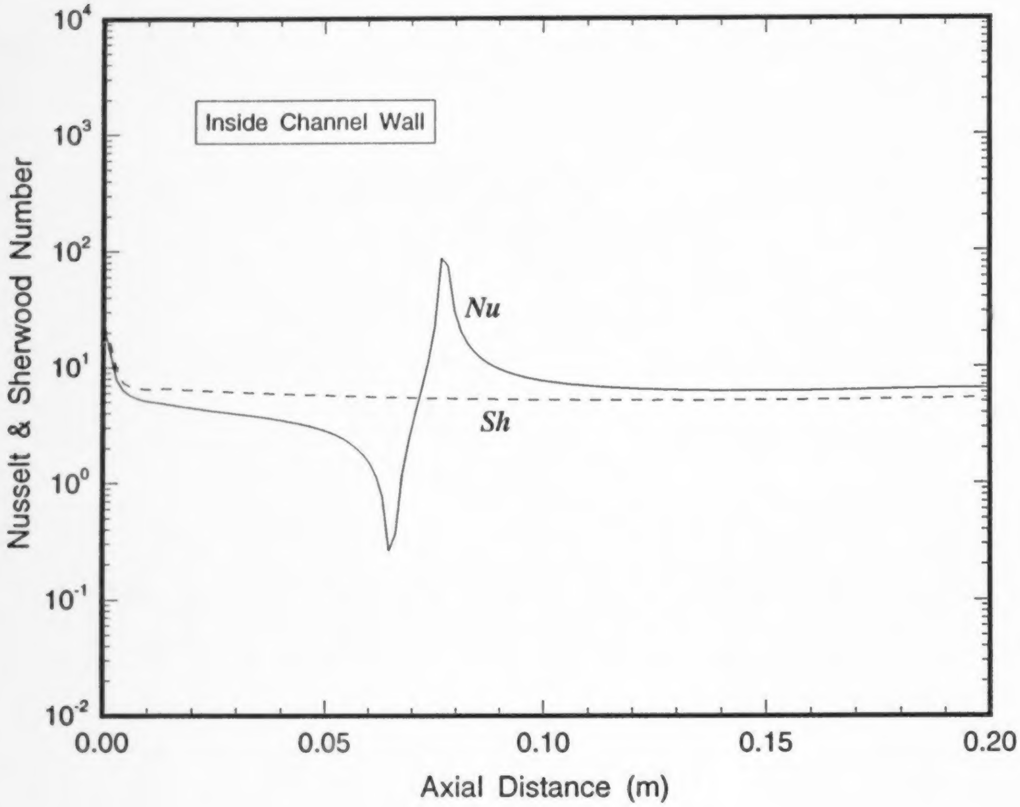

Model 079 (cat4 (4a); $k_W = 2\ \mathrm{m\ s^{-1}}$; annular velocity profile; 1594 elements; $T_{LR} = 450$ K; $\epsilon_{wt} = 0.8$)

Figure 4-24(c) *Sh* and *Nu* number plot with catalytic reaction : Channel wall.

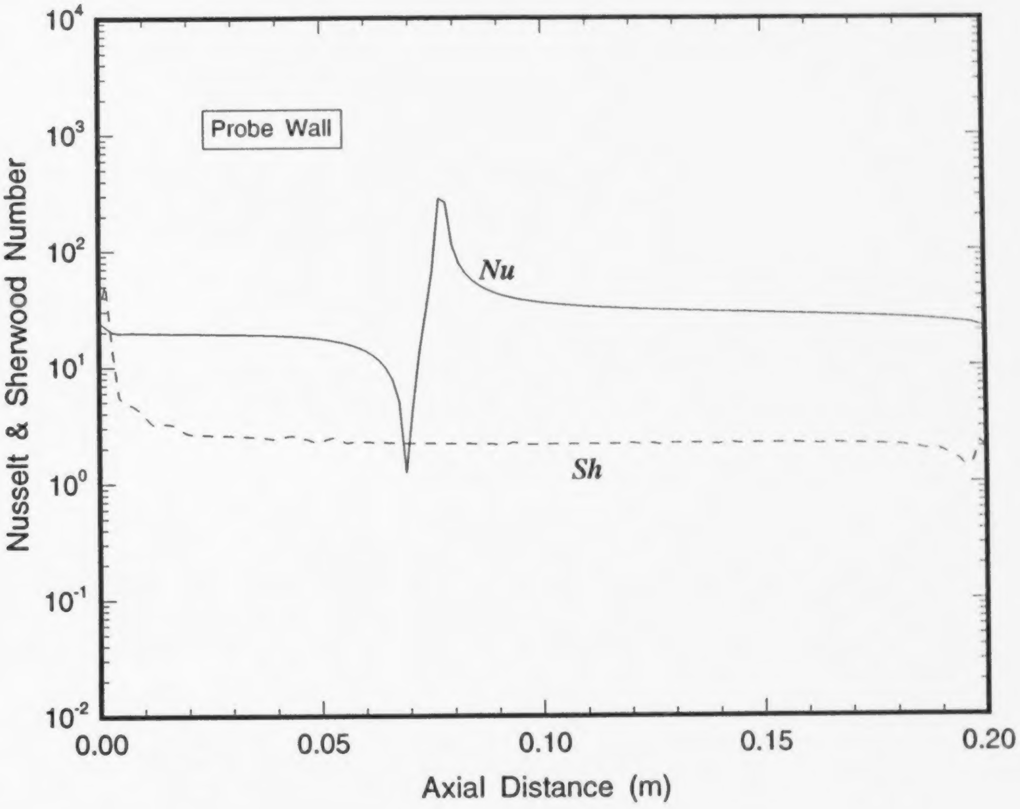

Model 079 (cat4 (4a); $k_W = 2$ m s^{-1}; annular velocity profile; 1594 elements; $T_{LR} = 450$ K; $\epsilon_{wi} = 0.8$)

Figure 4-24(d) *Sh* and *Nu* number plot with catalytic reaction : Probe wall.

4B.3 Diffusion Limited Catalytic Reaction

As stated in the previous sections, the rate of catalytic reaction was found to be limited by the rate of diffusion of the PCB to the coated channel wall. This seems a reasonable conclusion since the residence time of the gas in the channel is less than 0.25 sec and the channel diameter is large. Diffusion limitation is not an uncommon phenomenon for catalytic monolith reactors and has been reported in several studies [59,60]. This means that it was impossible to determine a catalytic rate expression since the conversion of PCB is independent of the catalytic reaction rate. In the subsequent simulation work the following arbitrary temperature independent expression was used for the rate of catalytic reaction:

$$R_W = 2.0 \ \mathrm{mol\ m^{-2}\ s^{-1}}$$

However, even though the catalytic reaction is diffusion limited the reactor model still under predicted the outlet experimental conversions. To explain the observed discrepancy in conversion the following hypotheses were made :

i) Developing laminar flow is a significant factor in the coated channel experiments. The developing profile may cause an increase in the transfer of PCB to the catalytic surface over the developing length L_D.

ii) The molecular diffusion coefficient for the PCB is effectively increased by
   - turbulence in the reactor channel caused by upstream disturbances.
   - radial convection due to the hot gas layer near the channel wall.

The first hypothesis was tested by including developing flow in the reactor model. At the experimental conditions the developing length was about $L_D \approx 9$ cm. Although this is a significant fraction of the overall channel lengths, developing flow was shown to increase only slightly the simulated PCB conversion, as illustrated by the results given in Table 4-8. Hence developing flow does not account for the observed discrepancy in conversion.

Table 4-8. The effect of developing flow on the catalytic reaction

Experiment Number	cat4 (4a)
Channel Length	24 cm
Experimental Y_{pcbL}	1381 x 10^{-6}
Model Y_{pcbL} : Fully Developed Flow *	2246 x 10^{-6}
Model Y_{pcbL} : Developing Flow †	2216 x 10^{-6}

* Model 069 ($A_W = 2$ m s^{-1}, $E_W = 0$; annular velocity profile; uniform mesh; 1594 elements)
† Model 169 ($A_W = 2$ m s^{-1}, ...)

The second hypothesis was that an effective increase in the diffusion of PCB in the experimental reactor accounts for the discrepancy. Recall from the previous section, that an increased D_k constant in the reactor model gave a better agreement between the experimental and simulated conversions. To test this hypothesis further, the D_k constant in Equation (4-11) was increased for the four experimental runs given in Table 2-5(b) since the experimental and predicted axial temperature profiles along the thermocouple probe could also be compared. It was found that by increasing the D_k value from 2.532 x 10^{-5} to a value of 7.025 x 10^{-5}, the simulated conversions were much closer to the experimental values. Table 4-9 gives the results obtained using this increased D_k value in Model 009 (complete model; fully developed flow) and Model 109 (complete model; developing flow). Again, developing flow is shown to increase slightly the outlet conversion of PCB.

However, it must be remembered that the homogeneous kinetics given as Equation (4-5) were derived with the original molecular diffusion equation *ie* $D_k = 2.532 \times 10^{-5}$ Pa m^2 K$^{-1.75}$ s^{-1}. In testing the second hypothesis it was necessary to determine if the homogeneous reaction is effected by an increase in diffusion in the channel. Two of the homogeneous experimental runs were tested using a model with only homogeneous reaction and an increased D_k value. From Table 4-10 it is apparent that the homogeneous reaction is not significantly effected by diffusion and so the kinetics are still valid. This is expected since the Reynolds number in this study is about 270, high enough to cause axial diffusion to be insignificant and since the radial concentration profiles for the uncoated experiments are also fairly flat (see Figure 4-22) radial diffusion will be insignificant.

Table 4-9. Results using an increased D_k value

Catalytic Kinetics: D_k = 7.025 x 10^{-5} Pa m^2 K$^{-1.75}$ s^{-1}; A_w = 2.0 m s^{-1}; E_W = 0						
Experiment No. / Channel Length (cm)	Experimental		Model 009 (Fully Developed)		Model 109 (Developing Flow)	
	Y_{pcbL} (x 10^6)	T_L (K)*	Y_{pcbL} (x 10^6)	T_L (K)†	Y_{pcbL} (x 10^6)	T_L (K)†
3d / L = 31	1220	774	1057	895	1014	895
4a / L = 24	1381	816	1380	900	1339	901
5f / L = 20	1650	844	1695	893	1648	895
6a / L = 15	1709	865	2187	876	2131	879

Model *09 (annular velocity profile; uniform mesh; number of elements 2054 (3d), 1594 (4a), 1324 (5f), 994 (6a); T_O = 675 K (4a, 5f, 6a) 645 K (3d); T_{LR} = 450 K; ibou = 4; $T_{ref1} = T_O$; T_{ref2} = 500 K; h_{eff} = 367 W m^{-2})

* Experimentally measured outlet temperature using the thermocouple probe.

† Radial average outlet temperature calculated by reactor model.

Table 4-10. Effect of molecular diffusion on homogeneous combustion

Homogeneous Kinetics: $A_H = 473\ \mathrm{s}^{-1}$; $E_H = 38{,}010\ \mathrm{J\ mol}^{-1}$				
Experiment Number	Model 009 with $D_k = 2.532 \times 10^{-5}$ ($\mathrm{Pa\ m^2\ K^{-1.75}\ s^{-1}}$)		Model 009 with $D_k = 7.025 \times 10^{-5}$ ($\mathrm{Pa\ m^2\ K^{-1.75}\ s^{-1}}$)	
	Y_{pcbL} (x 10^6)	T_L (K)	Y_{pcbL} (x 10^6)	T_L (K)
pcb6 (10, 2b)	3699	951	3684	951
pcb8 (10, 2d)	2892	1084	2867	1083

Model 009 ($R_w = 0$; annular velocity profile; uniform mesh; 1654 elements; $T_O = 778$ K (pcb6) 883 K (pcb8); $T_{LR} = 450$ K; ibou = 4; $T_{refl} = T_O$; $T_{ref2} = 450$ K; $h_{eff} = 440\ \mathrm{W\ m^{-2}}$)

Since there was now a greater degree of confidence in the use of a higher diffusion coefficient, the next stage was to determine what values of D_k in the model would exactly match the experimental conversions for the four catalytic runs. These D_k values are shown in Table 4-11 and the corresponding simulated and experimental axial temperature profiles are given in Figure 4-25(a) to 4-25(d). From these results the following observations were made:

i) As the length of the reactor channel increases the value of D_k required to match the experimental conversions decreases. The D_k values correspond to a diffusion coefficient that is averaged over the channel length to give a match in the outlet conversions. If there was some turbulence at the entrance of the channel, maybe due to a disturbance introduced by the manifold, it would be expected that the degree of turbulence will die down with distance along the channel. The observed trend in the D_k value is consistent with this hypothesis.

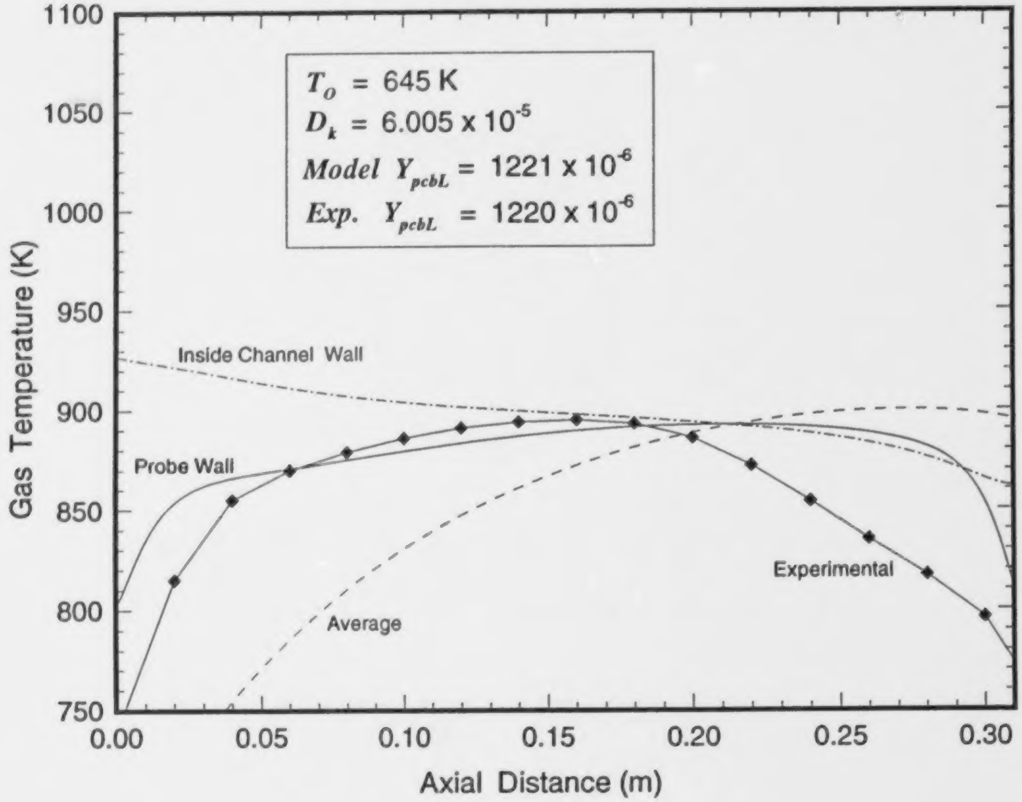

Model 109 (cat3 (3d); k_W = 2 m s^{-1}; annular velocity profile; no. elements 2054; T_O = 645 K; T_{LR} = 450 K; ibou = 4; T_{refl} = T_O; T_{ref2} = 500 K; h_{eff} = 367 W m^{-2})

Figure 4-25(a). Axial temperature profiles at an increased diffusion coefficient.

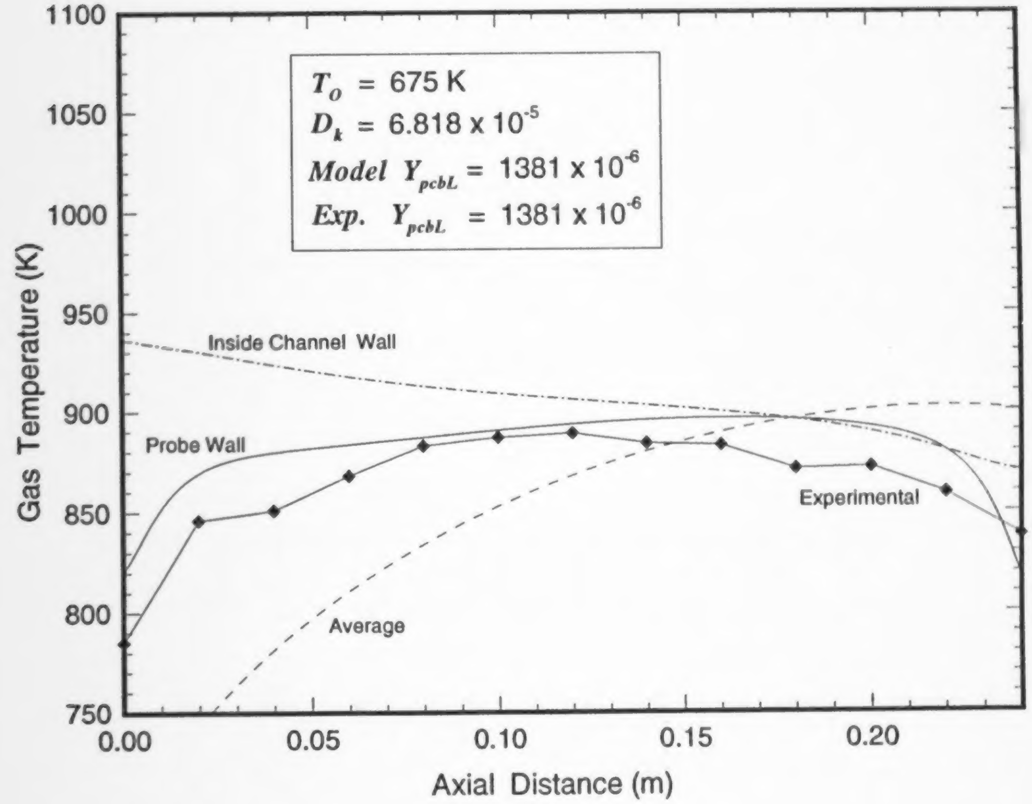

Model 109 (cat4 (4a); k_W = 2 m s^{-1}; annular velocity profile; no. elements 1594; T_O = 675 K; T_{LR} = 450 K; ibou = 4; T_{ref1} = T_O; T_{ref2} = 500 K; h_{eff} = 367 W m^{-2})

Figure 4-25(b). Axial temperature profiles at an increased diffusion coefficient.

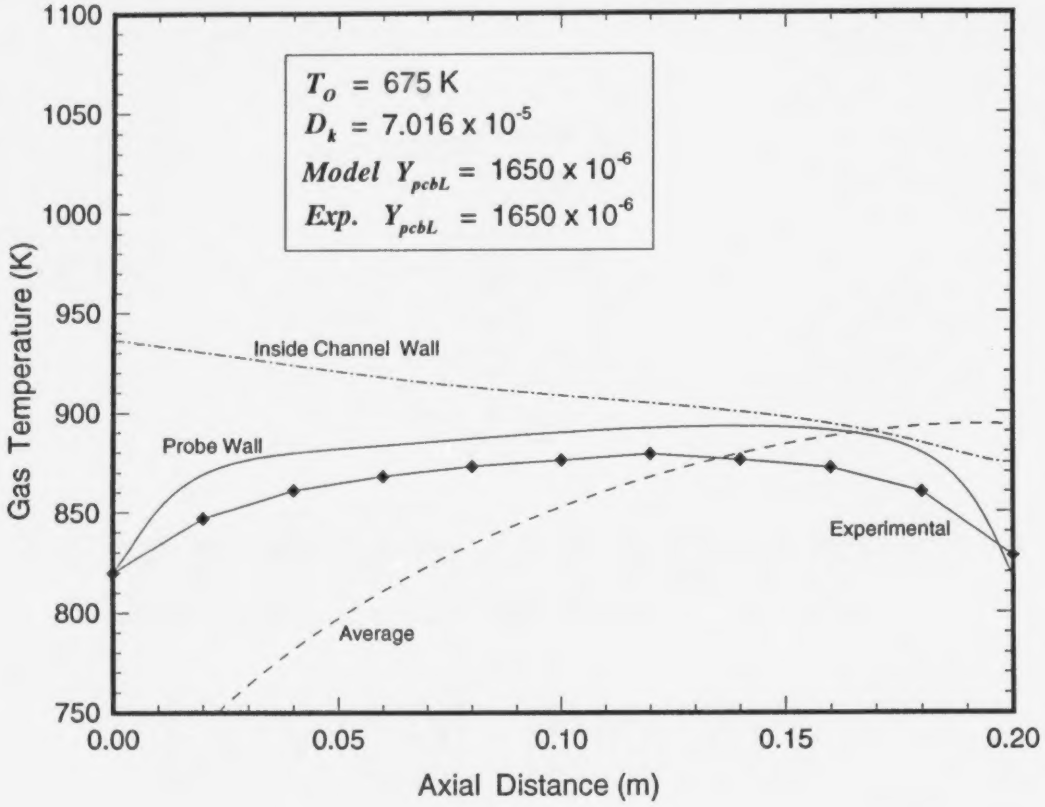

Model 109 (cat5 (5f); k_W = 2 m s^{-1}; annular velocity profile; no. elements 1324; T_O = 675 K; T_{LR} = 450 K; ibou = 4; T_{refl} = T_O; T_{ref2} = 500 K; h_{eff} = 367 W m^{-2})

Figure 4-25(c). Axial temperature profiles at an increased diffusion coefficient.

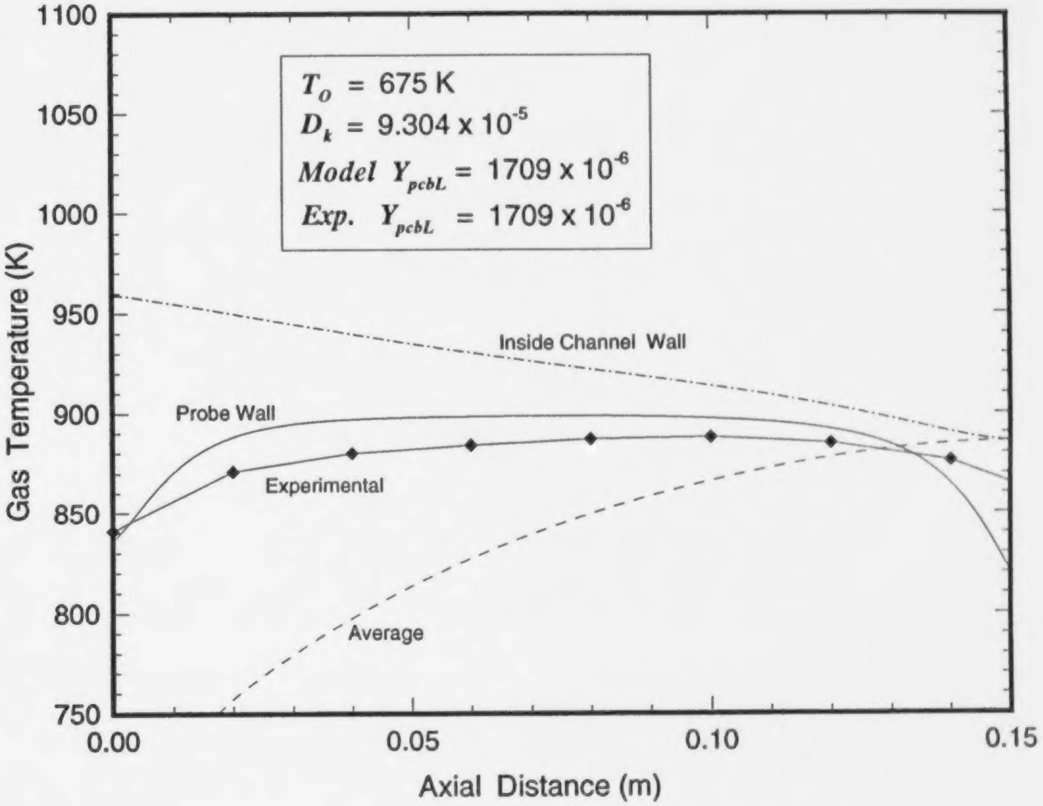

Model 109 (cat6 (6a); k_W = 2 m s^{-1}; annular velocity profile; no. elements 994; T_O = 675 K; T_{LR} = 450 K; ibou = 4; T_{refl} = T_O; T_{ref2} = 500 K; h_{eff} = 367 W m^{-2})

Figure 4-25(d). Axial temperature profiles at an increased diffusion coefficient.

ii) The simulated temperature profile for the probe wall agrees fairly well with the experimental profile measured with the thermocouple probe. Generally the shape of the two curves are consistent though some deviation is apparent near the entrance and exit of the channel.

iii) The inlet average gas temperature T_O is 100 - 160 K lower than the measured inlet probe temperature. This highlights the fact that the temperature recorded by the probe is significantly effected by the presence of zero slip velocity, internal radiation and axial wall conduction.

The data in Table 4-11 were all based on experimental runs with the same inlet PCB mole fraction *ie* $Y_{pcbo} = 5374 \times 10^{-6}$. It was now necessary to ascertain if a similar trend in D_k with channel length existed at different inlet PCB concentrations. Employing the same technique of increasing the diffusion coefficient to simulate some of the other catalytic experimental runs, the results given in Table 4-12 were obtained.

Table 4-11. Results using a variable D_k value

Exp. Number	Channel length (cm)	Inlet Y_{pcbo} (x 10^6)	D_k value used in Model (Pa $m^2K^{-1.75}s^{-1}$)	Experimental Y_{pcbL} (x 10^6)	Model Y_{pcbL} : Developing Flow (x 10^6)
cat3 (3d)	31	5374	6.005×10^{-5}	1220	1221
cat4 (4a)	24	5374	6.818×10^{-5}	1381	1381
cat5 (5f)	20	5374	7.016×10^{-5}	1650	1650
cat6 (6a)	15	5374	9.304×10^{-5}	1709	1709

Model 109 ($A_W = 2$ m s^{-1}, $E_W = 0$; annular velocity profile; uniform mesh; number of elements 2054 (3d), 1594 (4a), 1324 (5f), 994 (6a); $T_O = 675$ K (4a, 5f, 6a) 645 K (3d); $T_{LR} = 450$ K; ibou = 4; $T_{refl} = T_O$; $T_{ref2} = 500$ K; $h_{eff} = 367$ W m^{-2})

Table 4-12. Further results using a variable D_k value

Exp. Number	Channel length (cm)	Inlet Y_{pcbo} (x 10^6)	D_k value used in Model (Pa $m^2K^{-1.75}s^{-1}$)	Experimental Y_{pcbL} (x 10^6)	Model Y_{pcbL} : Developing Flow (x 10^6)
cat4 (4c)	24	6298	9.928×10^{-5}	982	980
cat4 (4b)	24	5888	7.095×10^{-5}	1425	1426
cat5 (5c)	20	6709	12.680×10^{-5}	959	958
cat5 (5a)	20	5066	5.972×10^{-5}	1788	1789
cat6 (6c)	15	7221	9.320×10^{-5}	2181	2181
cat6 (6d)	15	4963	5.675×10^{-5}	2263	2264

Model 109 ($A_W = 2$ m s^{-1}, $E_W = 0$; annular velocity profile; uniform mesh; number of elements 1594 (cat4), 1324 (cat5), 994 (cat6); $T_O = 675$ K; $T_{LR} = 450$ K; ibou = 4; $T_{ref1} = T_O$; $T_{ref2} = 500$ K; $h_{eff} = 367$ W m^{-2})

These results show that the value of D_k required to match the experimental conversions is effected by the inlet PCB concentration as well as the channel length. Increasing the temperature exponent in Equation (4-11) from 1.75 to 1.80 still gave the same trend. This tends to disprove the hypothesis that the discrepancy between the model and the experimental measurements is turbulence related. Also, experimental smoke tests on the reactor showed that a reasonably good plug velocity profile existed after the inlet manifold. There is obviously some other concentration related phenomena occurring, that has as yet not been accounted for in the reactor model. This will be addressed in the following section.

4B.4 Homogeneous Kinetics Reviewed

Since the discrepancy in model could not be adequately explained by turbulence in the channel a third hypothesis was proposed; the homogeneous kinetics obtained in Section 4A are not valid for the modelling of the catalytic experiments because of either or a combination of the following:

i) In the uncoated channel experiments the temperature and residence time of the reactor was not sufficient to cause the complete combustion of PCB to HCl, CO_2 and H_2O. If this is true, the activation energy E_H given in Equation (4-5) would be too low for complete combustion of PCB and is only representative of a PCB disappearance reaction to a non PCB product. In the catalytic experiments it is believed that the combustion was more complete than in the uncoated channel experiments.

ii) The average gas temperatures in the catalytic experiments are about 50 K higher and the channel wall temperatures are 30 - 80 K higher than the uncoated channel experiments. At increased temperatures a different PCB combustion mechanism may be present which would mean that the homogeneous combustion kinetics would probably be different.

The following evidence tends to support the above hypotheses:

i) In Section 4A it was apparent that the simulated axial probe temperature profiles were always higher than the experimentally measured profiles. By reducing the heat of reaction for PCB in the model and therefore accounting for some incomplete combustion, the profiles gave closer agreement.

ii) Inspection of the experimental apparatus revealed that the inside of the piping was coated in a tarry/carbon deposit. Partial PCB oxidation reactions are suspected to have formed these heavy hydrocarbon and carbon products. In addition, the analysis of an oily layer formed in one of the runs confirmed the presence of lower molecular weight species. It is unlikely these compounds would have appeared with the PCB peak in the HPLC analysis. Analysis trials using the HPLC equipment with known compounds like trichlorobenzene, chlorobenzene and trichloroethylene, all resulted in retention times that were considerably different from those expected for the PCB.

iii) Literature data on the combustion of similar chlorinated aromatics quote activation energies 2-3 times higher than the activation energy that was derived for the homogeneous PCB combustion, see Table 4-13.

In order to test the hypothesis further, the reactor model was again used to simulate the catalytic experiments given in Table 2-5(a). This time the original molecular diffusion coefficient was used *ie* $D_k = 2.532 \times 10^{-5}$ Pa m^2 K$^{-1.75}$ s^{-1} with the following arbitrary catalytic rate:

$$R_W = 2.0 \text{ mol m}^{-2} \text{ s}^{-1}$$

Table 4-13. Global homogeneous combustion kinetics for aromatics

Homogeneous kinetics derived for PCB: $E_H = 38{,}010$ J mol^{-1}; $A_H = 473$ s^{-1}			
Chemical	Experimental Temperatures (K)	E_H (J mol^{-1})	A_H (s^{-1})
chlorobenzene *	810 - 980	96,300	8.32×10^4
chlorobenzene †	870 - 1000	96,000	8.0×10^4
1,2-dichlorobenzene *	900 - 1010	167,500	4.47×10^8
1,2,4-trichlorobenzene *	910 - 1020	163,300	1.95×10^8
benzene *	900 - 1000	163,300	4.27×10^8
benzene ‡	1350 - 1500	146,566	9.38×10^8

* Data taken from Dellinger *et al.* [47], conditions: tubular reactor 1 mm diameter; dry flowing air; residence time of 1-6 seconds.

† Data taken from Delplanque *et al.* [61], conditions: rectangular channel of 5 mm width; preheated flowing air carrier gas.

‡ Data taken from Fujii *et al.* [62], conditions: shock tube technique, range of conditions, air atmosphere.

Following the same procedure as described in Section 4A.1, a temperature independent homogeneous rate constant k_H was used to match the experimental conversions for a selection of the experimental runs. Table 4-14 gives the values of k_H that matched the experimental conversions and the radial average temperature $T_{L/2}$ simulated at the midpoint of the reactor. As before this data was used to produce a plot of $\log(A_H)$ versus E_H, see Figure 4-26.

Table 4-14. Results for temperature independent kinetics

Experiment Number	Inlet Y_{pcbo} (x 10^6)	Rate constant k_H (s^{-1})	Exp. Y_{pcbL} (x10^6)	Model Y_{pcbL} (x10^6)	Model $T_{L/2}$ (K)
cat3 (3d)	5374	3.787	1220	1220	860
cat3 (3a)	6196	6.973	1456	1456	970
cat3 (3e)	5168	4.812	1509	1509	915
cat4 (4a)	5374	4.905	1381	1381	891
cat4 (4c)	6298	14.44	982	982	1064
cat4 (4f)	4675	5.901	1440	1440	929
cat5 (5f)	5374	4.983	1650	1651	882
cat5 (5c)	6709	20.36	959	959	1118
cat5 (5g)	4551	5.479	1698	1698	911
cat6 (6a)	5374	5.978	1709	1707	872
cat6 (6d)	4963	5.419	2263	2263	898
cat6 (6g)	2488	3.012	1311	1311	830

Model 009 ($A_W = 2$ m s^{-1}, $E_W = 0$; annular velocity profile; uniform mesh; number of elements 2054 (cat3), 1594 (cat4), 1324 (cat5), 994 (cat6); $T_O = 750$ K; $T_{LR} = 450$ K; ibou = 4; $T_{ref1} = T_O$; $T_{ref2} = 500$ K; $h_{eff} = 367$ W m^{-2})

BLANK PAGE INSERTED

NO INFORMATION MISSING

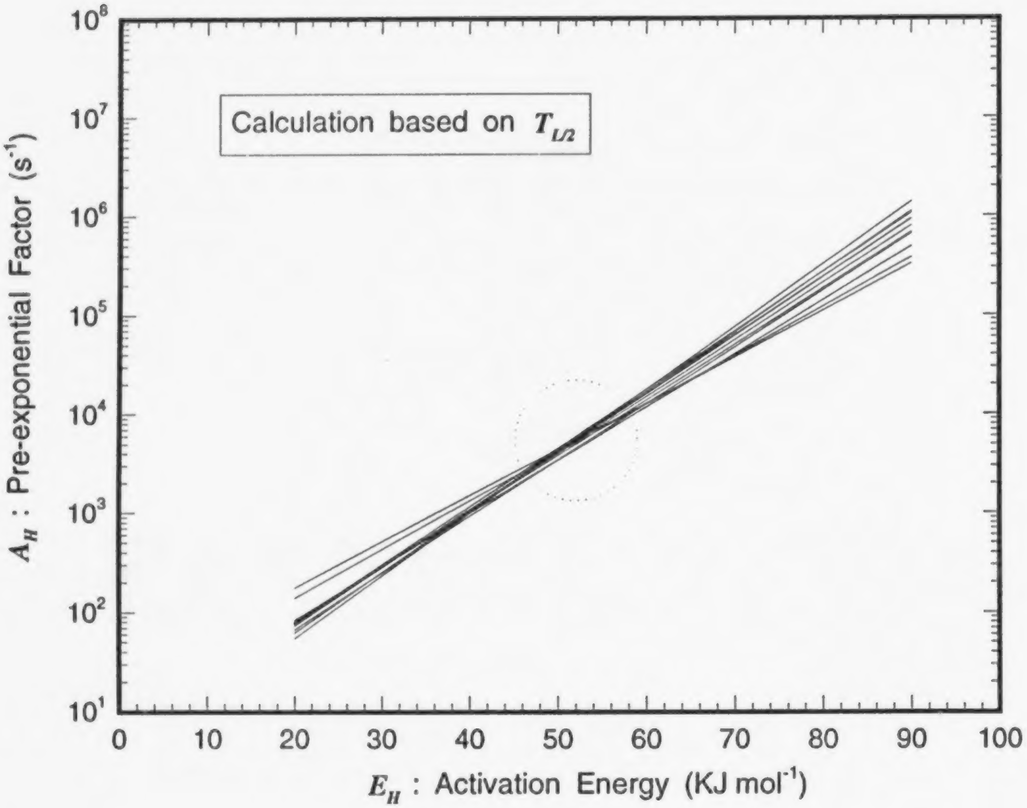

Figure 4-26. Homogeneous kinetics reviewed.

It can be seen from Figure 4-26 that most of the lines intersect in one region at approximately E_H = 52 kJ mol^{-1}. This suggests that the following homogeneous kinetic expression is more valid for the catalytic experiments than Equation (4-5) derived previously:

$$R_H = 7 \times 10^3 \exp\left[-\frac{52,000}{R_g T} \right] \frac{P\,Y_{pcb}}{R_g T} \qquad \textbf{(4-12)}$$

Employing these revised homogeneous kinetics the complete reactor model was used to simulate the four experiments given in Table 2-5(b), the temperature profiles are shown in Figures 4-27(a) to 4-27(d). The following was concluded:

i) The homogeneous kinetics given in Equation (4-12) are a more reasonable expression for the catalytic experiments since the simulated conversions now agree fairly well with the experimental values. Comparing this kinetic expression with Equation (4-5) that was obtained from analysing the uncoated channel experiments, suggests that the combustion of PCB was more complete in the catalytic experiments.

ii) The simulated probe wall profiles agree fairly well with the measured profiles. However, the model tends to over predict the probe wall temperatures as axial distance increases. This discrepencancy suggests that there was still a degree of incomplete combustion in the catalytic experiments. The new E_H value is still considerably lower than the literature values for similar chemicals given in Table 4-13. Alternatively, a combination of an increased diffusion coefficient and the revised homogeneous kinetics may be necessary to accurately describe the conditions in the experimental reactor system.

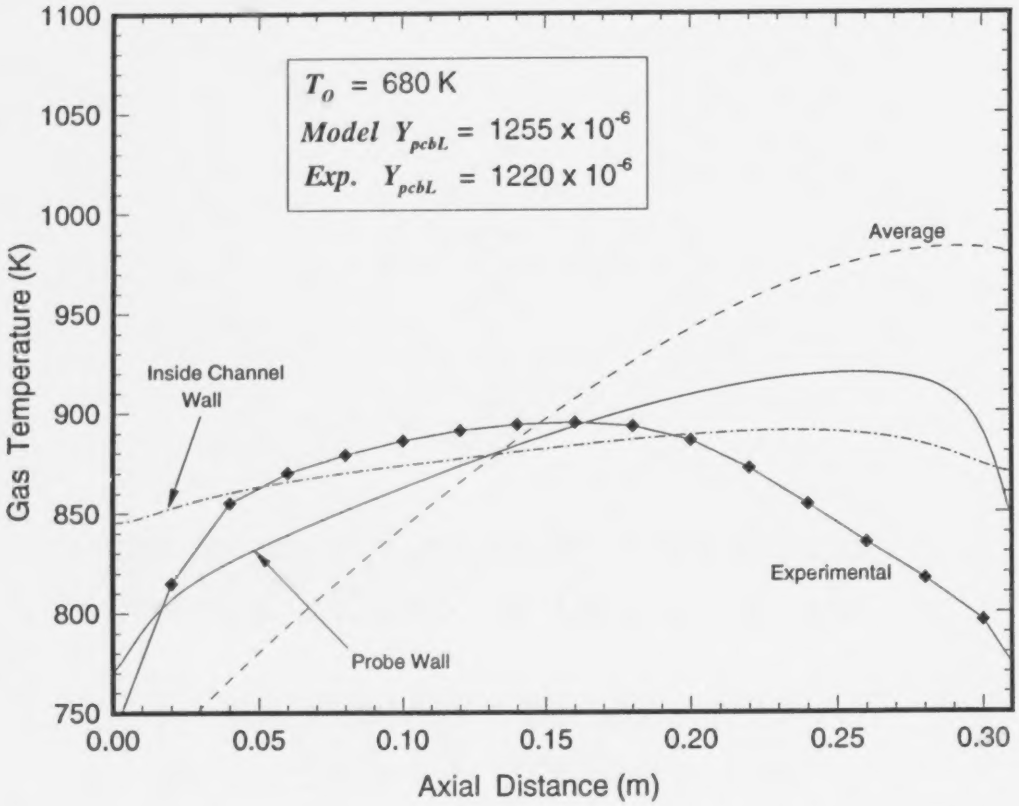

Model 009 (cat3 (3d); $A_H = 7000\ s^{-1}$, $E_H = 52\ kJ\ mol^{-1}$; $k_W = 2\ m\ s^{-1}$; annular velocity; elements 2054; $T_O = 680$ K; $T_{LR} = 450$ K; ibou = 4; $T_{refl} = T_O$; $T_{ref2} = 500$ K; $h_{eff} = 367\ W\ m^{-2}$)

Figure 4-27(a). Axial temperature profiles : Homogeneous kinetics reviewed.

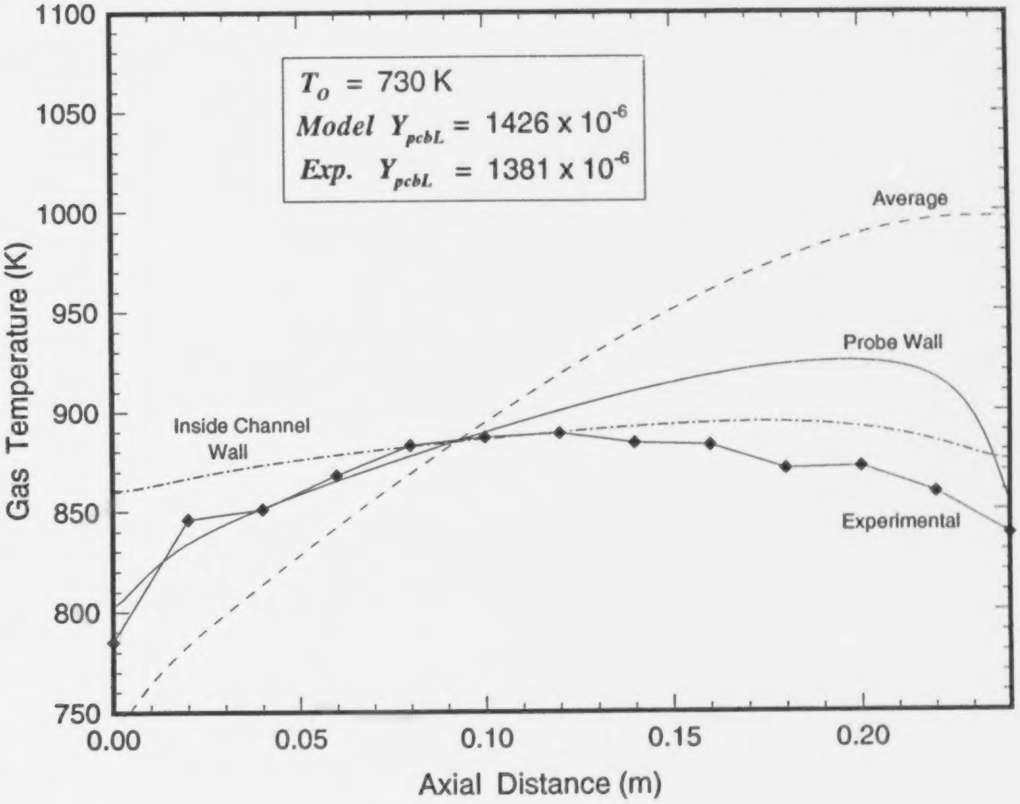

Model 009 (cat4 (4a); $A_H = 7000\ s^{-1}$, $E_H = 52\ kJ\ mol^{-1}$; $k_W = 2\ m\ s^{-1}$; annular velocity; elements 1594; $T_O = 730$ K; $T_{LR} = 450$ K; ibou = 4; $T_{refl} = T_O$; $T_{ref2} = 500$ K; $h_{eff} = 367\ W\ m^{-2}$)

Figure 4-27(b). Axial temperature profiles : Homogeneous kinetics reviewed.

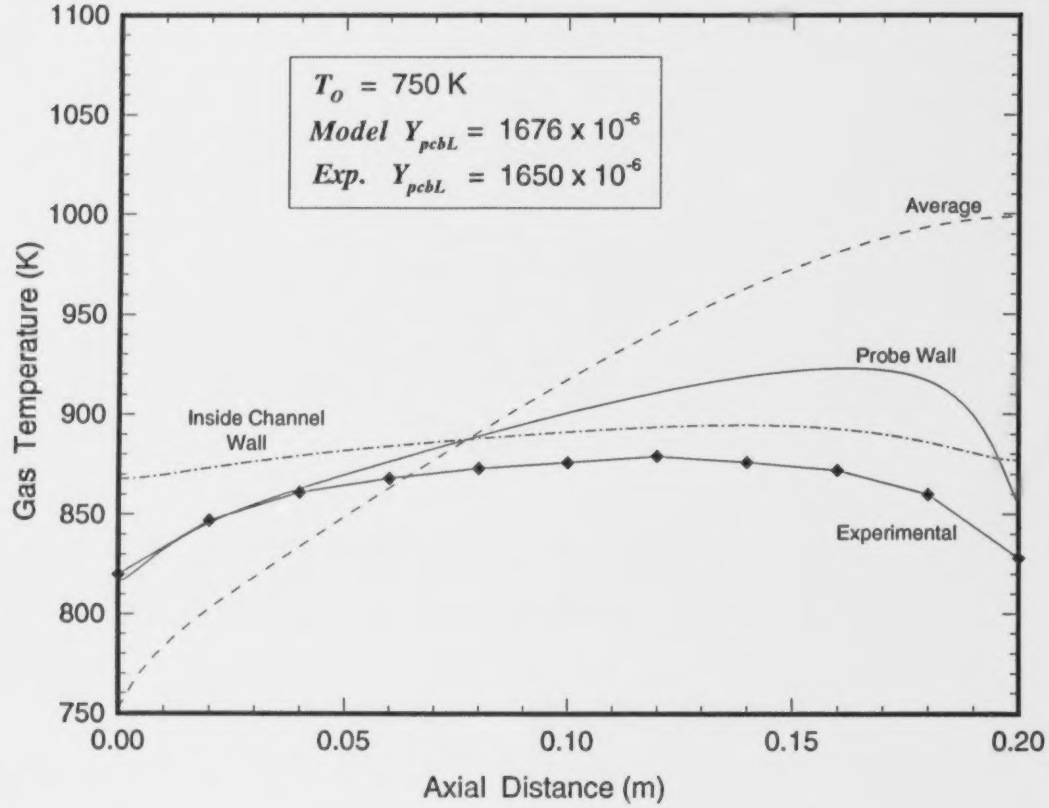

Model 009 (cat5 (5f); $A_H = 7000\ s^{-1}$, $E_H = 52\ kJ\ mol^{-1}$; $k_W = 2\ m\ s^{-1}$; annular velocity; elements 1324; $T_O = 750\ K$; $T_{LR} = 450\ K$; ibou = 4; $T_{refl} = T_O$; $T_{ref2} = 500\ K$; $h_{eff} = 367\ W\ m^{-2}$)

Figure 4-27(c). Axial temperature profiles : Homogeneous kinetics reviewed.

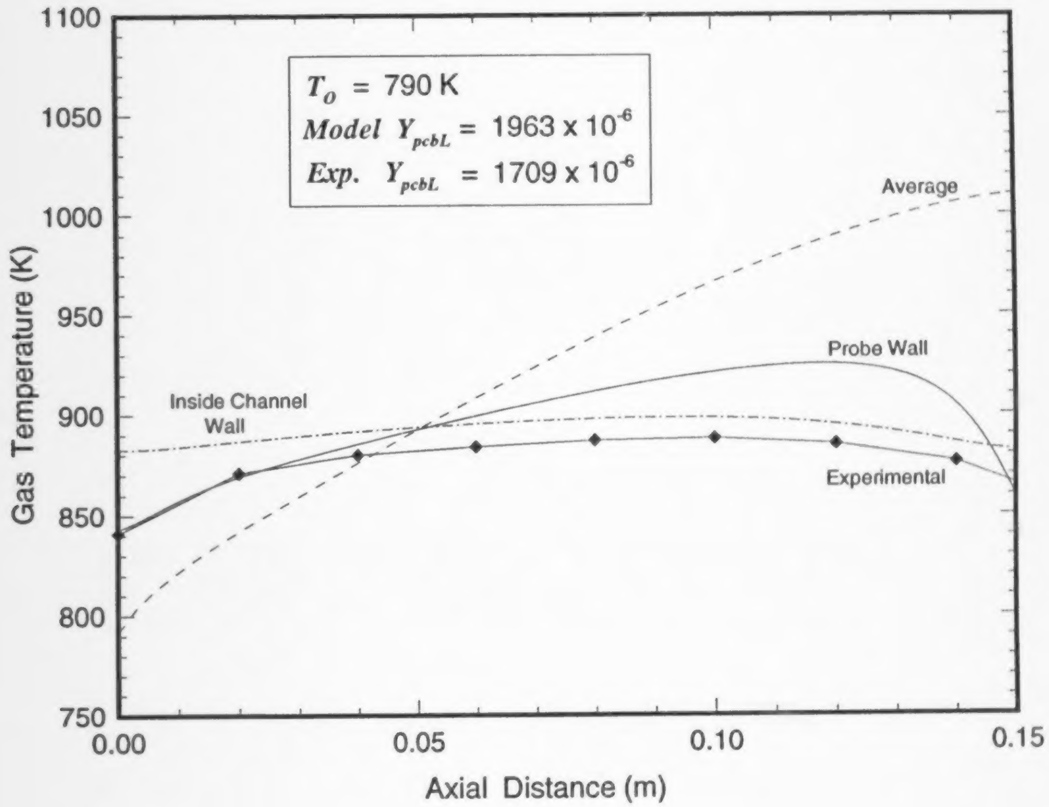

Model 009 (cat6 (6a); A_H = 7000 s^{-1}, E_H = 52 kJ mol^{-1}; k_W = 2 m s^{-1}; annular velocity; elements 994; T_O = 790 K; T_{LR} = 450 K; ibou = 4; T_{ref1} = T_O; T_{ref2} = 500 K; h_{eff} = 367 W m^{-2})

Figure 4-27(d). Axial temperature profiles : Homogeneous kinetics reviewed.

5

CONCLUSIONS AND RECOMMENDATIONS

In this chapter a summary of the important results obtained from the numerical modelling of the experimental data are presented and conclusions are drawn. As a result of the work that has been completed in this research, recommendations are made for possible future areas of study.

5.1 Conclusions

i) Catalytic combustion in a monolith reactor offers much potential as a commercial technique to destroy safely PCB or other chlorinated wastes at relatively low operating temperatures.

ii) A comprehensive mathematical model of a single channel monolith reactor has been developed. It includes the effects of internal and external radiation, axial wall conduction, empty tube or annular configuration, fully developed or developing gas flow as well as homogeneous and catalytic reaction.

iii) Optimum model convergence behaviour was obtained using the transient algorithm which involves solving the channel and probe wall temperature profile as separate 1-D finite element problems.

iv) The optimum kinetic expression for the disappearance of PCB in the uncoated channel experiments was found to be:

$$R_H = 473 \exp\left[-\frac{38{,}010}{R_g T} \right] \frac{P\, Y_{pcb}}{R_g T} \qquad \textbf{(5-1)}$$

The predicted outlet PCB mole fractions were within 15% of the experimental values. However, with these kinetics the simulated axial probe temperature profiles were higher than the profiles measured experimentally. Visual observations and comparison of the kinetic values with literature data on similar chlorinated aromatics, suggest that incomplete PCB combustion was present in the uncoated channel experiments.

v) The radial temperature profiles obtained showed considerable axial variation indicating that the flow was thermally non-developed. Consequently, the Nusselt and Sherwood numbers also exhibited unusual behaviour along the reactor length. This demonstrates the superiority of using a two-dimensional mathematical model and the difficulty of obtaining accurate correlations for the mass and heat transfer coefficients.

vi) The simulation work has shown that the axial probe wall temperature profile is significantly effected by internal radiation and axial wall conduction. In this study the average inlet gas temperature was found to be 20 - 150 K lower than the inlet probe wall temperature. This highlights the difficulties of using a thermocouple in a high temperature reactor to obtain a meaningful gas temperature.

vii) To obtain an accurate model of the wall temperature profiles in a monolith channel it is important to take account of internal radiation and wall conduction. However, at the experimental conditions used in this study, a reasonable estimate of the average outlet conversion and gas temperature can be determined using a basic Model 068; no internal radiation or wall conduction.

viii) No significant difference was apparent between the simulation results using fully developed and developing gas flow. In this study the Reynolds number was about 270, which gives a developing length $L_D \approx 7$ cm.

ix) At a inside channel diameter of 15 mm and an average inlet gas velocity of about 1.5 m s^{-1}, the catalytic wall reaction was found to be limited by the rate of diffusion.

x) Simulation of the experimental data from the catalytic coated channel experiments suggested that the homogeneous kinetics given in Equation (5-1) were not valid in this case. In the catalytic experiments it is believed that the combustion was more complete than in the uncoated channel experiments. The following homogeneous kinetics were found to give a better match to the conversions obtained in the catalytic work:

$$R_H = 7 \times 10^3 \exp\left(-\frac{52{,}000}{R_g T}\right) \frac{P\,Y_{pcb}}{R_g T} \qquad \textbf{(5-2)}$$

The simulated probe wall profiles agreed well with the measured profiles. However, the model tended to over predict the probe wall temperatures as axial distance increased, this suggests that there was still some degree of incomplete combustion in the catalytic experiments.

5.2 Recommendations for Future Work

i) Measure the complete distribution of products in the reactor effluent so that it is possible to ascertain the extent of PCB combustion and possible steps in the reaction mechanism.

ii) Ensure that the uncoated channel experiments are carried out over the same temperature range as the catalytic coated channel experiments. The homogeneous kinetics evaluated from the former set of experiments, are then more likely to be valid when both homogeneous and catalytic combustion coexist.

iii) Measure axial centre-line and channel wall temperatures for the following experimental trials:

  - hot gas flow without combustion in the channel.
  - combustion of a chemical which has well known oxidation kinetics and molecular diffusion coefficient.

These experiments would be useful to further validate the model of the single channel monolith reactor.

iv) Try to establish by measurement or apparatus design the wall temperatures preceding the entrance and beyond the exit of the reactor. It is important to obtain a reasonable estimate of the temperatures since these parameters are required to model the internal channel radiation and axial wall conduction.

v) In order to determine the catalytic kinetics, the experimental conditions should be chosen to eliminate diffusion limited wall reaction. The value of the channel diameter and inlet gas velocity at which a transition from reaction to diffusion controlled catalytic reaction occurs, can be established from further work with the reactor model.

vi) It may be important to include in the reactor model the phenomena of radial convection caused by hot layers of gas near the channel wall.

vii) Instead of using pseudo first order kinetics, it may be better to model homogeneous and catalytic PCB oxidation with a multi-step kinetic model. The influence of radicals produced by the catalytic reaction on the rate of homogeneous reaction and *vice versa* could also be considered.

viii) An insight into the mechanism of PCB combustion may be gained by completing combustion experiments with similar chemicals such as chlorobenzene and biphenyl.

ix) Explore possible methods of conversion enhancement by changing the operating conditions of the monolith reactor.

x) Compare experimental data obtained with a multi-channel monolith reactor with results obtained using the model of the single channel monolith.

xi) Complete scale-up and cost analysis calculations to assess the viability of using a monolith reactor for large-scale hazardous waste combustion.

REFERENCES

1. Hutzinger, O., Safe, S. and Zitko, V., *The Chemistry of PCBs*, CRC Press, Cleveland, 1974.

2. Sissons, D. and Welti, D., *Structural Identification of Polychlorinated Biphenyls in Commercial Mixtures by Gas-Liquid Chromatography and Nuclear Magnetic Resonance and Mass Spectroscopy*, J Chromatography, 1971, 60, pp. 15-20.

3. Crittenden, B.D., Kolaczkowski, S.T. and Perera, S.P., *Polychlorinated Biphenyls: 1. Properties, Health Risks and Legislation*, Environmental Protection Bulletin, 1990, 004, pp. 25-32.

4. Crittenden, B.D., Kolaczkowski, S.T. and Perera, S.P., *Polychlorinated Biphenyls: 2. Disposal and Treatment by Incineration*, Environmental Protection Bulletin, 1990, 009, pp. 10-21.

5. *PCBs in the U.S.: Industrial Use and Environmental Distribution*, 1976, EPA Report 560/6-76-005.

6. Kuratasune, J., Masuda, Y., and Nagayamma, J., *Some Recent Findings Concerning Yusha*, Proceedings of the National Conference on Polychlorinated Biphenyls, 1975, Chicago, U.S., EPA Report 560/6-75-004.

7. Kimbrough, R.D., *International Perspectives on PCBs (Polychlorinated Biphenyls), PCDFs (Polychlorinated dibenzofurans) and PCDDs (polychlorinated dibenzodioxins) in the environment*, 1986, paper presented at Royal Society Discussion Meeting, London, U.K..

8. International Agency for Research on Cancer, *Monographs on the Evaluation of the Carcinogenic Risk of Chemicals to Humans*, 1978, 18, PCBs, WHO/IARC, Geneva.

9. American Conference of Governmental Industrial Hygienists, *TLVs threshold limit values for chemical substances and physical agents in the work environment and biological exposure indices*, 1985, Ohio, 13, pp. 3-4.

10. Canadian Centre for Occupational Health and Safety, *PCBs: The Current Situation*, 1986, CCOHS P86-3E, Toronto.

11. Ackerman, D.G., Scinto, L.L., Bakshi, R.G., Delumyea, R.G., Johnson, R.J., Richard, G., Takata, A.M. and Sworzyn, E.M., *Destruction and Disposal of PCBs by Thermal and Non-Thermal Methods*, Noyes Data Corporation, New Jersey, 1983.

12. Exner, J.H. (Ed), *Detoxication of Hazardous Waste*, Ann Arbor Science, Michigan, 1982.

13. Report to the Council of Great Lakes Research Managers, *PCBs: A Case Study, Proceedings of a Workshop on Great Lakes Research Coordination*, 1985, Ontario.

14. Environment Canada, *PCBs - Fate and Effects in the Canadian Environment*, 1988, Report EPS 4/HA/2, Ontario.

15. Department of the Environment, *Third International Conference on the Protection of the North Sea*, UK Guidance Note on the Ministerial Declaration, 1990, London.

16. Environment Canada, *Manual for the Management of Wastes Containing Polychlorinated Biphenyls*, 1987, Manual EPS 9/HA/1, Ottawa.

17. Environment Canada, *Options for the Treatment/Destruction of PCBs and PCB Contaminated Waste*, 1991, Report EPS 2/HA/1, Ottawa.

18. De Zeeuw, M.A. and Lemkowitz, S.M., *Environmentally Acceptable Incineration of Chlorinated Chemical Waste: Review of Theory and Practice*, Delft University Press, Netherlands, 1987.

19. Environment Canada, *The Evaluation of Mobile and Stationary Facilities for the Destruction of PCBs*, 1989, Report EPS 3/HA/5, Ottawa.

20. Ontario Ministry of the Environment, *Preliminary Hearing Document on Proposals for the Regulation of Mobile PCB Destruction Facilities*, 1984, Ontario.

21. Coles, C.W. (St. Lawrence Cement), *The Use of Cement Kiln Technology for the Destruction of Wastes*, Proceedings of 42nd CSChE Conference, 1992, Toronto.

22. Prasad, R., Kennedy, L.A. and Ruckenstein, E., *Catalytic Combustion*, Catal Rev -Sci Eng, 1984, 26, 1, pp. 1-58.

23. Benson, J.S., *Catoxid for Chlorinated Byproducts*, Hydrocarbon Processing, 1979, 58 (10), pp. 107-108.

24. Technology, *Rockwell Develops PCB Incineration Method*, C&EN, 1981, 59, pp. 34-37.

25. Irandoust, S., Anderson, B., *Monolithic Catalyst for Non-Automobile Applications*, Catal Rev -Sci Eng, 1988, 30, 3, pp. 341-392.

26. Kummel, J.T., *Catalysts for Automobile Emission Control*, Prog in Energy and Combustion Sci, 1980, 6, pp. 177-199.

27. Bennett, C.J., Hayes, R.E., Kolaczkowski, S.T. and Thomas, W.J., *An Experimental and Theoretical Study of a Catalytic Monolith to Control Automobile Exhaust Emissions*, Proc Royal Soc London A, 1992, 439, pp. 465-483.

28. Sethuraman, S., Senkan, S.M. and Gutman, D., *An Experimental Study of the Gas Phase Oxidation of* C_6H_5Cl *in a Flow Reactor*, Combust Sci and Tech, 1992, 82, pp. 13-30.

29. Graham, J.L., Hall, D.L. and Dellinger, B., *Laboratory Investigation of the Thermal Degradation of a Mixture of Hazardous Organic Compounds*, Environ Sci Tech, 1986, 20, pp. 703-713.

30. Tsang, W. and Burgess, D., *The Incinerability of Perchloroethylene and Chlorobenzene*, Combust Sci and Tech, 1992, 82, pp. 31-47.

31. Ritter, E.R. and Bozzelli, J.W., *Reactions of Chlorinated Benzenes in* H_2 *and* H_2/O_2 *Mixtures: Thermodynamic Implications on Pathways to Dioxin,* Combust Sci and Tech, 1990, 74. pp. 117-135.

32. Rubey, W.A., Dellinger, B., Hall, D.L. and Mazerb, S.L., *High Temperature Gas-Phase Formation and Destruction of Polychlorinated Dibenzofurans*, Chemosphere, 1985, 14, pp. 1483-1489.

33. Jones, C.J., Hudson, B.C. and Smith, A.J., *The Combustion and Pyrolysis of some Halogenated Organic Compounds in a Laboratory Tube Furnace*, Journal of Hazardous Materials, 1978, 2, pp. 291-295.

34. Senkan, S.M. and Weldon, J., *Catalytic Combustion of* CH_3Cl *by* Cr_2O_3, Combust Sci and Tech, 1986, 47, pp. 229-237.

35. Subbana, P., Greene, H. and Desai, F., *Catalytic Oxidation of Polychlorinated Biphenyls in a Monolithic Reactor System*, Environ Sci Technol, 1988, 22, 5, pp. 557-561.

36. Kolaczkowski, S.T., Beltran, F., Crittenden, B.D. and Jefferies, T.M., *Catalytic Combustion of Polychlorinated Biphenyls*, Trans IChemE, 1990, 68 (B1), pp. 49-56.

37. Kolaczkowski, S.T., Crittenden, B.D. and Perera, S.P., *Catalytic Combustion of Polychlorinated Biphenyls - Catalyst Screening Trials,* Trans IChemE, 1992, 70 (B), pp. 27-38.

38. Benson, S.W., Cruickshank, F.R., Golden, D.M., Haugen, G.R., O'Neal, H.E., Rodgers, A.S., Shaw, R. and Walsh, R., *Activity Rules for the Estimation of Thermochemical Properties*, Chem Rev, 1969, 69, pp. 279-324.

39. Rihani, D.N. and Doraiswamy, L.K., *Estimation of Heat Capacity of Organic Compounds from Group Contributions*, Ind Eng Chem Fundamentals, 1965, 4, pp. 17-21.

40. Hayes, R.E., Kolaczkowski and S.T., Thomas, W.J., *Finite Element Model for a Catalytic Monolith Reactor*, Computers Chem Engng, 1992, 16, 7, pp. 645-657.

41. Bird, R.B., Stewart, W.E. and Lightfoot, E.N., *Transport Phenomena*, Wiley, Toronto, 1960.

42. Coulson, J.M., Richardson, J.F. and Sinnott, R.K., *Chemical Engineering - An Introduction to Chemical Engineering Design*, 6, Pergamon Press, Oxford, 1986.

43. Perry, R.H. and Green, D.W. (Eds), *Chemical Engineers Handbook*, 6th ed., McGraw-Hill, New York, 1984.

44. Fuller, E.N., Schettler, P.D. and Giddings, J.C., *A New Method for the Prediction of Gas-Phase Diffusion Coefficients*, Ind Eng Chem, 1966, 58, (May) 19.

45. Gilliland, E.R., *Diffusion Coefficients in Gaseous Systems*, Ind Eng Chem, 1934, 26, pp. 681-685.

46. Yang M., Karra, S.B. and Senkan, S.M., *Equilibrium Analysis of Combustion / Incineration*, Hazardous Waste & Hazardous Materials, 1987, 4, 1, pp. 55-68.

47. Dellinger, B., Torres, J.L., Rubey, W.A., Hall, D.L., Graham, J.L. and Carnes, R.A., *Determination of the Thermal Stability of Selected Hazardous Organic Compounds*, Hazardous Waste, 1984, 1, 2, pp. 137-157.

48. Lee, K., Jahnes, H.J. and Macauley, D.C., *Thermal Oxidation Kinetics of Selected Organic Compounds*, J Air Pollution Control Assoc, 1979, 29, 7, pp. 749-751.

49. Manning, M.P., *Fluid Bed Catalytic Oxidation: An Underdeveloped Hazardous Waste Disposal Technology*, Hazardous Waste, 1984, 1, 1, pp. 41-65.

50. Greene, H.L. and Subbanna, P., *Catalytic Oxidation of Chlorinated Hazardous Wastes*, Management of Hazardous and Toxic Wastes in the Process Industries, Kolaczkowski, S.T. and Crittenden, B.D. (Eds.), Elsevier Applied Science, 1987, pp. 513-541.

51. Hinton, E. and Owen, D.R., *An Introduction to Finite Element Computations*, Pineridge Press, Swansea, U.K., 1985.

52. Rohsenow, W.M. and Hartnett, J.P. (Eds), *Handbook of Heat Transfer*, McGraw-Hill, New York, 1973.

53. Leuenberger, H. and Person, R.A., *Compilation of Radiation Shape Factors for Cylindrical Assemblies*, ASME paper No. 56-A-144, 1956, pp. 1-19.

54. Crouzeix, M. and Raviert, P.A., *Conforming and Non-Conforming Finite Element Methods for Solving the Stationary Stokes Equations*, RAIRO Série Analyse Numérique, 1973, 7, pp. 33-76.

55. Sparrow, E.M. and Lin, S.H., *The Developing Laminar Flow and Pressure Drop in the Entrance Region of Annular Ducts*, J Bas Engr, Trans ASME, 1964, 86, pp. 827-834.

56. Heaton, H.S., Reynolds, W.C. and Kays, W.M., *Heat Transfer in Annular Passages: Simultaneous Development of Velocity and Temperature Fields in Laminar Flow*, Int J Heat Mass Transfer, 1964, 7, pp. 763-771.

57. Incropera, F.P. and Witt, D.P., *Introduction to Heat Transfer*, 2nd ed., John Wiley & Sons, New York, 1990.

58. Holman, J.P., *Heat transfer*, 6th ed., McGraw-Hill, New York, 1986.

59. Ablow, C.M. and Wise, H., *Theoretical Analysis of Catalytic Combustion in a Monolithic Reactor*, Combust Sci and Tech, 1979, 21, pp. 35-40.

60. Bensalem, O. and Ernst, W.R., *Mathematical Modelling of Homogeneous-Heterogeneous Reaction in Monolithic Catalysts*, Combust Sci and Tech, 1982, 29, pp. 1-12.

61. Delplanque, J.P., Rangel, R.H. and Sirignano, W.A., *Liquid-Waste Incineration in a Parallel-Stream configuration : Parametric study*, Twenty-Third Symposium (International) on Combustion, 1990, Pennsylvania, pp. 887-894.

62. Fujii, N. and Asaba, T., *High Temperature Reaction of Benzene*, J Faculty of Engineering, 1977, The University of Tokyo (B), 34, 1.

A

APPENDIX

In this Appendix further details of some of the calculations that were referred to in the development of the mathematical model given in Chapter 3 are presented, this allows the reader to can gain a better understanding of the steps in the derivations.

A.1 Physical Properties of the Composite Channel Wall

The reactor was comprised of a circular ceramic channel enclosed by a stainless steel tube. Between the stainless steel and ceramic wall there was a uniform air gap, as detailed in Table 2-2 and Figure 2-2. In order to model the physical properties of the channel wall the combined effect of the three components was considered.

The air gap between the steel tube and ceramic channel was 0.5 mm thick at ambient temperature. However, during the combustion experiments the wall temperature is considerably higher and so it may be important to consider the change in the thickness of the air gap due to expansion of the wall material. From the simulation work, a reasonable value for the channel wall temperature is about 850 K. At this temperature the coefficients of thermal expansion for ceramic and stainless steel were taken as [43]:

$$\alpha_c = 5.5 \text{ x } 10^{-6} \text{ K}^{-1}$$

$$\alpha_{ss} = 14 \text{ x } 10^{-6} \text{ K}^{-1}$$

Linear thermal expansion of a length l can be expressed by:

$$\Delta l = \alpha l \Delta T \tag{A-1}$$

If we assume that Equation (A-1) is valid for expansion of the channel wall, then the change in the outside radius of the ceramic channel at 850 K is:

$$\Delta R_c = 5.5 \times 10^{-6} \times 10 \times (850 - 290) = 0.03 \ mm \tag{A-2}$$

and similarly for the inside radius of the stainless steel tube:

$$\Delta R_{ss} = 14 \times 10^{-6} \times 10.55 \times (850 - 290) = 0.08 \ mm \tag{A-3}$$

Using these values, the thickness of the air gap at the experimental wall conditions (850 K) will be about 0.6 mm. Hence, the following radii can be deduced and were used in subsequent calculations:

Ceramic inside radius	$R = 7.50 \times 10^{-3}$ m
Ceramic outside radius	$R_2 = 10.03 \times 10^{-3}$ m
Steel inside radius	$R_3 = 10.63 \times 10^{-3}$ m
Steel outside radius	$R_4 = 12.75 \times 10^{-3}$ m
Air gap inside radius	$R_2 = 10.03 \times 10^{-3}$ m
Air gap outside radius	$R_3 = 10.63 \times 10^{-3}$ m

Recall that the radial wall conduction resistance λ_w for the composite channel wall was expressed by the following equation:

$$\lambda_w = R \left[\left(\frac{\ln \frac{R_4}{R_3}}{k_{ss}} \right) + \left(\frac{\ln \frac{R_3}{R_2}}{k_{air}} \right) + \left(\frac{\ln \frac{R_2}{R}}{k_c} \right) \right] \tag{A-4}$$

so that this gives a flux based on the inside channel radius R. If we now substitute for the values of the radii and the thermal conductivities given below for the components, we obtain: $\lambda_w = 8.41 \times 10^{-3}$ K m^2 W^{-1}

Table A-1. Cross-sectional areas of the components in the channel wall

Component	Cross-sectional area (mm^2)	% of the total wall cross-sectional area
stainless steel	161	48.22
ceramic	137	41.15
air gap	36	10.63

Table A-1 shows the cross-sectional areas of the components in the channel wall. By using an area weighted average, the combined physical properties of the composite wall were calculated using data from [43,57] *viz*:

Stainless steel density = 7800 kg m^{-3}
Ceramic channel density = 3130 kg m^{-3}
Air gap density = 0.39 kg m^{-3}

⇒ Channel wall density ρ_w = 5049 kg m^{-3}

Stainless steel heat capacity = $502 \text{ J kg}^{-1} \text{ K}^{-1}$
Ceramic channel heat capacity = $1187 \text{ J kg}^{-1} \text{ K}^{-1}$
Air gap heat capacity = $1121 \text{ J kg}^{-1} \text{ K}^{-1}$

⇒ Channel wall heat capacity Cp_w = $850 \text{ J kg}^{-1} \text{ K}^{-1}$

Stainless steel conductivity k_{ss} = $23 \text{ W m}^{-1} \text{ K}^{-1}$
Ceramic channel conductivity k_c = $2.01 \text{ W m}^{-1} \text{ K}^{-1}$
Air gap heat conductivity k_{air} = $0.06 \text{ W m}^{-1} \text{ K}^{-1}$

⇒ Axial wall thermal conductivity k_w = $11.9 \text{ W m}^{-1} \text{ K}^{-1}$

These are the composite values shown in Table 3-1 and used in the reactor model for the channel wall.

A.2 Heat of Combustion for PCB

The heat of reaction of for the combustion of PCB was defined in terms of a fourth order polynomial in temperature. This was determined using the following enthalpy cycle:

$$\Delta H_{R,T} = \Delta H_{R,298} + \Delta H_{prod} - \Delta H_{react} \qquad \textbf{(A-5)}$$

where $\Delta H_{R,T}$ and $\Delta H_{R,298}$ are the standard heats of reaction at the reaction temperature T and 298 K respectively; and ΔH_{prod} is the enthalpy change to bring the reactants to 298 K while ΔH_{react} is the enthalpy change to bring the products to the reaction temperature T. Using the heat of reaction for PCB at 298 K (see Table 2-1) and the reaction stoichiometry given in Section 3.3, by substitution we obtain:

$$\begin{aligned}\Delta H_{R,T} = {} & -5558 \times 10^3 + \int_{298}^{T} 12\, Cp_{co_2}\, dT + \int_{298}^{T} 1.9\, Cp_{h_2o}\, dT \\ & + \int_{298}^{T} 3.1\, Cp_{hcl}\, dT - \int_{298}^{T} Cp_{pcb}\, dT - \int_{298}^{T} 12.95\, Cp_{o_2}\, dT\end{aligned} \qquad \textbf{(A-6)}$$

The heat capacity of each component x in the gas phase can be expressed by the following polynomial:

$$Cp_x = A + BT + CT^2 + DT^3 \qquad \textbf{(A-7)}$$

where the constants A, B, C, D are given for each component in Table A-2. Substituting the *Cp* polynomials for each component into Equation (A-6) and simplifying gives:

$$\begin{aligned}\Delta H_{R,T} = {} & -5558 \times 10^3 + \int_{298}^{T} (\, 61.991 - 4.266 \times 10^{-2}\, T \\ & - 2.382 \times 10^{-4}\, T^2 + 1.789 \times 10^{-7}\, T^3 \,)\, dT\end{aligned} \qquad \textbf{(A-8)}$$

Integrating with the shown limits we obtain the final result for the heat of combustion of PCB at any reaction temperature T:

$$\Delta H_{R,T} = A + BT + CT^2 + DT^3 + ET^4 \tag{A-9}$$

where $\Delta H_{R,T}$ is in J (mol of PCB)$^{-1}$ and the constants are given as:

A = -5572830
B = 61.699
C = -2.133×10^{-2}
D = -7.941×10^{-5}
E = 4.471×10^{-8}

Table A-2. Heat capacity constants for the components of the gas phase

$Cp = A + BT + CT^2 + DT^3$ (J mol^{-1} K^{-1}) *				
Component	A	B	C	D
O_2	28.106	-3.680 E-6	1.745 E-5	-1.065 E-8
HCl	30.291	-7.201 E-3	1.246 E-5	-3.897 E-9
CO_2	19.795	7.343 E-2	-5.601 E-5	1.715 E-8
H_2O	32.243	1.923 E-3	1.055 E-5	-3.596 E-9
PCB 1242 †	-33.26	9.052 E-1	-6.012 E-4	1.466 E-7

* Heat capacity data taken from [42]
† PCB *Cp* constants calculated using group contribution method [39]

A.3 Molecular diffusion Coefficient for PCB

The molecular diffusion coefficient for PCB in air was determined using the Fuller et al. empirical relation [44], as shown below:

$$D = \frac{1.013 \times 10^{-7}\, T^{1.75} \left[\frac{1}{M_A} + \frac{1}{M_B} \right]^{0.5}}{P \left[\nu_A^{\frac{1}{3}} + \nu_B^{\frac{1}{3}} \right]^2} \qquad \textbf{(A-10)}$$

where M is the molecular weight and ν is the summation of the special diffusion volume coefficients for either components A or B. The pressure P has units of bar, temperature T is in K to give the diffusion coefficient D in $m^2\ s^{-1}$.

Taking the following values for air:

$M_{air} = 29$ and $\nu_{air} = 20.1$

and for Aroclor 1242 PCB assuming the following structure $C_{12}H_7Cl_3$:

$M_{pcb} = 261$ and **Element** ν_i

C x 12 = 198.0
H x 7 = 13.86
Cl x 3 = 58.5
2 x aromatic ring = -40.0

ν_{pcb} = 230.36

Then by substitution into the above empirical equation and converting the pressure from bar to Pa, we obtain:

$$D = D_k \frac{T^{1.75}}{P} \qquad \textbf{(A-11)}$$

where $D_k = 2.5322 \times 10^{-5}$ Pa $m^2\ K^{-1.75}\ s^{-1}$. Previously in Table 3-2, it was shown that this relation compared well with literature diffusion data for similar compounds.

A.4 View Factors for an Empty Tube

This section shows in detail the methodology employed in determining the view factors used in the zonal radiation analysis for an empty tube. This methodology is based on an example given by Holman [58] on radiation from a hole. Figure A-1 shows a section of the channel with appropriately labelled surfaces. Surfaces 2 and 4 are the inside surfaces (which may or may not have equal areas) between which we want to determine a view factor F_{24} . These surfaces will have lengths of $2w_1$ and $2w_2$ respectively. Surface 3 is the inside surface of the tube between surfaces 2 and 4. If the distance between the midpoint of surfaces 2 and 4 is denoted as s, then the length of surface 3 will be $(s - w_1 - w_2)$. Surfaces 1, 5, 6 and 7 are "imaginary" circular surfaces at the boundaries of surfaces 2, 3 and 4. This type of analysis is convenient, since the finite element discretisation of the domain naturally produces a number of small discrete surfaces. Each interior surface (2 or 4 in Figure A-1) is simply a single finite element.

The view factor between the opposing surfaces of two coaxial circular disks of equal radius R separated by a distance l is given by the formula:

$$F_{jk} = \frac{1}{2}\left[a - \sqrt{a^2 - 4}\right] \qquad \textbf{(A-12)}$$

where:

$$a = 2 + \left[\frac{l}{R}\right]^2 \qquad \textbf{(A-13)}$$

Thus the quantities F_{17}, F_{16}, F_{67}, etc can be readily determined. For a network of n surfaces exchanging radiant energy, where A is the surface area, we have the following:

summation

$$\sum_{k=1}^{n} F_{jk} = 1 \qquad \textbf{(A-14)}$$

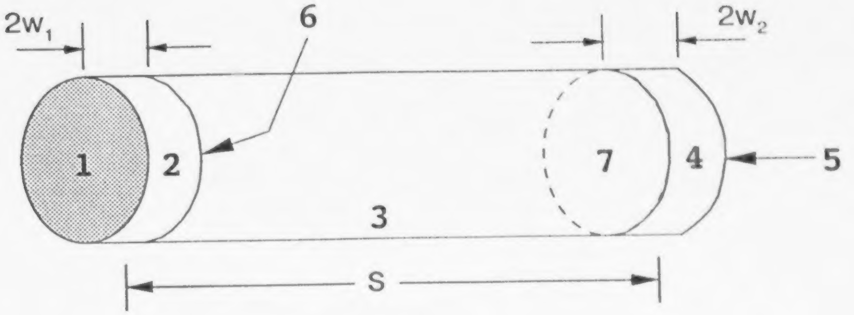
2w$_1$
6
2w$_2$
1
2
7
4
5
3
S

Figure A-1. Diagram of an empty tube : view factors between surface elements.

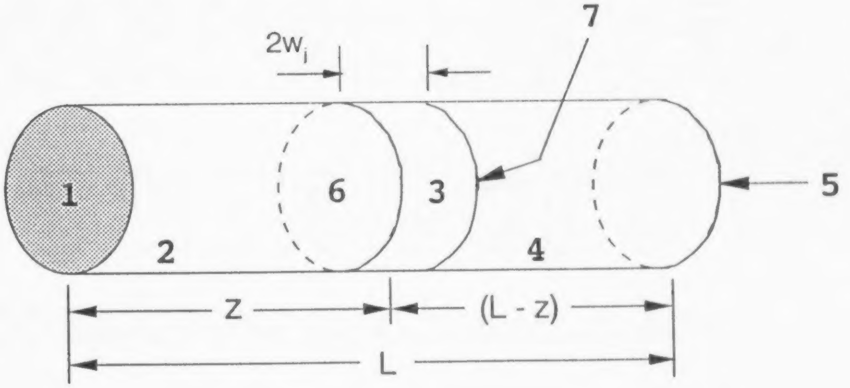
7
2w$_i$
1
6
3
5
2
4
Z
(L - z)
L

Figure A-2. Diagram of an empty tube : view factors to the channel ends.

and reciprocity

$$A_j F_{jk} = A_k F_{kj} \quad \textbf{(A-15)}$$

Using these two relationships plus symmetry, we proceed through the following steps.

$$F_{12} = 1 - F_{16} \quad \textbf{(A-16)}$$

$$F_{13} = F_{16} - F_{17} \quad \textbf{(A-17)}$$

$$F_{14} = F_{17} - F_{15} \quad \textbf{(A-18)}$$

$$F_{21} = F_{26} = \frac{A_1}{A_2}(1 - F_{16}) \quad \textbf{(A-19)}$$

$$F_{22} = 1 - F_{21} - F_{26} = 1 - 2\frac{A_1}{A_2}(1 - F_{16}) \quad \textbf{(A-20)}$$

$$F_{31} = F_{13}\frac{A_1}{A_3} = \frac{A_1}{A_3}(F_{16} - F_{17}) \quad \textbf{(A-21)}$$

$$F_{63} = 1 - F_{67} \quad \textbf{(A-22)}$$

$$F_{36} = \frac{A_6}{A_3} F_{63} = \frac{A_6}{A_3}(1 - F_{67}) \quad \textbf{(A-23)}$$

$$F_{32} = F_{36} - F_{31} = \left[\frac{A_6}{A_3}(1 - F_{67}) - \frac{A_1}{A_3}(F_{16} - F_{17})\right] \quad \textbf{(A-24)}$$

$$\begin{aligned} F_{27} &= F_{26} - F_{23} = F_{21} - F_{32}\frac{A_3}{A_2} \\ &= \frac{A_1}{A_2}(1 - F_{16}) - \frac{A_3}{A_2}\left[\frac{A_6}{A_3}(1 - F_{67}) - \frac{A_1}{A_3}(F_{16} - F_{17})\right] \end{aligned} \tag{A-25}$$

$$F_{25} = \frac{A_5}{A_2}F_{52} = \frac{A_5}{A_2}(F_{56} - F_{51}) \tag{A-26}$$

$$F_{24} = F_{27} - F_{25} \tag{A-27}$$

Thus,

$$\begin{aligned} F_{24} = &- \frac{A_3}{A_2}\left[\frac{A_6}{A_3}(1-F_{67}) - \frac{A_1}{A_3}(F_{16} - F_{17})\right] \\ &+ \frac{A_1}{A_2}(1 - F_{16}) - \frac{A_5}{A_2}(F_{56}-F_{51}) \end{aligned} \tag{A-28}$$

From geometrical considerations, it follows that:

$$A_1 = A_6 = A_5 = \pi R^2 \tag{A-29}$$

$$A_2 = (2w_1)(2\pi R) \tag{A-30}$$

$$\frac{A_1}{A_2} = \frac{R}{4w_1} \tag{A-31}$$

and therefore the final result for the view factor F_{24} is:

$$F_{24} = \frac{R}{4w_1}\left[F_{67} - F_{17} - F_{56} - F_{51}\right] \tag{A-32}$$

Note that if $w_1 = w_2$ then $F_{17} = F_{56}$. The four view factors on the right hand side of Equation (A-32) may be evaluated using Equations (A-12) and (A-13). If these two equations are used with all appropriate dimensions and the results are substituted into Equation (A-32), then, after simplification, Equation (3-35) is generated.

A similar procedure is employed to determine the radiation transfer to the channel ends. Referring to Figure A-2, it can be seen that the view factors F_{31} and F_{35} need to be determined. Since for the entrance:

$$F_{13} = F_{16} - F_{17} \tag{A-33}$$

it follows that,

$$F_{31} = \frac{A_1}{A_3} F_{13} = \frac{A_1}{A_3} (F_{16} - F_{17}) \tag{A-34}$$

and for the exit;

$$F_{53} = F_{57} - F_{56} \tag{A-35}$$

$$F_{35} = \frac{A_5}{A_3} (F_{57} - F_{56}) \tag{A-36}$$

Hence the substitution of Equations (A-12) and (A-13) into Equations (A-34) and (A-36) will give Equations (3-36) and (3-37).

A.5 View Factors for an Annular Geometry

In the previous section the view factors for radiation in an empty tube were derived. If we now include the effect of radiation to the probe wall, a new set of view factors needs to be derived for an annular geometry. This methodology is described here and uses some previous work on radiation in cylindrical assemblies completed by Leuenberger *et al.*[53].

Figure A-3 shows a section of the annulus with appropriately labelled surfaces. Surfaces 1, 9 and 10 are the outer surfaces of the probe wall, surfaces 7, 8 and 2 are the

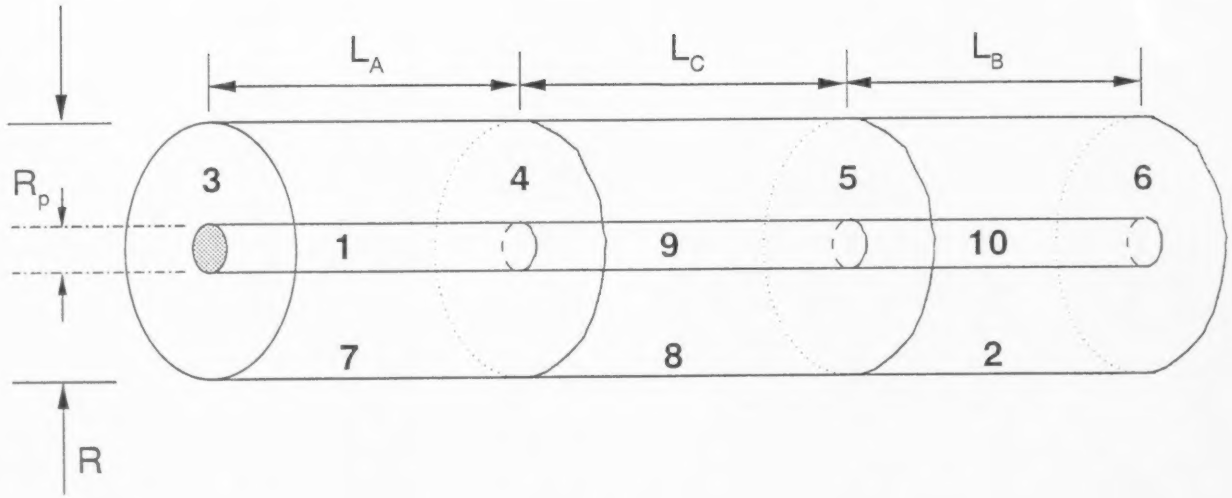

L_A
L_C
L_B
R_p
R
3
4
5
6
1
9
10
7
8
2

Figure A-3. Diagram of an annulus : view factors between surface elements and to the channel ends.

inner surfaces of the channel wall while surfaces 3, 4, 5 and 6 are the "imaginary" annular surfaces perpendicular to the probe and channel wall surfaces. Note that in Figure A-3 the lengths of the surfaces *ie* L_A, L_B and L_C are not necessarily equal. The view factors for "two concentric cylinders of equal length" are given in Leuenberger's paper and the reader is referred to this reference for more details. Thus the following view factors can be deduced and will be regarded as known parameters:

$$F_{34} \quad F_{71} \quad F_{77} \quad F_{13} \quad F_{14} \quad F_{89} \quad F_{88} \quad F_{2,10} \quad F_{22}$$

The objective then is to determine the view factors F_{12} (or F_{21}), F_{72} and $F_{7,10}$. Thus proceeding through the following steps:

$$F_{74} = F_{73} = \frac{1}{2}\left(1 - F_{71} - F_{77}\right) \qquad \textbf{(A-37)}$$

from Leuenberger's paper

$$F_{43} = F_{34} = 1 - \left[\frac{L_A(R_p - R)}{R^2 - R_p^2}\right](F_{77} + 2F_{71} - 1) \qquad \textbf{(A-38)}$$

$$F_{17} = \frac{A_7}{A_1}F_{71} = \frac{R}{R_p}F_{71} \qquad \textbf{(A-39)}$$

$$F_{13} = F_{14} = \frac{1}{2}\left(1 - F_{17}\right) \qquad \textbf{(A-40)}$$

$$F_{31} = \frac{A_1}{A_3}F_{13} = \frac{2\pi R_p L_A}{\pi(R^2 - R_p^2)}F_{13} = F_{41} \qquad \textbf{(A-41)}$$

similarly

$$F_{84} = F_{85} = \frac{1}{2}(1 - F_{89} - F_{88}) \qquad \textbf{(A-42)}$$

from Leuenberger's paper

$$F_{45} = F_{54} = 1 - \left[\frac{L_C (R_p - R)}{R^2 - R_p^2} \right] (F_{88} + 2F_{89} - 1) \qquad \textbf{(A-43)}$$

$$F_{98} = \frac{R}{R_p} F_{89} \qquad \textbf{(A-44)}$$

$$F_{94} = F_{95} = \frac{1}{2} (1 - F_{98}) \qquad \textbf{(A-45)}$$

$$F_{59} = \frac{A_9}{A_5} F_{95} = \frac{2 \pi R_p L_C}{\pi (R^2 - R_p^2)} F_{95} = F_{49} \qquad \textbf{(A-46)}$$

similarly

$$F_{25} = F_{26} = \frac{1}{2} (1 - F_{22} - F_{2,10}) \qquad \textbf{(A-47)}$$

from Leuenberger's paper

$$F_{56} = F_{65} = 1 - \left[\frac{L_B (R_p - R)}{R^2 - R_p^2} \right] (F_{22} + 2F_{2,10} - 1) \qquad \textbf{(A-48)}$$

$$F_{10,2} = \frac{R}{R_p} F_{2,10} \qquad \textbf{(A-49)}$$

$$F_{10,5} = F_{10,6} = \frac{1}{2} (1 - F_{10,2}) \qquad \textbf{(A-50)}$$

$$F_{5,10} = \frac{A_{10}}{A_5} F_{10,5} = \frac{2 \pi R_p L_B}{\pi (R^2 - R_p^2)} F_{10,5} = F_{6,10} \qquad \textbf{(A-51)}$$

Then it follows that:

$$F_{12} = F_{15} - F_{16} \tag{A-52}$$

$$F_{18} = F_{14} - F_{15} \tag{A-53}$$

and

$$F_{59} + F_{51} = F_{5(9+1)} \tag{A-54}$$

where $F_{5(9+1)}$ is the view factor for radiation from surface 5 to the combined surface comprised of elements 9 and 1. Since F_{71} is known then so is $F_{(7+8)(1+9)}$. Defining a view factor F_x as:

$$F_x = F_{(1+9)(7+8)} = \frac{R}{R_p} F_{(7+8)(1+9)} \tag{A-55}$$

hence

$$F_{(1+9)5} = \frac{1}{2}(1 - F_x) \tag{A-56}$$

substituting into Equation (A-54) gives

$$F_{59} + F_{51} = \frac{A_1 + A_9}{2A_5}(1 - F_x) \tag{A-57}$$

$$F_{51} = \frac{A_1 + A_9}{2A_5}(1 - F_x) - \frac{A_9}{A_5} F_{95} \tag{A-58}$$

$$F_{15} = \frac{A_5}{A_1}\left[\frac{A_1 + A_9}{2A_5}(1 - F_x) - \frac{A_9}{A_5} F_{95}\right] \tag{A-59}$$

The view factor F_{16} now needs to be determined, thus

$$F_{6,10} + F_{69} + F_{61} = F_{6(10+9+1)} \tag{A-60}$$

but since $F_{(7+8+2)(1+9+10)}$ is already known, we will define a view factor F_y such that:

$$F_y = F_{(1+9+10)(7+8+2)} = \frac{R}{R_p} F_{(7+8+2)(1+9+10)} \tag{A-61}$$

hence

$$F_{(1+9+10)6} = \frac{1}{2}\left(1 - F_y\right) \tag{A-62}$$

substituting into Equation (A-60)

$$F_{6,10} + F_{69} + F_{61} = \frac{A_{10} + A_9 + A_1}{2A_6}\left(1 - F_y\right) \tag{A-63}$$

substituting for $F_{6,10}$ from Equation (A-50) gives

$$F_{16} = \frac{A_6}{A_1}\left[\frac{A_{10} + A_9 + A_1}{2A_6}(1 - F_y) - \frac{A_{10}}{2A_6}(1 - F_{10,2}) - F_{69}\right] \tag{A-64}$$

It now follows that:

$$F_{6,10} + F_{69} = F_{6(9+10)} \tag{A-65}$$

but since $F_{(8+2)(9+10)}$ is already known, we will define a view factor F_z such that:

$$F_z = F_{(9+10)(8+2)} = \frac{R}{R_p} F_{(8+2)(9+10)} \tag{A-66}$$

hence

$$F_{(9+10)6} = \frac{1}{2}\left(1 - F_z\right) \tag{A-67}$$

substituting into Equation (A-65)

$$F_{69} + F_{6,10} = \frac{A_9 + A_{10}}{2A_6}\left(1 - F_z\right) \tag{A-68}$$

substituting for $F_{6,10}$ from Equation (A-50) gives

$$F_{69} = \frac{A_9 + A_{10}}{2A_6}\left(1 - F_z\right) - \frac{A_{10}}{2A_6}\left(1 - F_{10,2}\right) \tag{A-69}$$

then from Equation (A-64) we obtain

$$F_{16} = \frac{A_6}{A_1}\left[\frac{A_{10} + A_9 + A_1}{2A_6}\left(1 - F_y\right) - \frac{A_9 + A_{10}}{2A_6}\left(1 - F_z\right)\right] \tag{A-70}$$

and so finally substituting for F_{15} and F_{16} in Equation (A-52) gives

$$\begin{aligned} F_{12} = {} & \frac{A_1 + A_9}{2A_1}\left(1 - F_x\right) - \frac{A_9}{2A_1}\left(1 - F_{98}\right) \\ & - \frac{A_{10} + A_9 + A_1}{2A_1}\left(1 - F_y\right) + \frac{A_9 + A_{10}}{2A_1}\left(1 - F_z\right) \end{aligned} \tag{A-71}$$

For adjacent elements it can also be shown that Equation (A-71) simplifies to:

$$F_{18} = \frac{1}{2}\left(1 - F_{17}\right) - \frac{A_1 + A_9}{2A_1}\left(1 - F_x\right) + \frac{A_9}{2A_1}\left(1 - F_{98}\right) \tag{A-72}$$

From geometrical considerations:

$$A_1 = 2\pi R_p L_A \tag{A-73}$$

and similarly for A_9 and A_{10}.

Thus substitution of the respective areas of the elements into Equation (A-71), gives the final result for F_{12}:

$$\boxed{\begin{aligned} F_{12} = {} & \frac{L_A + L_C}{2L_A}\left(1 - F_x\right) - \frac{L_C}{2L_A}\left(1 - F_{98}\right) \\ & - \frac{L_A + L_B + L_C}{2L_A}\left(1 - F_y\right) + \frac{L_B + L_C}{2L_A}\left(1 - F_z\right) \end{aligned}} \qquad \textbf{(A-74)}$$

Since F_{12} can be determined then by similar reasoning $F_{7,10}$ is given by:

$$\boxed{\begin{aligned} F_{10,7} = {} & \frac{L_B + L_C}{2L_B}\left(1 - F_{(9+10)(8+2)}\right) - \frac{L_C}{2L_B}\left(1 - F_{98}\right) \\ & - \frac{L_A + L_B + L_C}{2L_B}\left(1 - F_y\right) + \frac{L_A + L_C}{2L_B}\left(1 - F_{(1+9)(7+8)}\right) = \frac{R}{R_p} F_{7,10} \end{aligned}} \qquad \textbf{(A-75)}$$

The view factor F_{72} now needs to be determined, thus

$$F_{72} = F_{75} - F_{7,10} - F_{76} \qquad \textbf{(A-76)}$$

but since $F_{(7+8)(7+8)}$ is already known from Leuenberger's paper, we will define a view factor F_v such that:

$$\begin{aligned} F_v = F_{(7+8)(7+8)} = {} & 1 - \frac{R_p}{R} \\ & + \frac{1}{\pi}\left[\frac{2R_p}{R}\tan^{-1}\frac{2\sqrt{R^2 - R_p^2}}{L_A + L_C} - \frac{L_A + L_C}{2R}\Lambda\right] \end{aligned} \qquad \textbf{(A-77)}$$

where Λ is given by

$$\Lambda = \frac{\sqrt{4R^2 + (L_A + L_C)^2}}{L_A + L_C} \sin^{-1} \frac{4(R^2 - R_p^2) + \frac{(L_A + L_C)^2}{R^2}\left(R^2 - 2R_p^2\right)}{(L_A + L_C)^2 + 4(R^2 - R_p^2)} \tag{A-78}$$

$$- \sin^{-1} \frac{R^2 - 2R_p^2}{R^2} + \frac{\pi}{2}\left[\frac{\sqrt{4R^2 + (L_A + L_C)^2}}{L_A + L_C} - 1\right]$$

hence

$$F_{(7+8)5} = F_{(7+8)3} = \frac{1}{2}\left[1 - \frac{R_p}{R} F_x - F_v\right] \tag{A-79}$$

since

$$F_{57} + F_{58} = F_{5(7+8)} \tag{A-80}$$

$$F_{75} = \frac{A_5}{A_7}\left[\frac{A_7 + A_8}{A_5} F_{(7+8)5} - \frac{A_8}{A_5} F_{85}\right] \tag{A-81}$$

$$F_{75} = \frac{L_A + L_C}{L_A} F_{(7+8)5} - \frac{L_C}{L_A} F_{85} \tag{A-82}$$

then from the above equations

$$F_{75} = \frac{L_A + L_C}{2L_A}\left[1 - \frac{R_p}{R} F_x - F_v\right] - \frac{L_C}{L_A} F_{85} \tag{A-83}$$

Since the view factors $F_{(8+2)6}$ and $F_{(7+8+2)6}$ are already known, we will define F_w and F_t respectively:

$$F_w = F_{6(8+2)} = \frac{A_8 + A_2}{A_6} F_{(8+2)6} \qquad \textbf{(A-84)}$$

$$F_t = F_{6(7+8+2)} = \frac{A_7 + A_8 + A_2}{A_6} F_{(7+8+2)6} \qquad \textbf{(A-85)}$$

hence

$$F_{67} = F_{6(7+8+2)} - F_{6(8+2)} = F_t - F_w \qquad \textbf{(A-86)}$$

$$F_{76} = \frac{A_6}{A_7}\left(F_t - F_w\right) = \frac{R^2 - R_p^2}{2RL_A}\left(F_t - F_w\right) \qquad \textbf{(A-87)}$$

Then as

$$F_{72} = F_{75} - F_{7,10} - F_{7,6} \qquad \textbf{(A-88)}$$

substituting for F_{75} and F_{76} from Equations (A-83) and (A-87) respectively gives the final result for the view factor F_{72}:

$$\boxed{\begin{aligned} F_{72} = {} & \frac{L_A + L_C}{2L_A}\left[1 - \frac{R_p}{R} F_x - F_v\right] \\ & - \frac{L_C}{L_A} F_{85} - F_{7,10} + \frac{R_p^2 - R^2}{2RL_A}\left(F_t - F_w\right) \end{aligned} \qquad \textbf{(A-89)}}$$

Note that the case of the probe wall being longer than the channel wall or *vice versa* has been previously dealt with in Leuenberger's paper - Case 10; two concentric cylinders of unequal length, one enclosed by the other. This involves determining view factors such as $F_{1(8+2)}$, $F_{9(7+8)}$, *etc* which can be obtained using a similar procedure as explained above. The results from Leuenberger's paper were used if this situation arose.

The case of radiation transfer to the ends of the channel now has to be dealt with, referring to Figure A-3 the entrance and exit elements are labelled 3 and 6 respectively. The view factors F_{86}, F_{83}, F_{96}, and F_{93} are required. It follows from the definition of F_w that:

$$F_{68} = F_w - F_{62} \tag{A-90}$$

$$\boxed{F_{86} = \frac{R^2 - R_p^2}{2RL_C} F_w - \frac{L_B}{L_C} F_{26}} \tag{A-91}$$

and similarly

$$\boxed{F_{83} = \frac{R^2 - R_p^2}{2RL_C} F_{3(7+8)} - \frac{L_A}{L_C} F_{73}} \tag{A-92}$$

It follows that

$$F_{96} = F_{95} - F_{92} \tag{A-93}$$

F_{92} can be obtained from Equation (A-72) :

$$F_{92} = \frac{1}{2}\left(1 - F_{98}\right) - \frac{L_C + L_B}{2\,L_B}\left(1 - F_{(9+10)(8+2)}\right) + \frac{L_B}{2\,L_C}\left(1 - F_{10,2}\right) \tag{A-94}$$

thus the view factor F_{96} is given by:

$$\boxed{\begin{aligned} F_{96} &= F_{95} + \frac{1}{2}\left(F_{98} - 1\right) \\ &\quad + \frac{L_C + L_B}{2\,L_B}\left(1 - F_{(9+10)(8+2)}\right) + \frac{L_B}{2\,L_C}\left(F_{10,2} - 1\right) \end{aligned}} \tag{A-95}$$

and similarly F_{93} is given by:

$$F_{93} = F_{94} + \frac{1}{2}\left(F_{98} - 1\right) + \frac{L_A + L_C}{2L_A}\left(1 - F_x\right) + \frac{L_A}{2L_C}\left(F_{17} - 1\right) \qquad \textbf{(A-96)}$$

B

APPENDIX

B.1 Example Parameter File for the Mathematical Model of the Single Channel Monolith Reactor

```
==================================
Paramaters for monolith simulation
==================================

General parameters
------------------
Problem type ..........................................  009
Reading of initial solution ...........................    1

Parameters related to numerical method
--------------------------------------
Number of iterations in time ..........................  500
Number of iterations for coupling .....................   20
Number of iterations in temperature ...................    1
Number of iterations in concentration .................    1
Number of steps between matrix factorisations .........    1
Kinetic model type (0=power law, 1=lhhw type ..........    0
Number of inside emissivity loading steps .............    1

Size of the time step .................................  1.000E+01
Tolerance for stopping criterion ......................  1.000E-03
Sensitivity for stopping criterion ....................  1.000E-06

Physical parameters for problem
-------------------------------
Average inlet velocity of gas .........................  1.548E+00
Initial temperature of gas ............................  7.500E+02
Initial concentration .................................  0.000E+00
Thermal conductivity of gas, k=a+bt    a coeff .........  8.870E-03
                                       b coeff .........  6.024E-05
Pre-exponential factor for the homo reaction ..........  7.000E+03
Activation energy for the homo reaction ...............  5.200E+04
Pre-exponential factor for the catalytic reaction .....  2.000E+00
Activation energy for the catalytic reaction ..........  0.000E+00
Pre-exponential factor for the adsorption term ........  0.000E+00
Activation energy for the adsorption term .............  0.000E+00
Coefficient of diffusion for the mass Do...............  2.532E-05
Total system pressure .................................  1.013E+05
Inlet temperature of the gas ..........................  7.500E+02
Entrance temperature for radiation ....................  7.500E+02
Outlet temperature for radiation ......................  4.500E+02
Temperature of surroundings (radiation) ...............  8.380E+02
Temperature of surroundings (convection) ..............  7.500E+02
```

```
Properties of the wall
----------------------
Density of the wall material ..........................  5.049E+03
Thermal conductivity of wall, kw = a + bT   a term .....  1.192E+01
                                            b term .....  0.000E-00

Heat capacity of the wall, Cp = a + bT  a term ........  8.500E+02
                                        b term ........  0.000E+00

Effective wall thickness of reactor ...................  5.250E-03
Emissivity of the inside wall .........................  8.000E-01
Initial value for inside emissivity loading ...........  8.000E-01
Emissivity of the outside wall (0 for no radiation) ...  7.000E-01
External convection transfer coefficient...............  0.000E+00


Enthalpy of reaction parameters
-------------------------------
Coefficient a ......................................... -5.573E+06
Coefficient b .........................................  6.199E+01
Coefficient c ......................................... -2.133E-02
Coefficient d ......................................... -7.941E-05
Coefficient e .........................................  4.471E-08

Inlet gas composition
---------------------
Mole fraction of propane ..............................  5.374E-03
Mole fraction of oxygen ...............................  1.912E-01
Mole fraction of nitrogen .............................  8.048E-01
Mole fraction of carbon dioxide .......................  0.276E-03
Mole fraction of water vapour .........................  0.000E+00
Weight factor for concentration loop ..................  0.250E+00
Weight factor for temperature loop ....................  0.250E+00
```